Advanced Virgo: INJ subsystem Preliminary Design study.

Authors:
**B. Canuel, R. Day, E. Genin, P. La Penna, M. Mantovani, J. Marque
and F. Paoletti**

**Date :**
05/05/2009

VIR-023A-09

Table of contents:

Introduction

The purpose of this document is to describe the studies that have been done so far on AdV INJ subsystem that should motivate the choices made for AdV INJ baseline design.
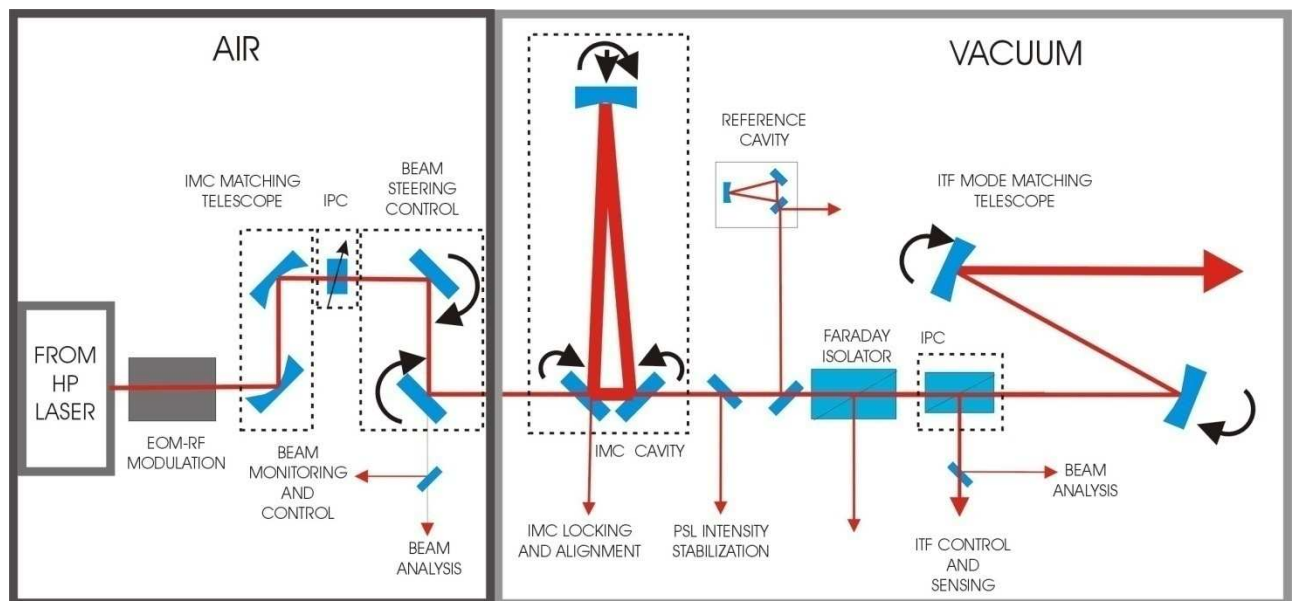
In section 1, the principle of Electro optical modulation is presented as well as the possible crystals that can be used for AdV (withstand high laser power, low thermal effects). Some elements on modulation scheme and possible noise sources are also given.

A power adjustment system, will be used in order to tune ITF input power (important for ITF lock acquisition). The principle of operation of this system is given in section 2.

Some preliminary considerations on input beam jitter are given in section 3.

In section 4, a study of IMC cavity gives some considerations to be taken into account for the AdV IMC cavity choice in term of shape, length and Finesse.

Section 5 explores the possibility to remove the reference cavity from the suspended injection bench.

Particularly critical optical paths such as ITF and IMC reflection sensing setup are introduced in section 6 in terms of back-scattering noise and safety issue due to the high laser power used in AdV.

Section 7 describes the kind of in-vacuum Faraday isolator that should be used in AdV and the progresses made on this topic from the design and the experimental point of views.

Finally, since INJ should also provide a way to monitor laser beam properties in different points of INJ subsystem a general study of the effects to monitor and some possible tools to characterize it are presented as well as some possible ways to compensate for thermal effects on INJ.

Design study

1. Electro-optic Modulation system (EOM)

DC detection is baseline for Advanced Virgo. Nevertheless, RF modulation will be used for the control of the interferometer, both for longitudinal and angular controls. The main difference between the EOM to be used in AdV and Virgo resides in that the power that the EOM system will have to withstand will be almost 10 times higher (180-200 W instead of 20 W).

Thermal effects will become more significant [1] and the choice of the appropriate material becomes crucial.

Requirements in AdV for EO modulation will also be different. Many of these parameters will affect the driving electronics and signal generator choice. Indicative numbers for the single sideband noise requirements (modulation phase noise) can be found in [2], and for modulation index noise (amplitude noise) in [3]. More than one modulation frequency will likely be used in AdV (probably three for ITF control and one for IMC cavity), either for control and for monitoring. The increased sensitivity and complexity of the interferometer will make it important to address the problems of sidebands on sidebands generation. The solution of this problem could imply novel EOM topology (see for example [4]) or new modulation generation techniques (see for example [5]), which have still to be fully tested and assessed.

In the following paragraphs, the principle of EO modulation is described, the problem of generation of sidebands on sidebands is addressed and possible candidates as EO crystals are presented and their characteristics are given. Finally, the possible modulation schemes for AdV are presented.

1.1. RF Modulation Requirements

The requirements on optical modulation, including modulation frequencies, modulation depths, and relative stability of the modulation frequency and amplitude, for AdV should be defined by the ISC subsystem and will depend on the IMC cavity length. Since the modulation frequencies used to control the ITF have to pass through the IMC, they have to satisfy the following equation $f = nc/2L_{IMC}$, where n is an integer, c, the light velocity, and L_{IMC}, the IMC cavity length. We will assume in this document that the maximum modulation depth required is about 0.2.

1.2. Principle of operation: phase modulator.

1.2.1. Phase modulator.
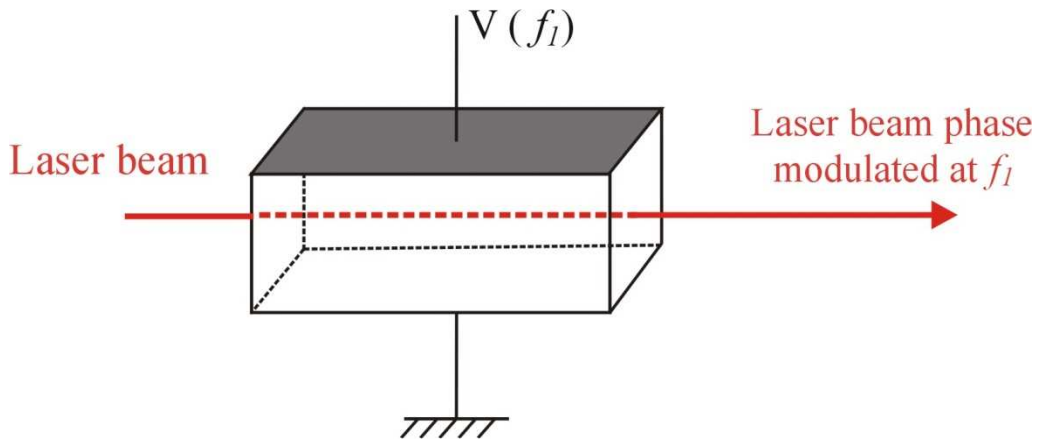
Figure 1: Phase modulation of the light using the Pockels effect.

The laser beam electric field at the input of the modulator can be written as $E=E_0 \exp(i\omega t)$.

When we apply a voltage modulated at frequency f_1 , the electric field of the light at the output of the modulator is expressed as follows:

$$E_{out} = E_0 \exp(i2\pi ft)\exp(i\beta \sin(2\pi f_1 t)) \tag{1}$$

Considering that $\omega = 2\pi f$ and $\omega_1 = 2\pi f_1$, we can rewrite Eq. 1 as:

$$E_{out} = E_0 \exp(i\omega t)\exp(i\beta \sin(\omega_1 t)) \tag{2}$$

The complete development can be written as follow:

$$
\begin{aligned}
E_{out} &= E_0 \exp(i\omega t)\exp(i\beta \sin(\omega_1 t)) \\
&= E_0 \exp(i\omega t)\left(J_0(\beta) + \sum_{k=1}^{\infty} J_k(\beta)\exp(ik\omega_1 t) + \sum_{k=1}^{\infty}(-1)^k J_k(\beta)\exp(-ik\omega_1 t) \right)
\end{aligned} \tag{3}
$$

Considering that β is small we can write Eq. 2 as a Taylor expansion considering only the first term of the expansion. Eq. 2 becomes then:

$$E_{out} = E_0 \exp(i\omega t)(1 + i\beta \sin(\omega_1 t)) \qquad (4)$$

That can also be written as:

$$E_{out} = E_0 \exp(i\omega t)(1 + \frac{\beta}{2}(\exp(i\omega_1 t) - \exp(-i\omega_1 t))) \qquad (5)$$

We can also do the same job for 2 modulation frequencies. The beam is phase modulated twice at f_1 and f_2. In this case, Eq. 4 becomes:

$$E_{out} = E_0 \exp(i\omega t)(1 + \frac{\beta_1}{2}(\exp(i\omega_1 t) - \exp(-i\omega_1 t)))(1 + \frac{\beta_2}{2}(\exp(i\omega_2 t) - \exp(-i\omega_2 t))) \qquad (6)$$

$$E_{out} = E_0(\exp(i\omega t) + \frac{\beta_1}{2}\left(\exp(i(\omega+\omega_1)t) - \exp(i(\omega-\omega_1)t)\right) + \frac{\beta_2}{2}\left(\exp(i(\omega+\omega_2)t) - \exp(i(\omega-\omega_2)t)\right)$$

$$+ \frac{\beta_1\beta_2}{4}\left(\exp(i(\omega+\omega_1+\omega_2)t) + \exp(i(\omega-\omega_1-\omega_2)t) - \exp(i(\omega-v+\omega_2)t) - \exp(i(\omega+\omega_1-\omega_2)t)\right)$$

$$(7)$$

This is a very simplistic evaluation of the sideband amplitude and the sidebands on sidebands amplitude, nevertheless, we can see very well that sidebands on sidebands are generated so when we are modulating a beam (carrier frequency = f), we are creating sidebands at $f + f_1$, $f - f_1$, $f + f_2$, $f - f_2$, $f + f_1 + f_2$, $f + f_1 - f_2$, $f - f_1 - f_2$, $f - f_1 + f_2$.

1.2.2. Amplitude modulator.

Amplitude modulators basically consist of an electro-optic modulator followed by a polarizer. If the input polarization is oriented at 45° to the crystal axes, the applied voltage will produce a variable phase delay between the ordinary and extraordinary field components, simulating a voltage-tunable waveplate. Thus, the modulation of the intensity is a square sine function.
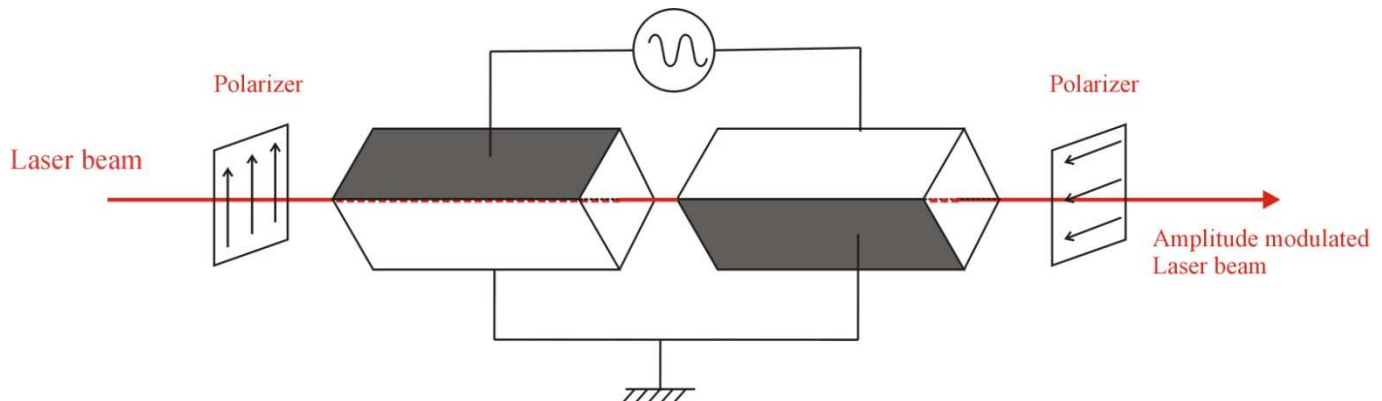
Figure 2: Amplitude modulation of the light using the Pockels effect.

Birefringence variations due to temperature changes is an issue for this kind of modulator especially in the case of AdV since the laser power passing through the crystal should be of the order of 180-200 Watts. In order to suppress this spurious effect, we can use two matched crystals

arranged in series with their applied electric fields oriented at 90° relative to each other. In this way, we suppress thermally-induced birefringence while doubling the electro-optically induced polarization rotations by reversing the crystal axes such that both polarization components see the same optical paths in the ordinary and extraordinary orientations (see Figure 2). If needed, this item will have to be further studied (TBD by ISC).

1.3. Electro optic material selection

1.3.1. Optical and Electro-optical Properties

Three kinds of crystals are considered in this preliminary study. The first one is KTP (currently used in Virgo as phase modulator), the second is RTP, that seems to be promising in terms of absorption and damage threshold compared to KTP, and the third one is lithium niobate doped MgO that could fulfil AdV requirements [6].

Properties	Units/conditions	RTP	KTP	MgO-LiNbO$_3$
Damage Threshold	MW/cm^2, (10ns, 1064 nm)	>600 (AR coated)	>600 (AR coated)	>280
n_x	1064nm	1.7652	1.7403	2.2238
n_y	1064nm	1.7751	1.7478	2.2238
n_z	1064nm	1.8536	1.8296	2.1456
Absorption coefficient α	cm^{-1} (1064 nm)	< 0.0005	< 0.0005	<0 .001
r_{33}	pm/V	39.6	36.3	32
r_{23}	pm/V	17.1	15.7	10
r_{13}	pm/V	12.5	9,5	?
r_{42}	pm/V	?	?	?
r_{51}	pm/V	?	7,3	?
r_{22}	pm/V	?	9,3	?
$n_z^3 \, r_{33}$	pm/V	252.2	222.3	316.08
Dielectric const., ε_{eff}	500 kHz, 22 ^{o}C	13	13	
Conductivity, σ_z	Ω^{-1}cm^{-1}	~10^{-11}-10^{-12}	10^{-6}	
Thermal conductivity	W.m^{-1}.K^{-1}	k=3	k$_x$=2.0 k$_y$=3.0 k$_z$=3.3	5.6
Thermo-optic coefficient	/K	dn$_x$/dT=? dn$_y$/dT=0.279x10^{-5} dn$_z$/dT=0.924x10^{-5}	dn$_x$/dT=1.1x10^{-5} dn$_y$/dT=1.3x10^{-5} dn$_z$/dT=1.6x10^{-5}	dn$_x$/dT=5.7x10^{-6} dn$_z$/dT=3.9073x10^{-5}
Thermal Expansion	/°C	α_x=1.01x10^{-5} α_y=1.37x10^{-5} α_z=4.17x10^{-6}	α_x=1.1x10^{-5} α_y=0,9x10^{-5} α_z=0,6x10^{-6}	
Density	g/cm3	3,6	3.03	
Specific Heat	Cal/g.°C	?	0,1737	

Table 1: Parameters of KTP (from Cristal Laser), RTP crystals (from Raicol) and MgO-LiNbO$_3$ (literature survey).

The largest EO-coefficient is r_{33} (see Table 1). The optimum configuration is a propagation of the beam along y-direction and applies the electrical field in the z-direction.

1.3.2. Modulation depth estimation

In these conditions, the modulation depth can be written as:

$$\Delta\Phi = m = \frac{\pi L}{\lambda} r_{33} n_z^3 \frac{V_z}{d} \tag{8}$$

where L is the length of the crystal, V_z the voltage across the crystal, and d the thickness in the z-direction. The modulation depth of $m = 0.2$ leads to:

$$V_z \frac{L}{d} = \frac{m\lambda}{\pi r_{33} n_z^3} = 268.6V \text{ for RTP}, \quad V_z \frac{L}{d} = 304.7V \text{ for KTP and } V_z \frac{L}{d} = 214.3V \text{ for MgO-LiNbO}_3.$$

For typical dimensions, L = 20 mm and d = 4 mm, V_z = 53.7 V for RTP, 60.9V for KTP and 43 V for MgO-LiNbO$_3$.

A resonant circuit, with the RTP crystal as the capacitor, reduces the required input voltage by the Q of the resonator as currently done in Virgo for 6.26, 8.35 and 22.38 MHz modulation frequencies.

1.3.3. Halfwave voltage

The halfwave voltage is the voltage we have to apply on the electro optic crystal in order that the phase modulator behaves as a halfwave plate. This means, $m = \pi$ and as a consequence:

$$V_\pi = \frac{d\lambda}{L r_{33} n_z^3} = 843.7V \text{ for RTP} \quad ; V_\pi = 957.26V \text{ for KTP} \quad ; V_\pi = 673.2V \text{ for MgO-LiNbO}_3.$$

1.3.4. Thermal lensing measurements

It is important to select the right material in terms of thermal focusing; not only to limit wavefront aberrations but also because it is a proof of local heating of the material that can induce slow variation of the modulation index (this creates RFAM noise).

As part of the HPIO R&D program, we have carried out some measurements of thermal lensing with a Shack-Hartmann wavefront sensor on different samples of KTP, RTP and MgO-LiNbO3. These samples were tested with a laser beam of 100 W and a beam size of about 1mm. We selected the right polarization and crystal orientations in order to get an electrical field along r$_{33}$.

A telescope placed close to the Shack-Hartmann enables to tune a flat beam on it. Then by placing the sample close to the sensor, we measured directly the thermal lensing created by the material. Here are the results obtained with the different samples:

- We have tested two KTPs coming from different orders placed with Cristal Laser (France). The tested crystals are 5x5x12mm x-cut (corresponding to the actual Virgo EOMs). The first one gave **23m** of thermal lensing and the second **8m** (see Figure 3).

- We have also tested a RTP from Cristal Laser (France), 5x5x12mm y-cut. We measured **8 m** of thermal lensing. A RTP crystal from another source was also tested (a 4x4x20mm crystal from Raicol (Israel)). Being slightly smaller, this crystal was tested with an other setup. With a beam of 0.8 mm of waist and 40W of power, no lensing was measured.
- The last material tested was a MgO-LiNbO3 crystal, y cut 5x5x10 mm provided by Prof. Mio (University of Tokyo, Japan). At 100W we could measure along z axis **8m**.

From these preliminary results we can conclude that KTP crystals could be good candidates (one is measured at 23m). According to literature, it would be possible to obtain even better results with RTP crystals. Some tests should go on with RTP crystals from Raicol that were successfully tested at LIGO (no noticeable lensing obtained at 60W but with a less sensitive measurement). Nevertheless, even after identification of the best material/manufacturer, it seems clear that it will be necessary to set up a process of selection to find the better crystals.
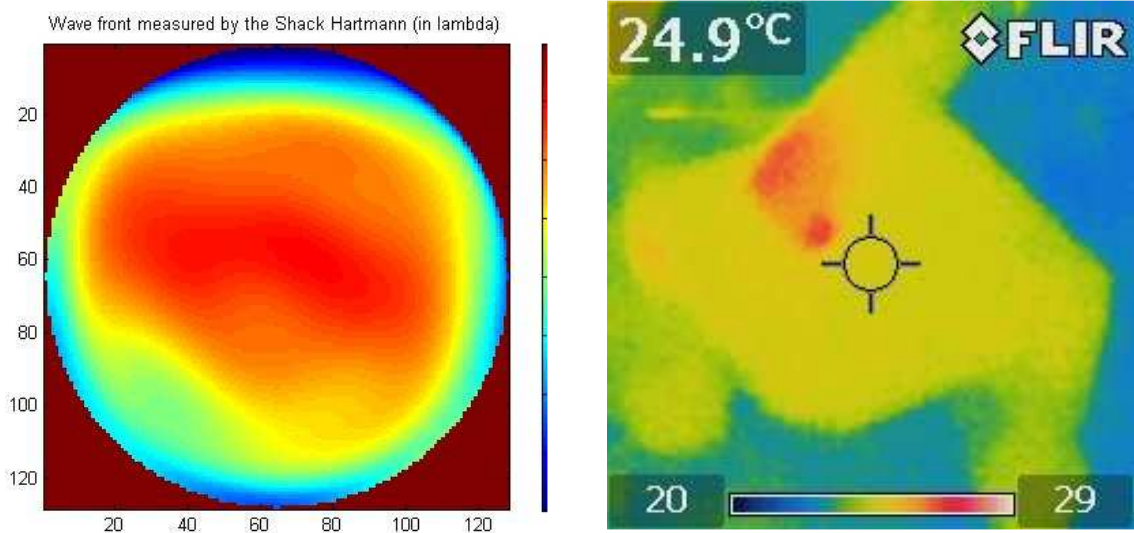
Figure 3: Results of measurement of one of the two KTP crystals tested. Left picture: wavefront measured by the Shack-Hartmann sensor. From it, we can extract a lensing of about 8 m. Right picture: heating of the material seen with a thermal camera.

1.3.5. Damage threshold

The intensity distribution in a Gaussian mode with total power P_o is:

$$I(r) = P_o \frac{2}{\pi} \frac{e^{-2\frac{r^2}{w^2}}}{w^2} \tag{10}$$

10

For a gaussian beam, we have 86% of the beam power in a $2w$ diameter; this gives a mean power density about $0.86P/\pi w^2 = 21.9kW/cm^2$ for a 0.5 mm waist beam for a 200 watts laser beam which is much lower than the damage threshold given by the manufacturer.

In any case we plan to test RTP and KTP crystals with 200 W (they have already been tested with 100 W and we couldn't see any damage). We have already some experience in Virgo concerning KTP; we have also destroyed a crystal instantly when the 20 W beam touched one of the electrodes. We will have to take particular care to not send the very high power beam onto the electrodes. This can be very easily avoided by installing some metallic diaphragms in front of crystal to protect the electrodes from the laser beam.

1.3.6. Selected material

Among the three electro optic crystals that have been considered in this study, KTP and RTP could be used as part of the Electro-optical Modulation system for AdV. These materials have lower thermal lensing effect and higher damage threshold and are permitting to work with 200 W continuous laser power. Laboratory tests have shown that it will be necessary to carefully select the crystal to be used for AdV since crystal properties can change significantly from one manufacturer to another.

1.3.7. Performances in term of Phase noise and RF amplitude modulation

1.3.7.1. Phase noise

Fluctuation in the modulation frequency due to oscillator phase noise can spoil the interferometer performance. In this section, we will give an upper limit of Virgo oscillator phase noise that has been measured.

Of the many methods available for measuring the Phase Noise of a given source, each one has its own pros and cons, we have used the so called "single-channel measurement method" for our tests in VIRGO, and with this method we have been able to characterize the VIRGO main signal generator's phase noise.
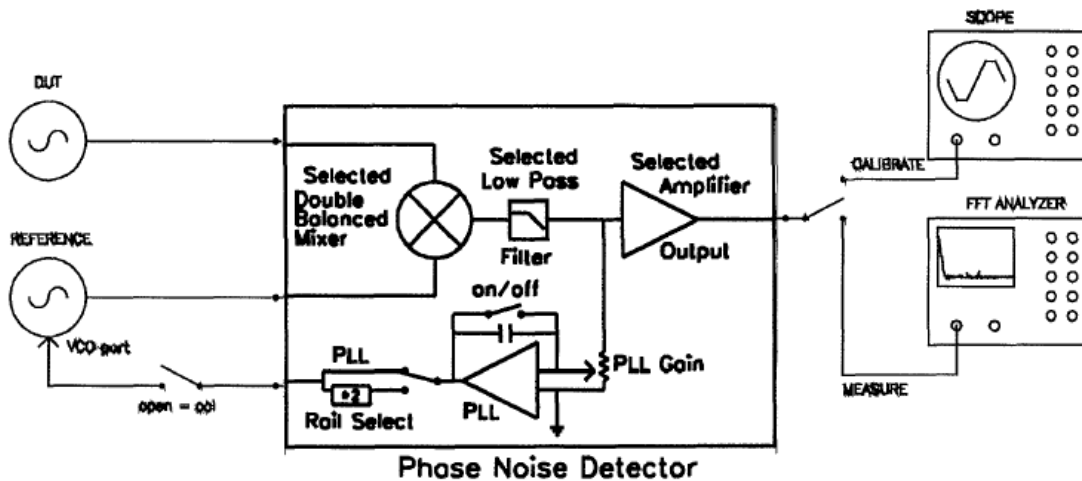
Figure 4: Single Channel Phase Noise Measurement Setup.

The single channel measurement system refers to the fact that only one channel comes out to the FFT or spectrum analyzer. Figure 4 illustrates such a system. This system topology typically refers to a two-source system where one signal is phase-locked to the other. This technique is generally used when two sources, at the same frequency, are involved. This approach works over a large frequency range and has a reasonably low phase noise measurement floor.

This is one of the simplest systems to set up and start using, but one disadvantage of this method is that one cannot separate the noise in the reference from that in the DUT (Device Under Test). Multiple measurements may be required to determine which source dominates the noise floor. If the reference is 20 dB below the noise of the DUT, then the reference can be ignored and the DUT is the main contributor. If the DUT and reference are at the same level (as we have in VIRGO), then we have to divide the noise between the two sources (subtract 3 dB).

Relying on the fact that the generators for which we want to measure the phase noise are quite stable over time (the internal reference is a high stability Oven-Controlled Crystal OscillatorOCXO), we have decided not to "phase lock" the Reference in quadrature: in our case the long term stability of the S.G.s is so high that we can have both in quadrature for minutes, allowing a sufficiently precise measurement.

A preliminary measurement produced an Upper Limit that is very close to the declared Signal Generator's Phase Noise as you can see on Figure 5.
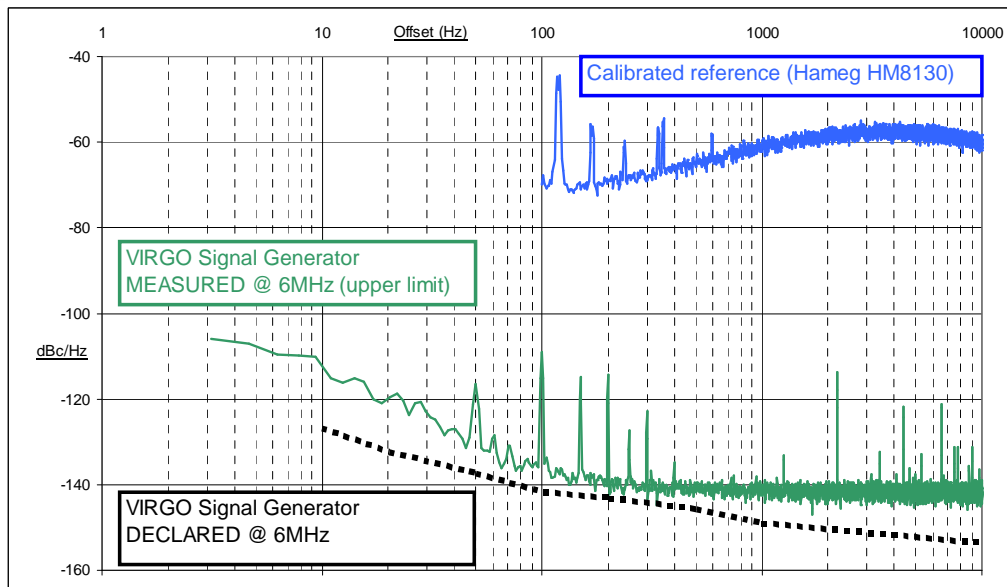
Figure 5: Upper Limit noise measurement (green curve), SDI declared noise at 6 MHz (black dashed curve),

Phase noise from Hameg HM 8130 (blue curve) used for measurement calibration check.

As visible in the plot, the limit of the used setup is:

Frequency offset (Hz)	Phase noise upper limit (dBc)
10	-113
100	-138
1000	-145
10000	-145

A link to the documentation for the SDI signal generator used in Virgo is given in [LNFS100].
Going further down with the resolution call for more sophisticated techniques, not available at the time of writing. We are evaluating the purchase of the needed instruments.
With this method we have been able to find an Upper Limit for the VIRGO main signal generator's phase noise, and using this Upper Limit it is now possible to evaluate the projection of this noise into the AdV sensitivity curve. At the same time we have demonstrated the feasibility of this measurement technique that can be used to test other RF sources.

1.3.7.2. RFAM (Radio frequency amplitude modulation)

According to measurements perform on Virgo interferometer (see logentry # 22358), this noise is far from limiting the sensitivity nevertheless this item will have to be further investigated once the AdV optical configuration has been chosen.

1.4. Possible modulation schemes

For AdV, we should provide an EOM system that is able to phase modulate the beam at 4 different modulation frequencies (see ISC documents for the values). It is likely that we keep the same modulation frequency for the IMC cavity lock as in Virgo (f = 22.38 MHz).

1.4.1. Serial configuration (Virgo-type)

This configuration is already used in Virgo without experiencing any problems (see Figure 6). Two KTP based EOMs are used to apply 3 modulation frequencies (6.26, 8.35 and 22.38 MHz). In AdV, three modulation frequencies should be used for ITF sensing and control (see note [8]) and one should be used to control the IMC cavity.

This means that we have to apply 4 modulation frequencies at the high power laser output and a multiple of sidebands on sidebands will be generated. In the past, we have already made some simulations on this problem and the conclusion was that we could get rid of this problem by phase locking the modulation frequencies sued to control the Interferometer. Nevertheless, some simulations by the ISC subsystem on the effect of sidebands on sidebands on the ITF error signals are needed to check if this configuration is suitable or not.
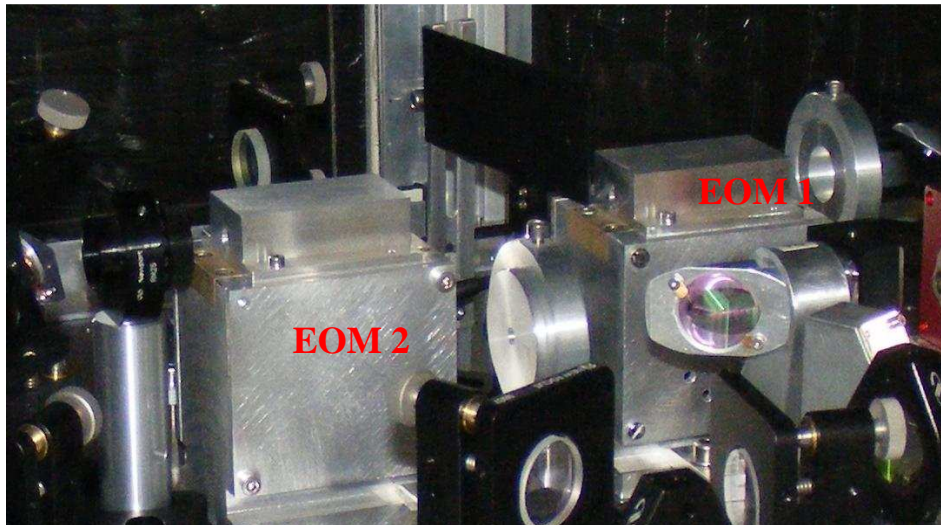
Figure 6: Virgo+ serial configuration to phase modulate the laser beam at 6, 8 and 22 MHz.

1.4.2. Parallel configuration

This parallel configuration that consists of using a Mach-Zehnder interferometer to avoid the sidebands on sidebands generation problem is the current baseline solution for Advanced LIGO [4].

1.4.2.1. Principle of operation

We need some input from ISC subsystem to see what could be the impact of sidebands on sidebands on the AdV ITF control. The principle of operation of this EOM system is quite simple. A principle scheme is given in Figure 7.
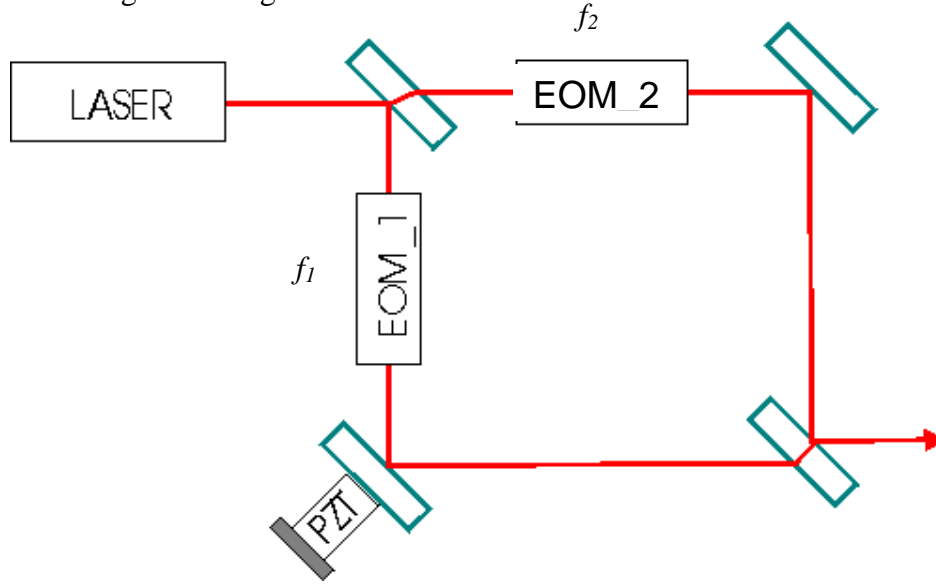
Figure 7: Parallel (Mach-Zehnder) electrooptic modulation system.

EOM_1 and EOM_2 are two phase modulators that modulate the beam phase at the frequencies f_1 and f_2. In this way, we are sure that we avoid creating sidebands on sidebands. The main drawback of this kind of modulation is that we need to control the optical path length of the two arms in order to avoid additional phase noise coming from the common motion of the two arms and amplitude noise coming from the differential motion of the arms. Some estimation of the contribution of each noise source will be given in the next paragraph.

1.4.2.2. Noise coupling

The Mach-Zehnder output field can be written as:

$$E_{out} = \frac{E_0}{2}\exp(i\omega t)\left(\exp(ikL_1 + im_1\sin(\Omega_1 t)) + \exp(-ikL_2 + im_2\sin(\Omega_2 t))\right) + \text{c.c.}$$

(11)

$$E_{out} = \frac{E_0}{2}\exp(i\omega t)\exp(ik(L_1 + L_2)/2)\left(\exp(ik(L_1 - L_2)/2 + im_1\sin(\Omega_1 t)) + \exp(-ik(L_1 - L_2)/2 + im_2\sin(\Omega_2 t))\right)$$

$$+ c.c$$

(12)

From Eq. 12, we see that the Mach-Zehnder (MZ) output field depends on two quantities $L = (L_1 + L_2)/2$ and $\Delta L = (L_1 - L_2)/2$. It becomes then possible to evaluate the contribution of the MZ arm common length motion (*L*) and MZ arm differential length motion (*ΔL*) on phase and amplitude noise at the output of the EOM system.

1.4.3. Complex modulation configuration

Finally, there is a second way to phase modulate the beam avoiding the problem of sidebands on sidebands. The modulation scheme is explained in a LIGO note [3] and has not been considered for the moment since it would require a major effort of R&D in that direction that seems not possible considering the current manpower working on EOM design and test for AdV.

1.4.4. Conclusion

For the moment, it is not possible to select the modulation scheme that should be chosen for AdV. Some input from the ISC subsystem is needed (requirements in terms of phase and amplitude noise, how the generation of sidebands on sidebands is affecting the ITF control system?,…).

2. Input Power Control (IPC)

INJ system should provide a way to change the interferometer (ITF) input power keeping the INJ system elements (IMC cavity, Reference cavity (RFC)) under control with the same performances in term of noise level at each power.

The configuration that seems more reasonable if we want to save commissioning time, consists in having a system where one can adjust the laser power **before the IMC cavity** and after all the optical elements that are experiencing thermal effects after the Input Mode-Cleaner and suspended Faraday, in other word **at the ITF input port**.

2.1. IPC principle

In order to adjust the power, the most convenient system consists of a half wave plate placed between two polarizers. This system, already used in Virgo to adjust the power at the output of the IMC matching telescope, is presented in Figure 8.

As this system should handle both light and back reflected by the interferometer, the two situations are treated here. Light going to the interferometer (S-Pol) goes through P1, its polarisation is turned by θ by the wave-plate and after crossing P2 goes towards the interferometer with S-polarisation with an attenuated power of P_0 (1-cos$^2(\theta)$). Reflected light by P2 should go to a high power beam dump. No specific requirements about diffused light are necessary for this beam dump, as its back reflections cannot re-enter into the interferometer.
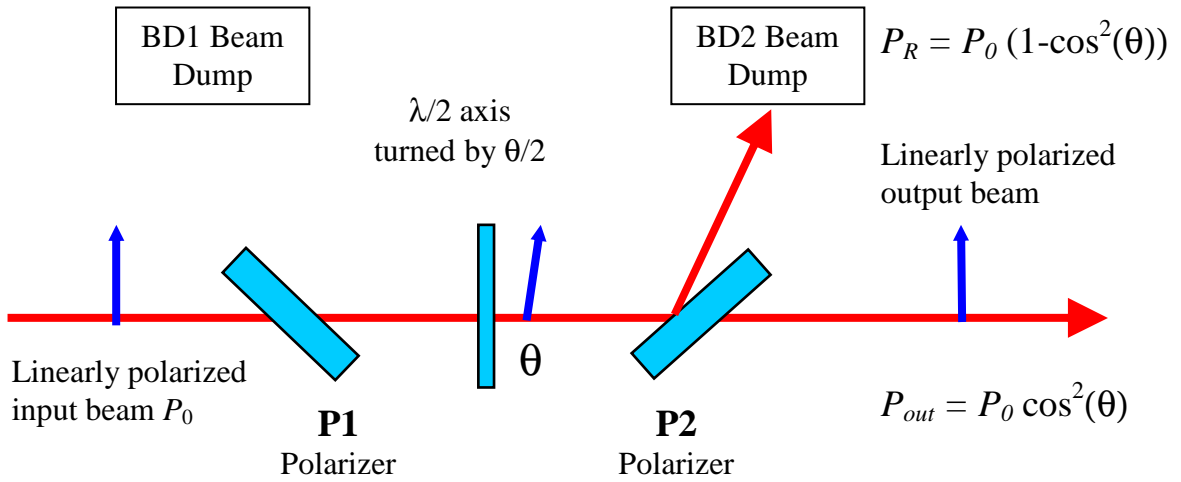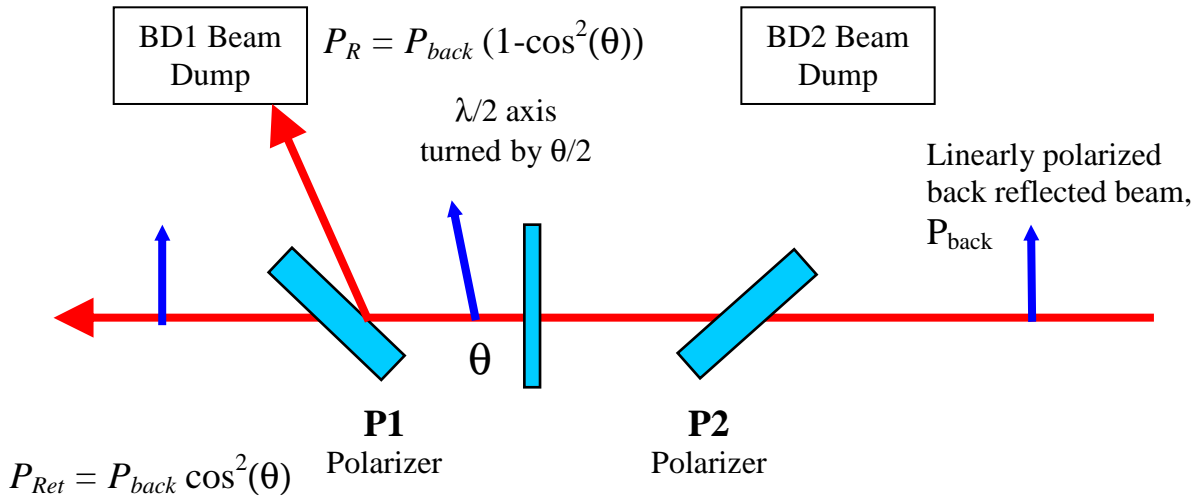
Figure 8: Input Power Control system: principle of operation.
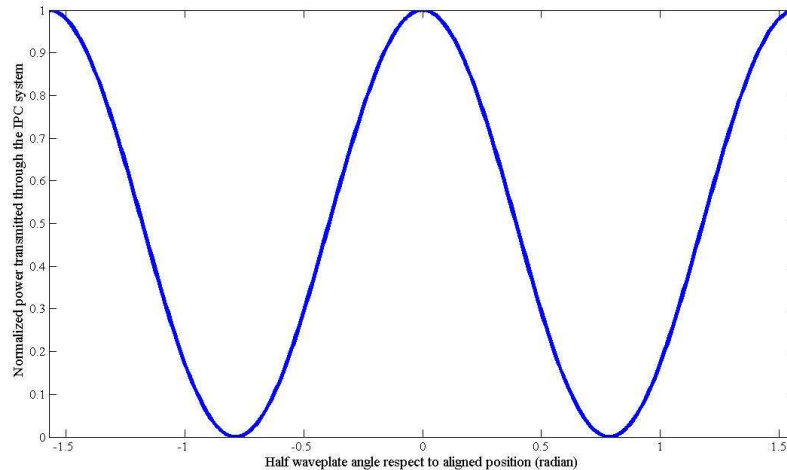
Figure 9: Normalized power transmitted by Input Power Control system

function of half wave plate axis respect to polarizer axis.

On Figure 9, one can see that turning the half wave plate by $\pi/4$ radians, the power transmitted can drop down to 0. This value is only theoretical and depends obviously on the extinction capability of the polarizer. Tests done in laboratory showed that even with high power we can expect up to 40 dB extinction for thin film Brewster polarizers. Since we will need to go down to several watts for locking purpose, we are not expecting any problem from the IPC system with these kind of polarizers.

Back reflected light coming from the interferometer should go through P2, its polarisation is turned by θ by the wave plate and therefore $P_{back}\cos^2(\theta)$ is going back towards the laser system after crossing P1. The P-Polarized light reflected by P1 should go to another high power beam dump. Diffused light on this beam dump can recouple to the interferometer and therefore, a low diffusing system should be used on this beam.

2.2. IPC technical realisation.

2.2.1. Thermal effects in polarizers and waveplates.

The first main issue of the IPC system is that it must not exhibit thermal effects that could impact beam quality or polarisation at its output. This is critical as one of these IPCs would be placed directly at the ITF input port.

Many tests were performed as part of the "high power input optics R&D" in order to determine suitable half wave plates and polarizers. Concerning polarization quality, it turns out that the best polarizers tested were Thin Film Plate Polarizers from EOT technology that could achieve more than 40 dB of extinction. This type of polarizer is already used for the Virgo suspended Faraday isolator. Unfortunately these polarizers exhibit substantial thermal lensing due to the use of BK7 substrates. Some custom Fused silica items were ordered and will be tested soon.

Nevertheless it is still possible to use optically contacted cubes in Fused Silica (for example CVI PBSO-1064-100) that were tested up to 100W with a beam waist of 1mm and showed no absorption. The drawback is the polarization quality that is slightly worse (31dB) with comparison

to the TFPP, but for the IPC system this should not be a problem since we could add another polarizer in series if a better polarization quality is needed.

Concerning waveplates the performed tests showed that a standard optically contacted waveplate from CVI is compliant with 40 dB of extinction. Besides no absorption could be measured on these components.

2.2.2. High power, low diffusing beam dump.

The other main concern of the IPC is the way light is dumped on P1. As stated before a low diffusing beam dump should be used in this case. Indeed, noise hunting on Virgo showed that diffused light on optics could spoil the ITF sensitivity. This is due to the fact that seismic noise of the optical bench creates some direct and up-converted noise measurable on the dark fringe through the phase-modulation of diffused light re-introduced into the interferometer [9].

Tests were made in the EGO optics lab [10] to characterize the diffusing properties of common beam dumps used in Virgo. It turned out that the best performances could be achieved with absorbing glass. The value of total diffused light from this material (integrated over the whole hemisphere) is in the 10 ppm range, very close to the values obtained with super polished optics. Much care should be given to the selection of the beam dump, as some tested items (razor blades or commercial high power bean dumps) were worse by 3 to 4 order of magnitude in terms of amount of diffused light.

Nevertheless, the problem of absorbing glass is that it is only suitable for low-medium power beams as it was shown to break at only 2 W for a 1mm beam waist. This is due to the low conduction coefficient of glass that makes it locally melt.

To realize a high power, low diffusing beam dump, it can be foreseen to use super polished metals or water [4]. In both cases, it is difficult for practical reasons to design a compact, easy to use, and possibly UHV compatible beam dump for 200W laser power. Therefore we propose to use layers of Silicon originally made for semiconductor production. Silicon is a very interesting material as it has a good conductivity (about 150 $W.m^{-1}.K^{-1}$ which is close to aluminum: 237), and it can be polished with an optical quality. Its absorption at 1064nm is also quite high: 45% for 1mm length, and increases with temperature. This material was tested in the EGO optics lab, and it was shown that it breaks at about 20-30W for 1 mm beam size. Values of total diffused light are at the same level as absorbing glass.

We were able to increase this breaking limit by cooling down the layer of Silicon with a Copper radiator (see prototype on Figure 10). With this setup, the Si beam dump prototype worked properly up to 80-100W, at which point it broke. Even if this level is already satisfactory, it could be further enhanced by improving the cooling system.
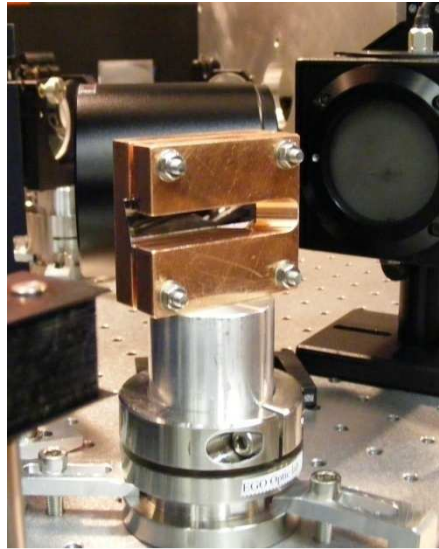
Figure 10: Silicon layer placed between two copper plates that evacuate heat.

In conclusion Silicon seems to be a very promising material to realize this type of beam dump.

2.2.3. IPC system before the IMC cavity
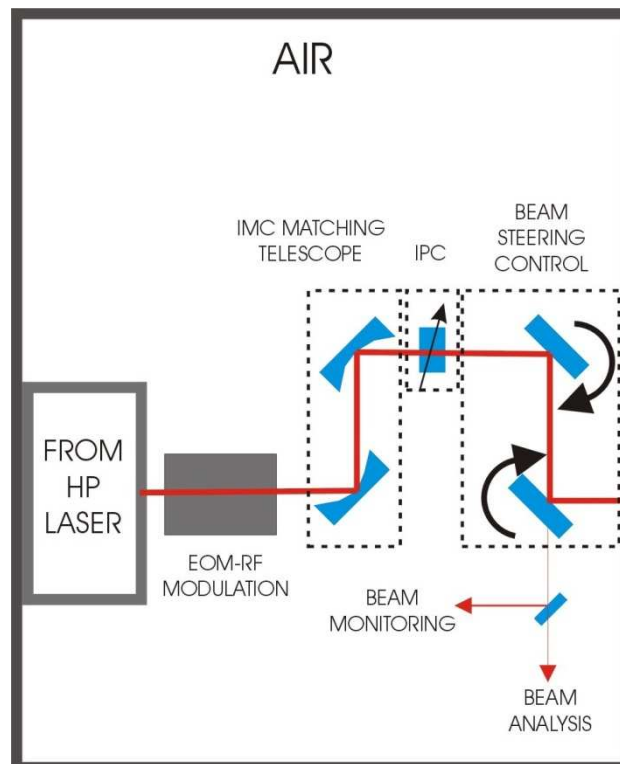
Figure 11: Possible position of the Input Power Control system before the IMC cavity.

First, we propose to install such a system just before the IMC cavity in order to be able to change its stored power, while keeping the rest of the injection system at the same power level.

Therefore we chose to place this IPC just after the IMC mode matching telescope. The Injection system control loops will be then kept in the same condition while changing the IMC power. The beam mode will also not experience any change as the IPC is installed after all the elements that are experiencing thermal effects in the injection system (Faraday isolators, EOM system) as it is shown on Figure 11.
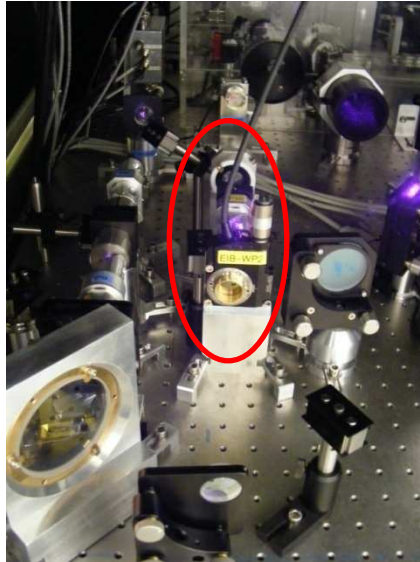
Figure 12: Virgo+ like Input Power Control system before the IMC cavity.

On Figure 12, one can see the Virgo+ IPC system that is installed before the IMC cavity.

2.3. IPC system after the IMC cavity
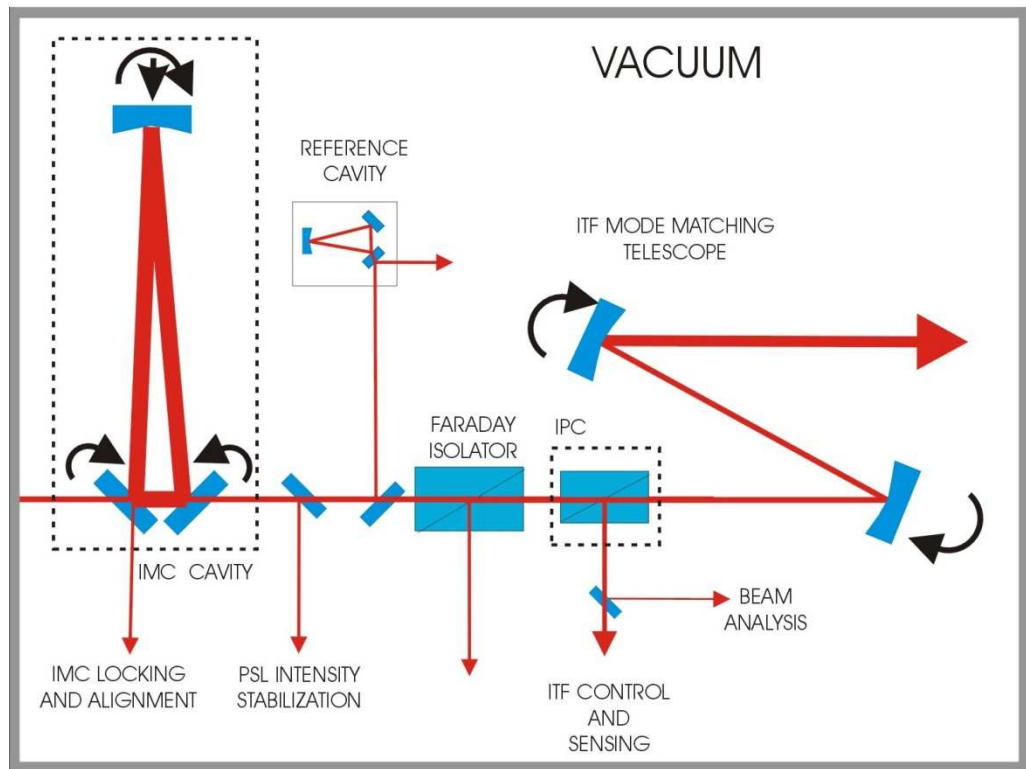
Figure 13: Possible position of the Input Power Control system after the IMC cavity.

We also propose to install a second IPC system just before the ITF, placed after all the elements that are potentially experiencing thermal effects (IMC cavity, Faraday isolator) (see Figure 13). In this way, we can avoid the change of thermal effects on the beam sent to ITF, while going from low to high power. This will minimize the change of all locking and alignment loops with ITF input power.

The use of this IPC modifies the way the reflection of the ITF is picked up for alignment and control of the ITF with respect to Virgo. For the actual Virgo, the reflected power is picked-off after passing again through the Faraday Isolator on the suspended bench which provides a beam quite distorted.

With the use of this IPC, the beam coming back to the faraday isolator will be much attenuated when the wave plate is turned in order to work with a low power inside the ITF. On Figure 14, we plot the power back reflected by the ITF and picked off by the Faraday as a function of power sent to ITF. When the ITF is working under 20W, less than 500mW would be available on this beam.

Then we propose to use for control and alignment, the beam coming from the ITF and reflected on the P1 polarizer of the IPC. This method will provide a cleaner beam. In this case for power sent to the ITF between 2 and 178W (i.e. between 1% and 99% of the full power), more than 500 mW would be available.

The only point that has to be clarified is the way we dump the laser power rejected by the attenuation system on BD2 (see Figure 8).
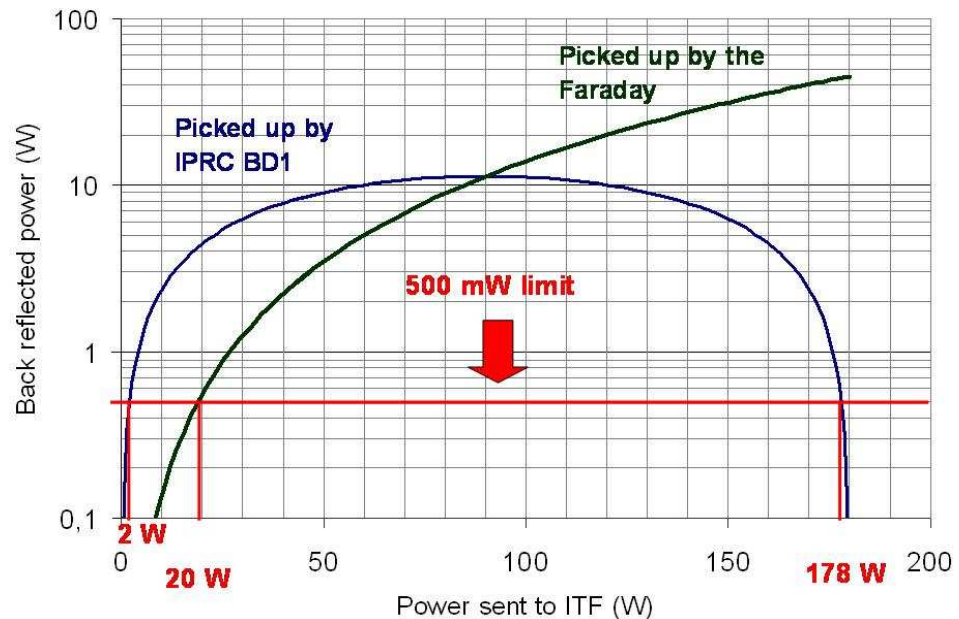
Figure 14: Back-reflected power picked up from IPC BD1

and by Faraday as a function of power sent to ITF.

For convenience, we propose to place this item directly on the Suspended Injection Bench (SIB). As said before, it is highly improbable that scattered light from this beam dump can re-couple to the ITF. Nevertheless, as commercial beam dumps produce a lot of diffused light that can affect photodiode signals or could recombine to the ITF through reflections on the vacuum chamber, a special, low diffusing beam dump should be used also here.

It remains to clarify if such power (could be higher than 100 W) can be dumped under vacuum without generating substantial thermal effects on the bench. In fact, the temperature elevation of BD2 will be quite high when dumping up to 200W. Therefore some investigation should be done to know if we can cool it down easily under vacuum.

Besides, since we will have a lot of things to install on the suspended bench (Faraday isolator, IMC input and output mirrors, PR cavity PRM1 and PRM2 mirrors) it is not obvious if it can be placed there.

Another possibility would be to install the beam dump outside the injection tower and tilt the viewport enough to avoid sending back part of the rejected beam into the interferometer.

2.4. Conclusion

In order to save commissioning time, we are convinced that we should install two optical systems that can be used to adjust the laser power. A first one has to be installed before the IMC cavity, the second one at the ITF input port after all the optical elements affected by laser beam heating such as the in-vacuum faraday isolator.

3. Beam Jitter

3.1. Current status and noise projections

New quadrant diodes have been produced recently. They have been installed in March 2009 and provide a good measurement of the input beam jitter up to several hundred Hz.
Figure 15 is a plot of the current input beam jitter.
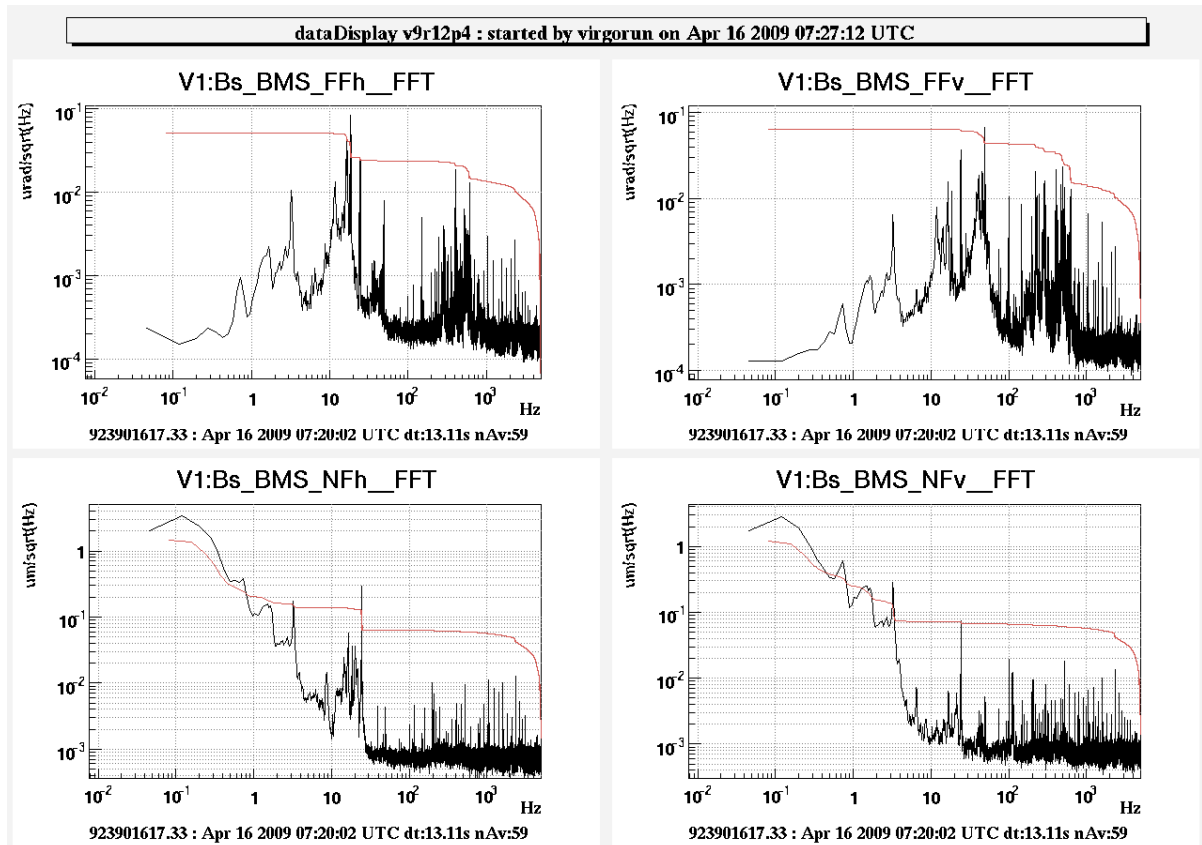
Figure 15: Virgo+ beam jitter.

The input beam jitter is known to be due to the motion of the optical table from 1-3Hz (full coherence between beam jitter and seismometer on the optical table). Below these frequencies, many experiments pointed out the problem of air currents. This has been improved in the past by improving the baffling of the beam path. There exist currently 2 baffles: the acoustic enclosure and an additional Plexiglas cover.

Some tentative jitter noise projections have been done in the past. The most conclusive ones are the projection of the seismometer signals placed on the optical table (calibrated with a shaker placed also on the bench). Here is the most recent noise projection (see Figure 16). Direct noise corresponds to input beam jitter while the up-converted noise corresponds to some other noise coupling mechanism (backscattered light).
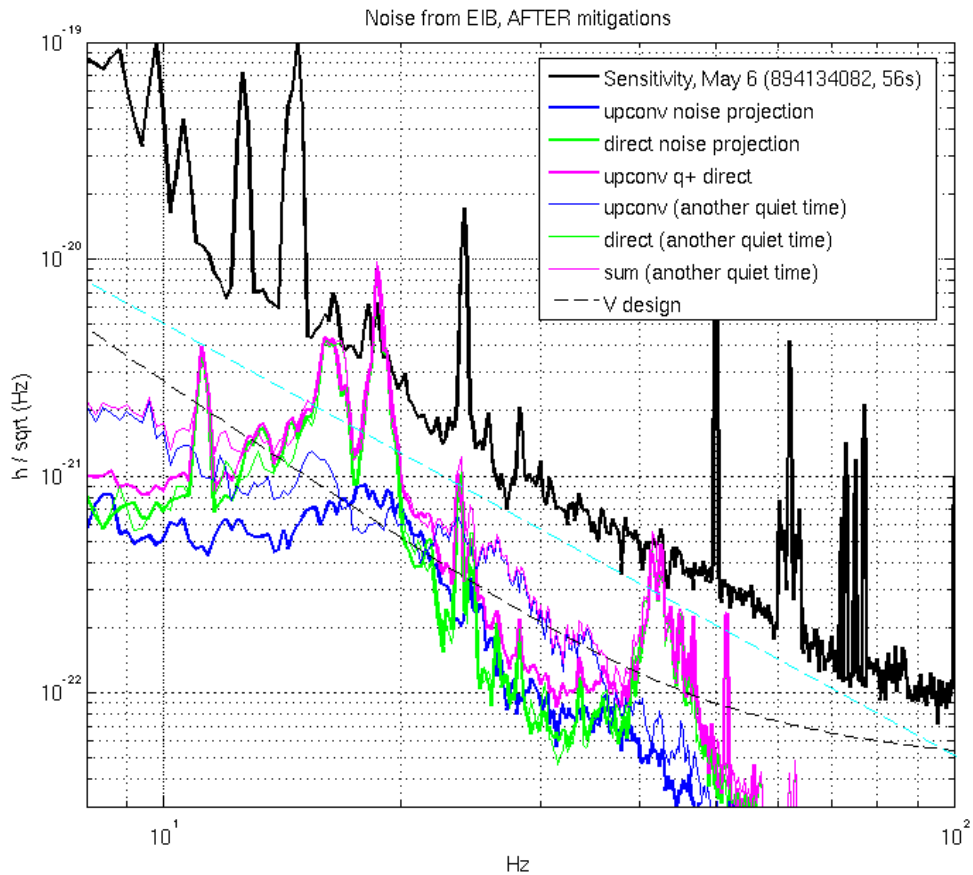
Figure 16: EIB noise projection onto Virgo sensitivity curve.

The peaks at 18Hz and 42Hz come from the optical table itself (demonstrated by measuring the mechanical TF between the ground and the bench). This could be fixed in the future by improving the stiffness of the optical table. At that point the projection of input beam jitter noise expressed in h would stand just a factor 2-4 below the Virgo sensitivity.

One must add that the main source of beam jitter is the seismic motion of the bench, although this is not the only source. There are also a few peaks at few hundred Hz which corresponds to the mechanical resonance of some optics on the input beam path, in particular the optics mounted on PZT to control the pointing of the beam. This has to be further studied but could be improved by having lighter optics/mounts.

3.2. Requirements after IMC

One cannot base entirely the requirements for AdV on the current noise projections. There are 3 reasons for that: the coupling of the input beam jitter to the dark fringe will be different in AdV because the optical layout of the recycling cavity will be different and because AdV will have a DC detection scheme instead of an AC detection scheme. The third reason is that the power stabilisation system may need higher requirements as it is usual the main limitation is coming from bema jitter coupling with sensor non-homogeneity.

The coupling of the input jitter to the dark fringe will also depend on the tilt motion of the recycling cavity mirrors.

A serious study with dedicated simulation tools is needed to establish the requirements [11].

3.3. IMC filtering

The IMC cavity can filter part of the input beam jitter. It depends on its finesse, length and alignment accuracy. One has to underline that, due to its geometry, the IMC will filter in a different way the 4 degrees of freedom of the input beam jitter. These attenuation factors have to be carefully computed.

Because higher-order modes are suppressed by the input mode cleaner, beam jitter is also decreased. The amplitude of the suppression is:

$$A_S = \sqrt{\frac{T_{mn}}{T_{00}}} = \sqrt{\frac{1}{1 + \left(\frac{2}{\pi} F \sin\left(\frac{2\pi\Delta\upsilon_{mn}}{c} L \right) \right)^2}}$$

(13)

where $\Delta\upsilon_{mn} = \frac{c}{2L}(m+n)\frac{1}{\pi}\arccos\sqrt{g}$ and $g = 1 - L/R_C$; R_C is the end mirror radius of curvature.

The filtering efficiency depends on the factor $\frac{2}{\pi} F \sin\left(\frac{2\pi\Delta\upsilon_{mn}}{c} L \right)$ and has to be as high as possible

for the lower-order modes in order to minimize the beam jitter.
See section 4.7 for more details.

3.4. How to meet the requirements?

Depending on the final requirements for the 4 degrees of freedom, there are various options to improve the current input beam jitter.

First, the location of the Mode Matching Telescope for the IMC and its design has to be carefully studied. Indeed, as it expands the beam by a factor α, it also multiplies the shift coupling of the bench where is located the telescope by the same amount. Besides, the shift/angle, angle/shift and angle/angle coupling depends on the design of the telescope.

Of course, the optical tables could be suspended and a Local Control system could be implemented to control the bench position as it is already done for the optical tables suspended in the towers. The complexity of the suspension will depend on the requirements for the jitter and for the backscattering.

It is more delicate to deal with the air current issue. Obviously, the baffling could be improved and the source of heat could be removed from these covers. But it is difficult to make projections. It is also important to say that the laboratory where stand these optics need to be kept in over pressure for obvious cleanliness issues which make difficult the fixing of air currents.

4. Input Mode Cleaner cavity (IMC)

The input laser light of the interferometer must be frequency and spatially stabilized. The IMC provides active frequency stabilization through feedback to the laser system, passive frequency noise and power fluctuation suppression above its cavity pole frequency, and passive spatial filtering at all frequencies. In particular, as it reduces higher order modal content of the laser light, the IMC suppresses part of the input beam jitter. Here are discussed the main design choices: the geometry, the length and the finesse with respect to the various issues.

4.1. The IMC geometry

The current geometry (triangular cavity) is, of course, one of the 2 possible configurations discussed here. The other possible configuration is a "bow-tie" one.

These 2 configurations comply with the main design requirement: they separate naturally the input beam from the reflected beam and the transmitted beam (ring cavities). They are also compliant with the astigmatism requirements.

There are mainly 2 differences between these configurations: they have different properties for what concerns the backscattering issue and the LG33 compliance.
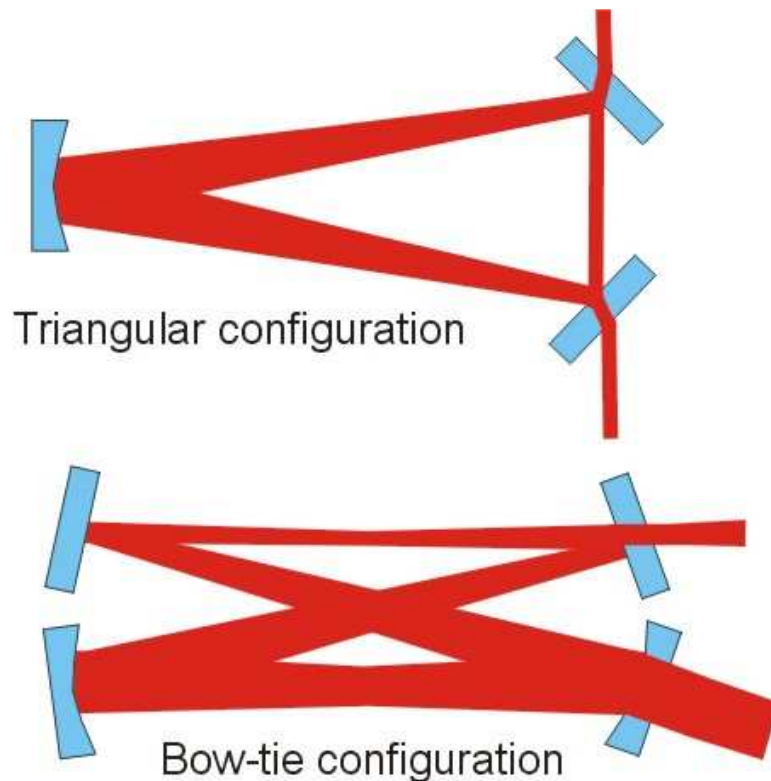
Figure 17: IMC cavity possible geometries.

In the triangular configuration, the problem is well known. Let's describe it again. The light reflected by the interferometer goes back to the IMC and is then transmitted back towards the laser system. The problem is that part of this light is scattered by the end mirror and, because the angle of incidence on this mirror is very small (around 3.10^{-4} rad for a 150 m long triangular cavity), a non-negligible amount of this scattered light is then resonant again in the same direction as the input beam. In particular, this light reaches all the sensors placed in reflection of the cavity and interferes with the light reflected by the IMC. This interference is due to the length fluctuations between the interferometer and the IMC and consequently spoil the signals used to control the IMC [12].

The principle is similar for both configurations, "bow-tie" and triangular configurations. But, actually, it is worse for the bow-tie configuration, since the incident angle is small on all 4 mirrors, meaning one has to take into account the light scattered by all 4 mirrors.

Concerning LG33 modes, it has been shown that the triangular cavity does not transmit properly the LG33 mode ([13]). As this mode is an option for future upgrade of AdV, it would be worth looking at which kind of ring cavity could transmit in a proper way this LG33 mode. The Bow-tie ring cavity may be a good candidate since having an even number of mirror is necessary to transmit properly LG33 mode. But, no detailed studies have been carried out until now.

4.2. The low pass filtering effect

The IMC cavity behaves as a first order low-pass filter for amplitude and frequency fluctuations of the input laser beam.

$$H(f) = \frac{1}{\sqrt{1 + \left(\dfrac{f}{f_0}\right)^2}}$$

(14)

where f_0 is the IMC cavity pole ($f_0 = c/4LF$, L: cavity half round-trip, F: cavity finesse).
A length of 150m with a finesse of 1000 corresponds to a pole at 500Hz.

4.3. The astigmatism issue

The triangular shape introduces some astigmatism in the beam transmitted by the cavity. This is directly linked to the length of the cavity. But, it is actually negligible. For a 15m long cavity, with a triangular base of 9 cm, the discrepancy between horizontal and vertical beam waist is of the order of 0.01%.

4.4. The thermal effects issue

The most critical thermal effects are located in the input and output mirrors of the cavity due to the absorption of the coating. Some computations should be made to know if thermal effects affect more or less a long or short cavity for the same Gouy phase propagation.

4.5. The compliance with the frequencies of modulation

The sidebands of the frequencies of modulation used to control the interferometer have to be resonant into the IMC. So these frequencies of modulation have to be a multiple integer of the IMC FSR. For a 150 m long cavity, that means that all multiples of around 1 MHz can be chosen as frequencies of modulation. If the cavity is only 15m long, only multiples of 10 MHz can be chosen.

4.6. The back-scattering issue

Due to the small angle of incidence on the IMC end mirror, some light is scattered by this mirror in the opposite direction inside the IMC cavity. This back scattered light can create some control problems at the level of the IMC cavity (generation of fringes). This effect can be easily explained by the fact that the IMC cavity is behaving as a mirror of definite reflectivity and we have an uncontrolled cavity that consists of the IMC and power recycling mirror. This is illustrated in Figure 18.
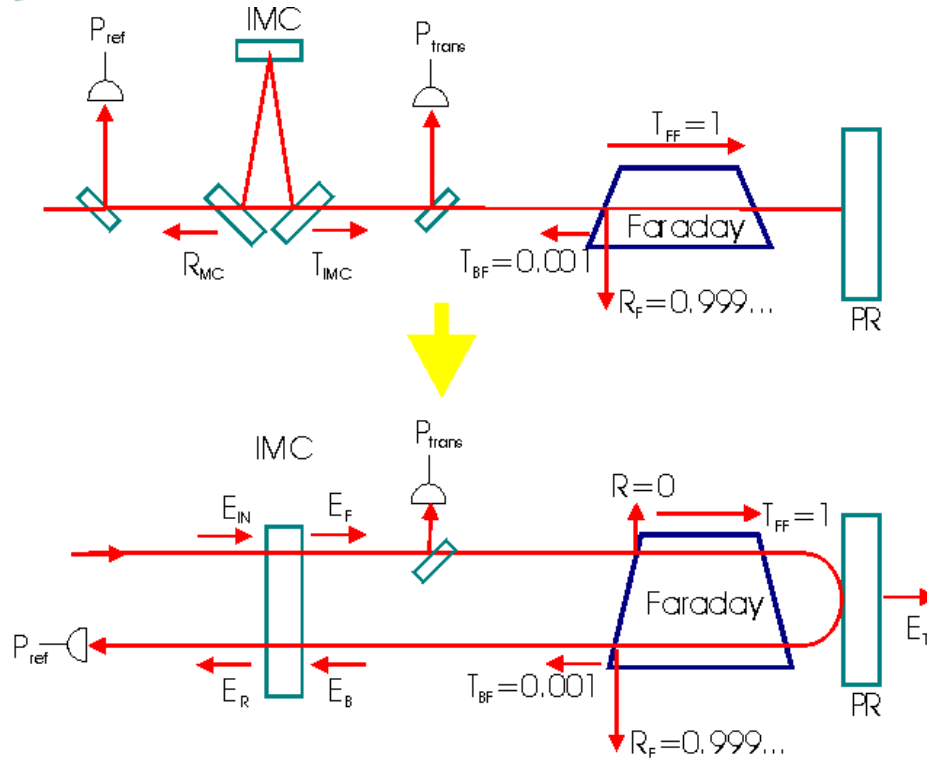
Figure 18: Cavity IMC-PR- IMC cavity can be seen as a simple mirror of reflectivity R_{eff_IMC} .

One can estimate in a simple way the effective reflectivity of the IMC cavity as function of $R_{back-scattering}$ [21] which is the power coupling coefficient of the back-scattered light in the cavity mode (estimated to be about 10^{-7} if the beam is centered on the IMC curved mirror) as follows:

$R_{eff\_IMC} = G^2 R_{back-scattering}$

where $G = F/\pi$ is the cavity gain (F is the cavity finesse).

In past experience of Virgo, the effective reflectivity of the IMC has been measured to be 300 ppm [15] with the Faraday corresponding to some fluctuations of the IMC transmitted power of 10% amplitude when there was no faraday isolator between the IMC cavity and the Power Recycling mirror.

The reflectivity of the IMC has also been evaluated directly from the wavefront map of the mirror [16]. For the old IMC end mirror, this reflectivity was evaluated to be 1.10^{-8} in intensity, that is to say an effective reflectivity of the IMC of 1200 ppm for a finesse of 1100. The difference with the measurement is quite high (300 ppm) and can be explained partially or completely by the depolarization effects in the Faraday which are changing the spatial distribution of the light transmitted by the Faraday so that the residual light transmitted by the Faraday does not couple well inside the IMC (which explains the additional isolation).

Recently, some computations have been performed by Mikhael Pichot (Artemis group) using DarkF software in order to evaluate the current backscattering we have with the new IMC end mirror and the part of back-scattered light that is re-coupled into the IMC cavity and that is travelling in reverse way respect to the beam coming from the laser. The result of this work is given on Figure 19.
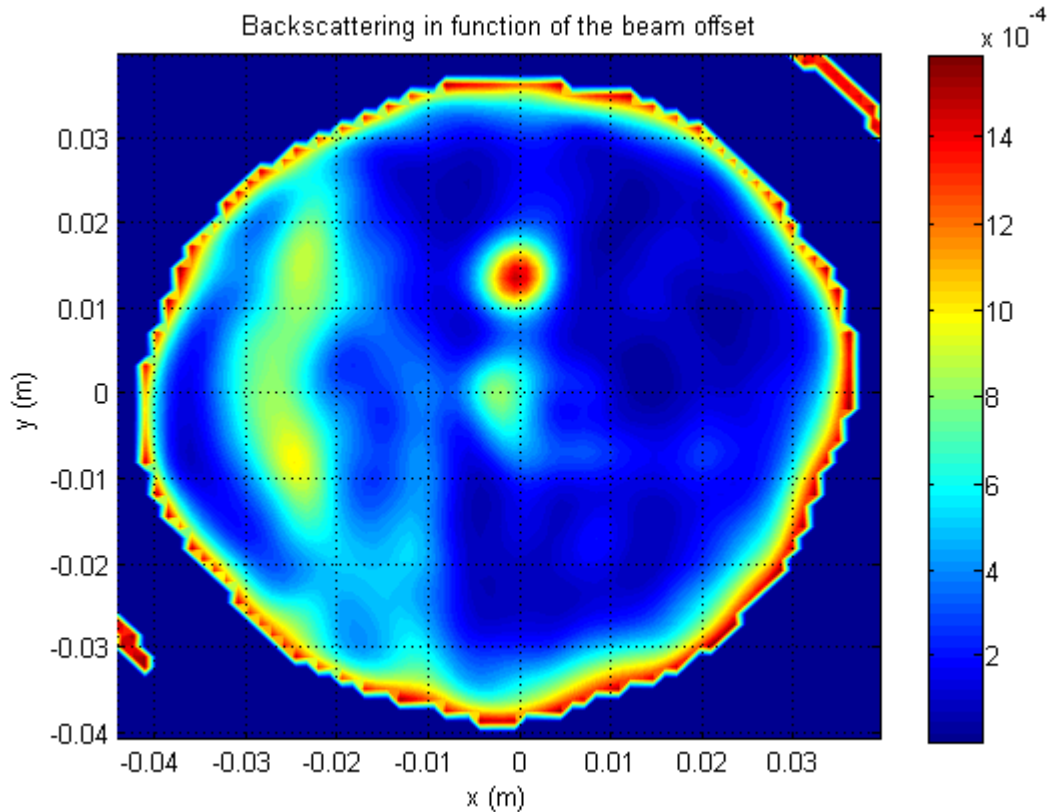
Figure 19: Amplitude of back-scattered light coming from IMC end mirror re-coupled in the TEM_{00} mode and travelling backward in IMC cavity.

As can be seen on Figure 19, the back-scattered light re-coupled into the IMC cavity mode for a beam centered on the curved mirror is about 5.10^{-4} in amplitude (see color bar in the figure), so 2.510^{-7} in intensity (for a beam radius of 11mm) that is to say an effective reflectivity of 30000 ppm for a finesse of 1100, so a factor 25 worse with respect to the old mirror.

As already said, if the effective reflectivity of the IMC is of the order of a few hundred ppm, all IMC controls are spoilt by the cavity formed by the PR and the IMC. After the installation of the faraday isolator, this problem was fixed thanks to the additional attenuation of a factor 1000, leading to an effective reflectivity of 0.3 ppm (with the old IMC end mirror). The Faraday has been then further upgraded to compensate for some depolarization effects reaching an isolation of 50 dB (logbook # 21182) which was actually useful since the IMC end mirror was changed at the same time and found to be much worse in terms of scattering with respect to the old one. Even if the real effective reflectivity has not been measured, it can be assumed to be less than 1ppm.

This experience can help us to set requirements on the effective reflectivity of the IMC end mirror. We can assume that an effective reflectivity lower than 1ppm is a good requirement.

So, the effective reflectivity of the IMC depends on the square of the finesse of the IMC, on the square of the RMS roughness of the IMC end mirror [18] and on the Faraday isolation.

For a finesse of 1000, and a back-scattered reflectivity of 10^{-8} , there is the need for a Faraday isolation of 30dB.

According to the performance study of UHV faraday isolator [17], the maximum isolation ratio could be a bit higher than 40 dB with AdV laser power.

If the finesse is 100, and if the back-scattered reflectivity is 10^{-9} (corresponding to a better polishing: roughness RMS < 1nm), there is no need for a Faraday isolator (but there is no margin).

4.7. The High Order Mode filtering effect

Because higher-order modes are suppressed by the input mode cleaner, beam jitter, in particular, is also decreased. The amplitude of the suppression is given in equation 13.

The filtering efficiency depends on the factor $\frac{2}{\pi} F \sin\left(\frac{2\pi\Delta\upsilon_{mn}}{c} L\right)$ and has to be as high as possible

for the lower-order modes in order to minimize the beam jitter.

To satisfy this condition F has to be as high as possible and the IMC has to be non-degenerated, i.e., $(m+n)\arccos\sqrt{g} \neq n\pi$ (n is an integer).

Considering that the AdV power recycling cavity will be non-degenerate, this cavity will also contribute to beam pointing filtering as well as the IMC cavity. This optical configuration will put less stringent requirements on the IMC jitter filtering efficiency. Advanced LIGO specifications in terms of beam jitter has been used to give a preliminary requirement for AdV [2]. Beam pointing noise specifications for AdV are not known but should be of the order of 10^{-10} rad/$\sqrt{Hz}$ for $f > 10$ Hz after the input mode cleaner (factor of 10 better than for Initial Virgo)[24].

Considering that the beam jitter after the PMC cavity should be of the order of 0.01 μrad/$\sqrt{Hz}$ from 10Hz (see Virgo+ presentation on beam jitter (10/2007)) the required filtering factor from the optics between the PMC and PR cavity should be higher of 100. As seen in equation 13, the filtering efficiency of the IMC is about $1/F$ and if the beam expanding telescope between the PMC and the IMC has a magnification factor M (=3 for example). The output beam will not only have M-times the beam radius, but also $1/M$ the r.m.s. value of angular fluctuations.

Considering that the input mode-cleaner controls are stable enough to not reintroduce beam jitter noise due to Suspended Mode-cleaner motion. The IMC jitter suppression factor should be at least 30, if we want to fulfil the requirements meaning that F should be higher than 30.

This should enable us to decrease IMC cavity finesse down to probably 100 but further detailed investigations on beam jitter are needed to confirm this statement because for this estimation we are not taking into account laser and external injection benches residual seismic motion that could contribute in a non-negligible way to input beam jitter (it is likely that in-air benches will have to be suspended).

4.8. IMC throughput and IMC losses

The throughput of the cavity depends directly on the losses and on the finesse of the cavity. So the choice for the finesse is limited by the amount of losses if 90% of throughput is required.

The throughput can be estimated using the following formula:

$$IMC_{Throughput} = \frac{4\,T_1 T_2}{(T_1+T_2+L_{RT})^2} \qquad (15)$$

where T_1, is IMC input mirror transmission, T_2, is IMC output mirror transmission and L_{RT}, IMC cavity round-trip losses. For the IMC, $T_1 = T_2 = T = 2450$ ppm.
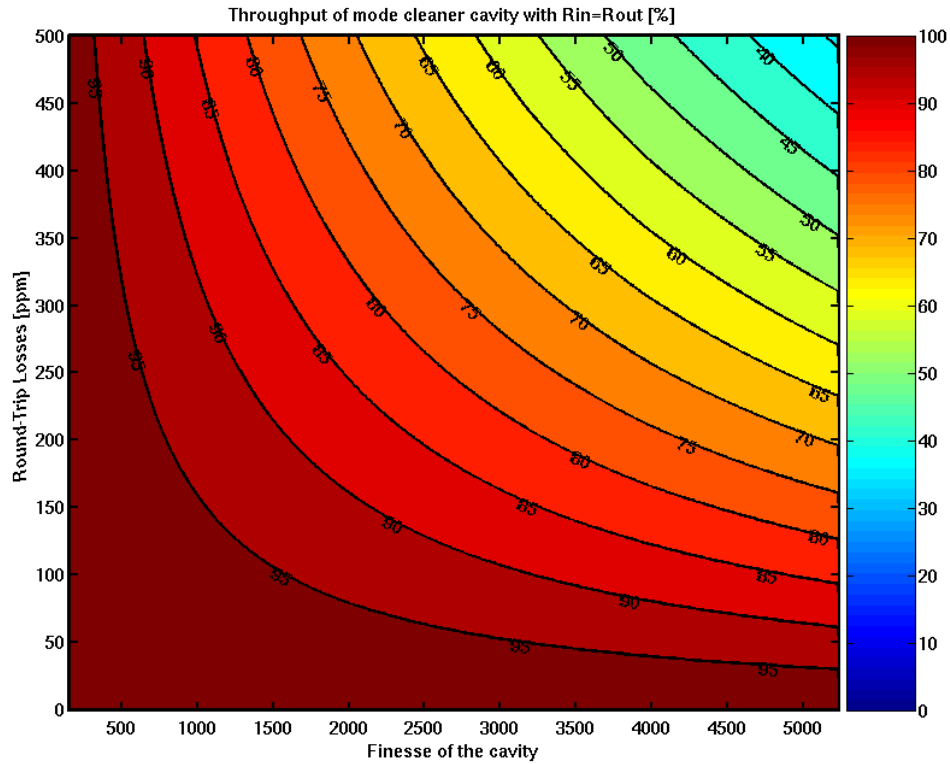
Figure 20: IMC throughput vs Finesse and round-trip losses.

On Figure 20, we have plotted the IMC cavity throughput as a function of the Finesse and the round-trip losses of the cavity. As you can see to fulfil the requirements, we need to get round trip losses lower than 300 ppm if the finesse is 1000.

Some simulations with DarkF have been carried out by Mikhael Pichot (From Artemis group) starting from the simulation results given in a Virgo internal note [45] to compute round-trip losses using IMC mirror maps provided by LMA.

NB: mirror maps of the Virgo + IMC mirror have been used in this work (C08009).

Mirrors	C08009 with In/Out mirror rms 1nm	C08009 with In/Out mirror rms > 7 nm
IMC transmission	93.58%	84.27%
Round-trip losses	104ppm	371 ppm

Table 2: DarkF simulation results considering Virgo+ IMC end mirror and for 2 different roughnesses for IMC flat mirrors.

Table 2 gives the results using the mirror maps given by LMA-Lyon.

The roundtrip losses are presently of the order of 370 ppm and the transmission of the IMC should be around 84%. It is very close to what has been measured in Virgo [32].

The losses are due to the fact that mirror imperfections, at the level of a few nm RMS, modify the beam shape and spread some energy out of the reflecting part of the coatings.

As you can see in Table 2, round-trip losses are very small if we reduce the roughness of IMC flat mirrors.

These round-trip losses could be even better by improving the roughness of IMC curved mirror that is for Virgo+ around 2.8 nm.

4.9. The thermal effects issue

The most critical thermal effects are located in the input and output mirrors of the cavity due to the absorption of the coating (the power absorbed by the substrate is considered negligible with respect to the power absorbed by the HR coating). A preliminary study has shown that thermal effects in the IMC cavity are not depending on the cavity length and, to the first order, on the cavity beam waist. This study has also shown that it is better if the beam waist is located on the cavity input mirror.

It turned out that thermal effects become non-negligible for an absorbed power higher than 100 mW. For example, if we consider a coating absorption $abs = 1$ ppm, $P_{Laser} = 200$ W and a finesse F=1000, the power absorbed by the coating is about 60 mW.

However, astigmatism will become an issue if we have thermal lensing due to absorption in input mirrors as it is shown by Barriga et al. [14] and as demonstrated on the Virgo interferometer [32]. We will need to take particular care to select IMC input and output mirrors with as little absorption as possible in order to reduce this effect and not to limit the beam matching onto the Interferometer.

Substrate and coating absorption of the IMC mirrors will lead to changes in the radius of curvature of the 3 IMC mirrors [19], and in particular to lensing effects in the input and output mirrors. Evaluation of the output beam characteristics has to be given in order to foresee a compensation of this thermal effect is necessary. Depending on the possible compensation to recover the beam, the finesse of the cavity may be limited by these effects.

4.10. The radiation pressure issue

The IMC and ITF mirrors will be subjected to incremental radiation pressure changes as the input power is changed. An internal Virgo note, Salem Hebri [20] has demonstrated that it should be possible to lock the IMC with an incident power of 180 watts with a IMC end mirror mass at least of 900 g. Thus, one should understand that taking an IMC end mirror heavy enough, there should not be any problems to lock the IMC even the presence of the radiation pressure.

Nevertheless, it is interesting to take a look in more detail at what we can expect according to the cavity finesse F and laser power coupled in the cavity.

Hereafter only the static radiation pressure effect is considered.

A laser beam incident on a mirror applies a force given by:

$$F_{rad} = 2P_{stored} / c \qquad (16)$$

where c is the speed of light and P_{stored}, the power stored in the IMC cavity.

$$P_{stored} = FP_{Laser} / \pi \qquad (17)$$

We can write eq.16 as:

$$F_{rad} = \frac{2FP_{Laser}}{\pi c} \qquad (18)$$

The radiation pressure force on the IMC mirrors has been computed as a function of the cavity Finesse and laser power coupled in the IMC cavity.
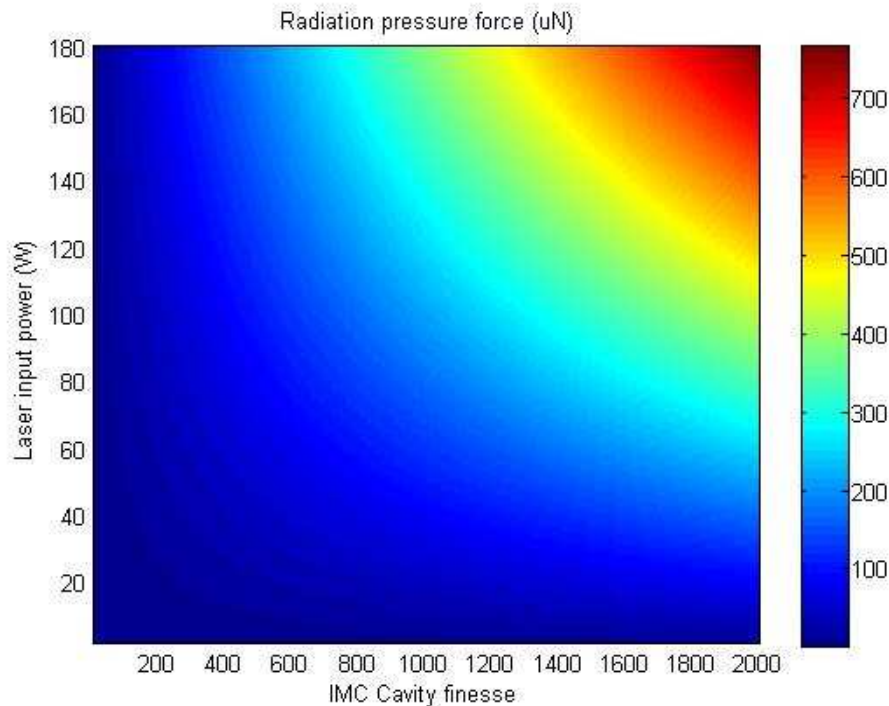
Figure 21: radiation pressure in the 144m triangular IMC cavity respect to

laser input power and cavity finesse.

At maximum, we get about 800 μN for a finesse of 2000 and a laser input power of 180 W (see Figure 21).

It has been shown in a recent Virgo internal note [23] that a radiation pressure force $F = 400$ μN (Finesse = 1000, Laser power =180 W, IMC length =144m)*,* induces a frequency shift $\Delta f = 35$ MHz (Finesse = 1000).

If we use the same locking strategy as Initial Virgo, the actuation range should be large enough to deal with the radiation pressure effect (the master laser piezo actuator actuation is 1.75 MHz/V and we are able to apply +/-100 V).

In any case the lock could be acquired at low power where the radiation pressure is negligible and then we could keep the IMC cavity locked up to full power by using the Input Power Control system that will be installed before the IMC cavity (see section 2.2 for more details) and will enable us to slowly ramp up the power up to 180 W.

The only point that needs to be further investigated concerns the angular control of the cavity.

In fact if the beam is not well centered on the IMC curved mirror, the radiation pressure will generate a torque that will have to be compensated by the IMC alignment sensing and control system.

This servo loop will have to be fast enough to keep the IMC cavity aligned. Some further checks on this topic are needed but we think that if the IPC system is slow enough we shouldn't have any problems with this specific point.

Nevertheless, the effect of radiation pressure on the IMC end mirror angular degrees of freedom has been studied. A note has been released on this issue [23].

The radiation pressure effects in the IMC cavity have been studied using both analytical and numerical approaches for the θ_x mode. The results show that also with Virgo+ configuration (IMC end mirror mass = 1.4 kg) the effects of radiation pressure will modify the mechanical transfer functions but the unstable configuration will not be reached with AdV laser power (see Figure 22).
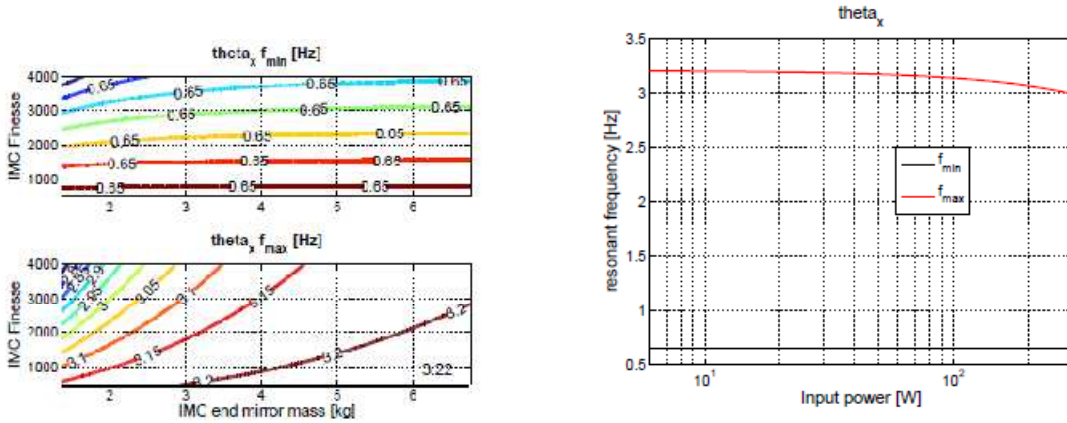
Figure 22: left plot: θ_x resonant frequencies change (due to radiation pressure) with IMC curve mirror mass and IMC cavity Finesse; right plot: Frequency change due to radiation pressure for F=1100 and $M_{IMCcurvedmirror}$=1.4 kg.

For the θ_y mode the situation is more critical since it cannot be modeled by the present simulation tools and it is complex to solve it analytically.

Some measurements have been recently performed on the Virgo IMC and it has shown that the resonant frequency of the IMC end mirror suspension for this d.o.f increases with power starting from 1.315 Hz. From 0 to 12 W, the frequency increases by about 0.1 Hz and it is expected to increase by more than 1 Hz for 200 W laser power.

It would be better to raise the mirror mass, up to about 3 kg, in order to have a larger safety margin in order to face with easier angular control strategies.

Radiation pressure noise could also be responsible for frequency noise since it can affect the length of the IMC cavity and the angular control of the IMC end mirror if the beam is not well centered on this mirror. In "linear regime", it has been shown that radiation pressure noise is not an issue for Initial Virgo sensitivity[22]. Since it has been demonstrated that for Virgo we are already 4 orders of magnitude below the sensitivity meaning that this noise should not be an issue for AdV since this noise is proportional to the power stored in the IMC cavity. Considering the same finesse F and a 144 meter long cavity, this noise is at maximum about 4. $10^{-27} / \sqrt{Hz}$ over the whole sensitivity bandwidth meaning that we are well below the AdV sensitivity that should be about 3. $10^{-24} / \sqrt{Hz}$ at 300Hz [8].

4.11. Conclusion

There are no mature studies for the bow tie cavity configuration. Besides, the scattering issue would be 4 times worse and the alignment/longitudinal control would be far more complicated. This option would require a huge design study effort and consequently should be reconsidered only when LG33 will be a serious option for an upgrade of AdV.

The scattering from end mirror issue can be overcome without shortening the IMC. So there is no strong motivation to change the Initial Virgo IMC length.

There are 2 options for the finesse….

First option: the finesse has to be as high as possible and its choice is limited by the losses of the cavity (constraint on throughput), the thermal effects (depending on corrective system efficiency) and radiation pressure effect. To be conservative, F=1000 should be ok according to what has been discussed in the previous sections but further studies are required

Second option: the finesse has to be low enough to be able to remove the Faraday isolator, but still high enough to filter sufficiently the beam jitter noise… Preliminary considerations seem to show that we could lower the IMC finesse down to 100. A detailed study is needed to confirm this statement.

5. Reference cavity (RFC)

A reference cavity (RFC) is used to pre stabilize laser laser frequency during the lock acquisition to get the frequency stability that is small enough to lock the long arms (typically, it should be of the order of 4 Hz rms for AdV[24]). The frequency pre-stabilization is needed only as long as the Second Stage of Frequency Stabilization is not engaged.

The reference cavity according to the INJ block diagram should be installed after the IMC cavity on a pick-off beam just before entering the Interferometer.

Since we will probably have limited space on the suspended injection bench to integrate all the components needed for AdV, due to the fact that the SIB of AdV could accommodate many big and heavy components (high power compliant Faraday isolator, Power recycling cavity mirror PRM1, IMC input and output mirrors), the real need of placing the RFC suspended below the SIB should be reconsidered.

5.1. Why the RFC is presently suspended?

The decision to suspend the RFC, under the SIB, originates from the evaluation of VIR-NOT-LAL-1380-051 [25]. There is essentially no subsequent computation about this subject.

After the first decision to suspend the RFC, any later setup assumed this configuration. The reason was based essentially on the fact that the suspended RFC had worked, there was no reason to change this configuration, it seemed in any case to benefit from the SIB seismic isolation, and it was possible, without any major drawback, to attach the RFC to the SIB.

At that time the frequency pre-stabilization was quite different from the one currently used in VIRGO. The requirements on the frequency pre-stabilization were not quite clear.

There are several reasons for reconsidering this decision:

- The actual seismic noise in the injection area (e.g. benches in the laser laboratory) is now known, and could be different from that used for the first evaluation in 1993.
- The frequency pre-stabilization topology has changed significantly.
- The needs for the frequency pre-stabilization are better known.
- The needs for AdV could be different
- It is difficult to find space and available weight for the RFC in the SIB of AdV.

In addition to that, it should be taken into account that in LIGO the RFC has also been positioned outside the interferometer vessel, in vacuum on an external bench in the laser area. There is no major drawback reported as a consequence of this choice. This configuration will be adopted also in Enhanced LIGO and in Advanced

LIGO. Specifications on RFC frequency control for AdV are reported in AdV INJ design requirement document [24]

According to that, at present it should be assumed:

Δν < 4 Hz RMS integrated down to 10 Hz.

5.2. New computation

5.2.1. Vibrations

We assume that in VIRGO the level of the pre-stabilized laser was at about 0.2 Hz/sqrt(Hz) between 0.1 and 10 Hz, and an RMS of about 3 Hz (smaller than the ITF cavity line width). Figure 23 shows a measurement of the frequency noise of the pre-stabilized laser in VIRGO before the closing of the SSFS loop.
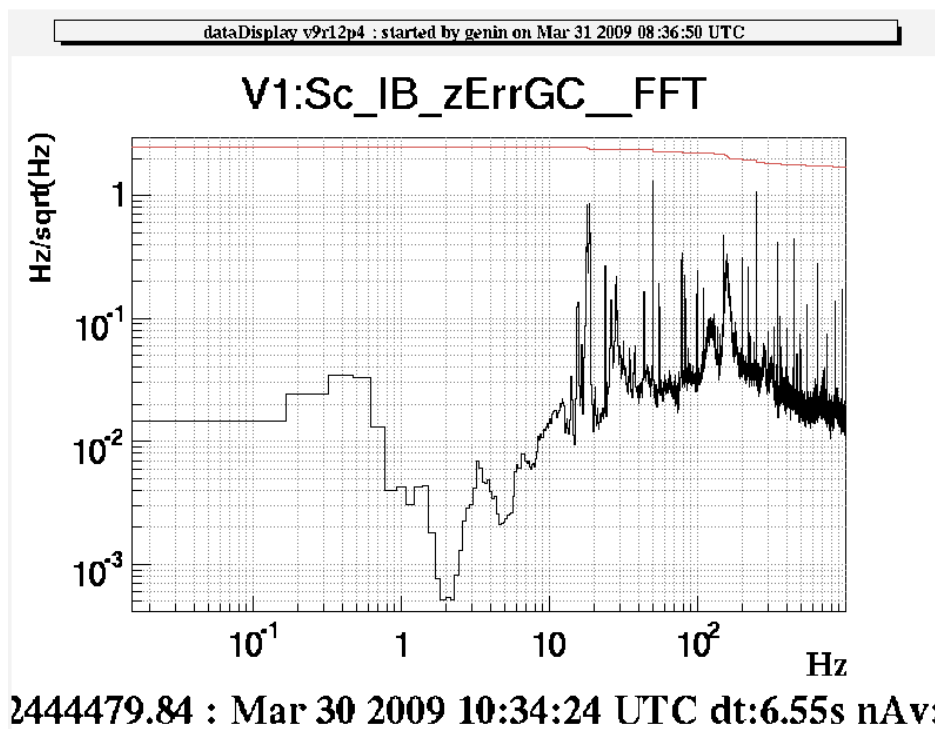
Figure 23: Frequency noise of the pre-stabilized laser, before closing SSFS.

The measured frequency noise satisfies the requirements reported in VIR-NOT-LAL-1380-051 between 0.1 and 10 Hz, and has been sufficient for the VIRGO locking. The computation in VIR-NOT-LAL-1380-051 exceeded this value above 5 Hz.

The main reason for suspending the RFC resided in the effect of the block vibrations, when the silica block was subjected to the (horizontal) seismic noise.

We have performed again the same computation of VIR-NOT-LAL-1380-051, using the horizontal and vertical accelerometer spectrum measured on the EIB.

The assumptions are the following (same as VIR-NOT-LAL-1380-051):

mass of the silica block of the RFC	M = 13 Kg
length of the silica block	L = 300 mm
effective radius of the section of the silica block	R = 100 mm (section: S=0.013 m^2)
Young modulus of silica	Y= 6.7×10^{10} Pa

According to L. Chen et al.[26] the fractional length change of a cavity in the shape of a cylindrical block (in this case subjected to gravitational force) is given by:

$$\frac{\Delta L}{L} = -\rho \times g \times \frac{L}{Y} \qquad (19)$$

where Y=Young modulus, L=cavity length, ρ=material density, and where it is assumed that the vibration force is uniformly distributed on the silica block cross section. This expression holds for vibration wavelengths longer than the cavity in the vibration direction. Given the material dispersion relation:

$$\omega = \sqrt{\frac{Y}{\rho}} k \qquad (20)$$

where k=2π/λ is the sound propagation constant inside the material space, for ULE (Y=6.7 × 10^6 Pa), if f=ω/2π<1 kHz, we have that λ>3.9 m. Therefore, for the frequency of interest (f<100 Hz) and a cavity length of the order of 30 cm, the vibration wavelength is much longer than the cavity, and the excitation of the microscopic oscillators of the material can be considered collective.

The former expression is essentially the same used in VIR-NOT-LAL-1380-051. In addition, this note assumes a relative offset of the force application point of Offs=0.02, which should take into account of the force application point. This offset is directly multiplied to the vibration coefficient connecting cavity elongation and acceleration. Already in the note all the former assumptions are considered pessimistic.

The formula used in VIR-NOT-LAL-1380-051 was therefore:

$$\frac{\Delta L}{L} = F \times Offs \times \frac{L}{Y \times S} = Ma \times Offs \times \frac{1}{Y \times S} \qquad (21)$$

The frequency noise spectrum for a wavefront locked on the cavity length L is given by:

$$\frac{\delta v}{v} = \frac{\Delta L}{L}$$

$$\qquad (22)$$

$$\delta v = v \times \frac{\Delta L}{L} = v \times F \times Offs \times \frac{L}{Y \times S} = Ma \times Offs \times \frac{1}{Y \times S}$$

The frequency noise spectrum obtained in this way (same method as in VIR-NOT-LAL-1380-051 is shown in Figure 24.
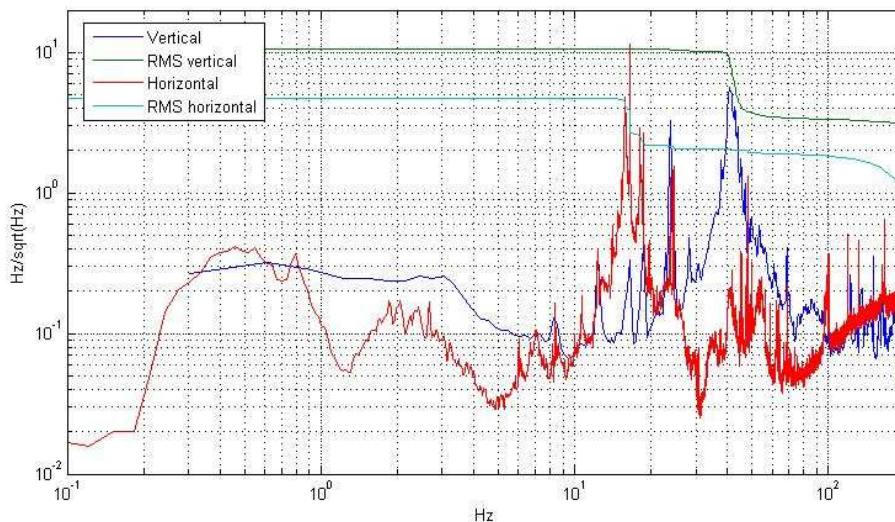

Figure 24: Frequency noise of a wavefront locked to the reference cavity on which the seismic noise measured on the EIB is active: between 0.1 and 10 Hz the frequency jitter results to be lower than 0.1 Hz/sqrt(Hz). Red: horizontal accelerometer (cyan: RMS), Blue: vertical accelerometer (green: RMS).

Figure 24 shows that the frequency jitter, computed in the same way as in VIR-NOT-LAL-1380-051, would therefore be, in the bandwidth of interest (below 10 Hz), the theoretical frequency jitter of a beam locked on a cavity, on which the seismic noise as measured on the EIB were active, should lay close to the frequency noise of the pre-stabilized laser used in Virgo, which is achieved with the suspended RFC. In particular the RMS up to 10 Hz, if the major peaks between 10 and 50 Hz (EIB table mechanical resonances) were damped, would be in the range of the AdV specs. This would mean that if the cavity were placed on the EIB, given a damping of the present mechanical resonances, this could be acceptable for the frequency jitter performance of the Virgo pre-stabilized laser.

It should be noted that the computation method used above is performed in pessimistic conditions (force acting uniformly on the surface, application force relative offset of 0.2), and it is likely that the vibration action on the silica is overestimated. A reliable computation of the cavity elongation due to the EIB seismic vibration would need a FEM simulation. We think that the results above, however, would justify considering the possibility of moving the cavity outside of the IB tower to the EIB, and a more precise evaluation of the real frequency noise in these conditions.

NB: Estimations of frequency noise given above are reliable only below 200 Hz since episensors used to measured EIB motion have a limited bandwidth of the order of 200Hz.

5.2.2. Comparison with RFC leaning on ground

Placing the RFC on the EIB has some advantages with respect to simply placing it on ground. Figure 25 shows the comparison between the frequency noise expected from the RFC on the EIB and on the ground (vertical ground seismic spectrum measured close to the IMC tube between EEroom and Laser lab).
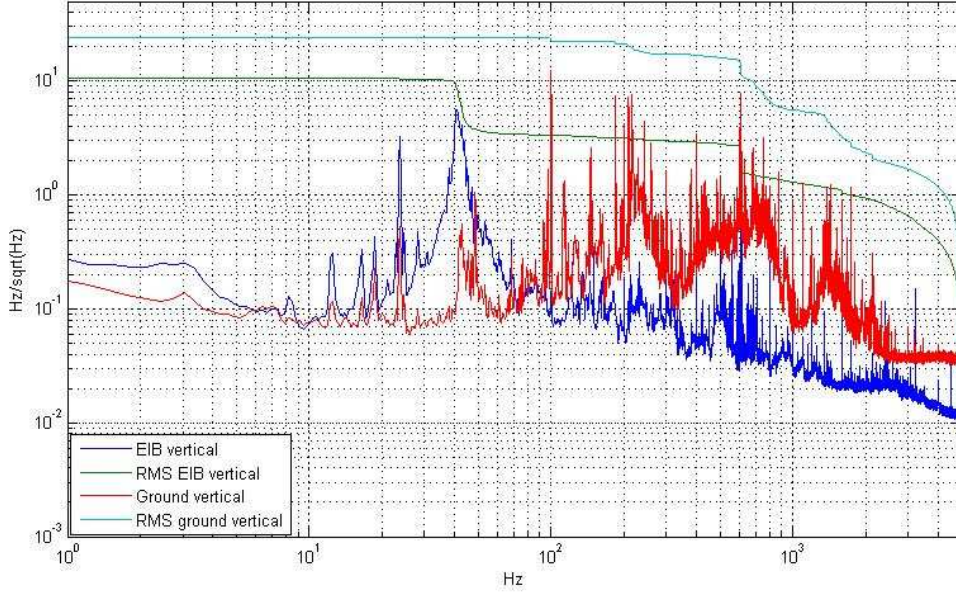
Figure 25: Blue curve: frequency noise with the RFC on the EIB; red line: RFC on ground.

5.2.3. Misalignments

The equivalent displacement noise for an optical cavity, as measured with the Pound-Drever demodulated signal, is taken from the Calloni et al. paper [27]:

$$\delta\tilde{x}(f) = \frac{\pi c}{8\nu_0 F^2}\left(\varepsilon_l\tilde{\varepsilon} + \beta_l\tilde{\beta}\right) \times \left[\frac{2sin(\alpha)}{1-\cos(\alpha)} - \frac{sin(\alpha+\theta_m)}{1-\cos(\alpha+\theta_m)} - \frac{sin(\alpha-\theta_m)}{1-\cos(\alpha-\theta_m)}\right] + \frac{4L}{\nu_0}\left(\varepsilon_l\tilde{\beta} + \beta_l\tilde{\varepsilon}\right)f$$

$$= \frac{\pi c}{8\nu_0 F^2}\left(\varepsilon_l\tilde{\varepsilon} + \beta_l\tilde{\beta}\right)\Theta(a,\theta_m) + \frac{4L}{\nu_0}\left(\varepsilon_l\tilde{\beta} + \beta_l\tilde{\varepsilon}\right)f$$

(23)

where:

$\varepsilon = a/w_0$, $\beta = i\theta/\theta_\infty$, $\cos(\alpha/2) = \sqrt{(1 - L/R_1)(1 - L/R_2)}$; $\theta_m = 2\Omega L/c$, a = displacement cavity-beam, w_0 = beam waist, θ = cavity-beam misalignment angle, θ_∞ =beam divergence, $R_{1,2}$= radius of curvature of cavity mirrors, , ε_l=low frequency cavity-beam displacement, $\tilde{\varepsilon}$ = high frequency displacement spectrum, θ_l = low frequency angular misalignment, $\tilde{\theta}$ = high frequency misalignment spectrum.

The corresponding frequency noise of a beam locked on a cavity having this length noise is:

$$\delta\nu = \frac{\delta x}{x}\nu_0$$

(24)

x being the cavity length and ν_0 the laser frequency, with the RFC parameters:

x=0.15 m

R_{curv}=0.5 m

w_0=285 μm

We can assume that $\tilde{\varepsilon}$ is given by the accelerometer measurement, $\tilde{\theta}$ is given by the accelerometer spectrum divided by a few meters (distance between laser and RFC, corresponding to the relative displacement between EIB and LB). We can assumethe presence of an automatic alignment so that ε_l is 1 mm and θ_l is 1 mrad.

In these conditions the corresponding frequency noise is shown in the Figure 26.
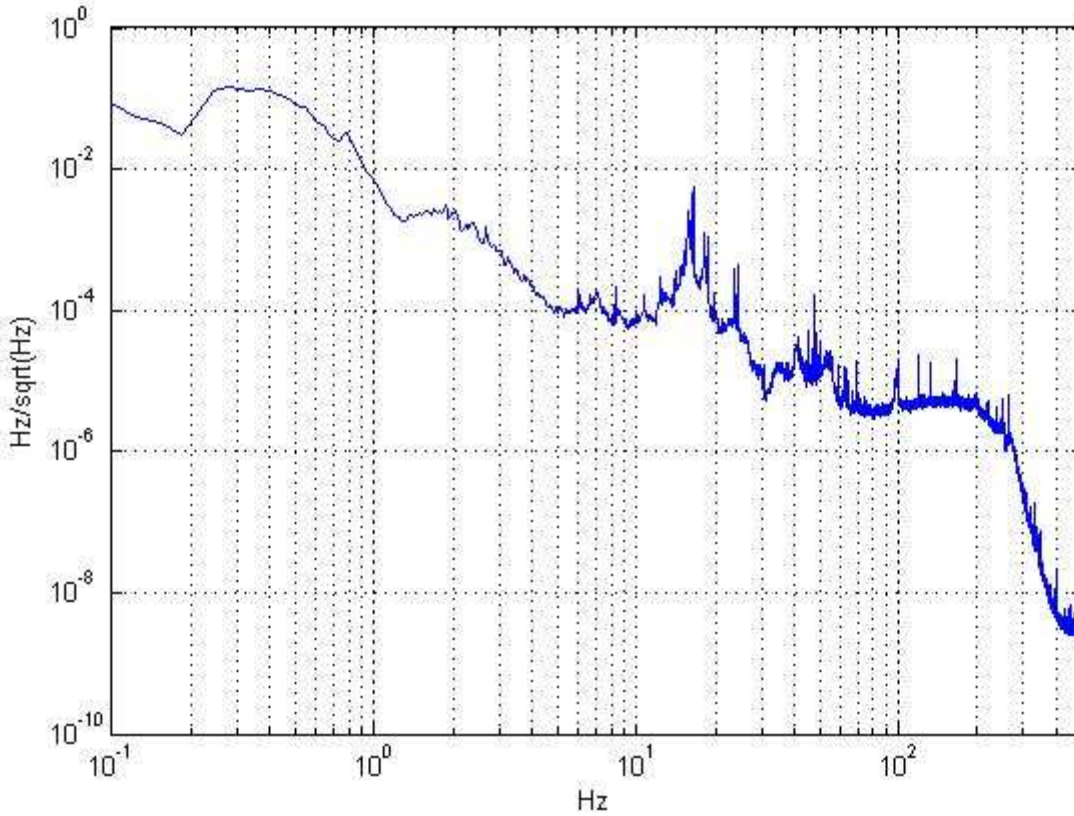
Figure 26: Estimated frequency noise coming from cavity misalignment.

It is well below the vibration level and the RFC frequency stabilization requirements.

5.2.4. Doppler

The fluctuation in frequency given by the cavity vibrations is described as a fluctuation in the phase of the light coming from the laser source to the cavity:

$$\delta\tilde{\phi} = \frac{2\pi}{\lambda}\delta\tilde{z} \qquad (25)$$

where $\delta \widetilde{z}$ is the optical path. The change in frequency is therefore:

$$\delta \widetilde{v} = \frac{2\pi v_0}{c} \frac{\partial}{\partial t}(\delta \widetilde{z}) = \frac{2\pi v_0}{c} i\omega \delta \widetilde{z} = 2\pi \frac{v_0}{c} vel \qquad (26)$$

where *vel* = Laser-cavity speed. It is therefore equivalent to a Doppler effect. The spectrum of this expression is in Figure 27.
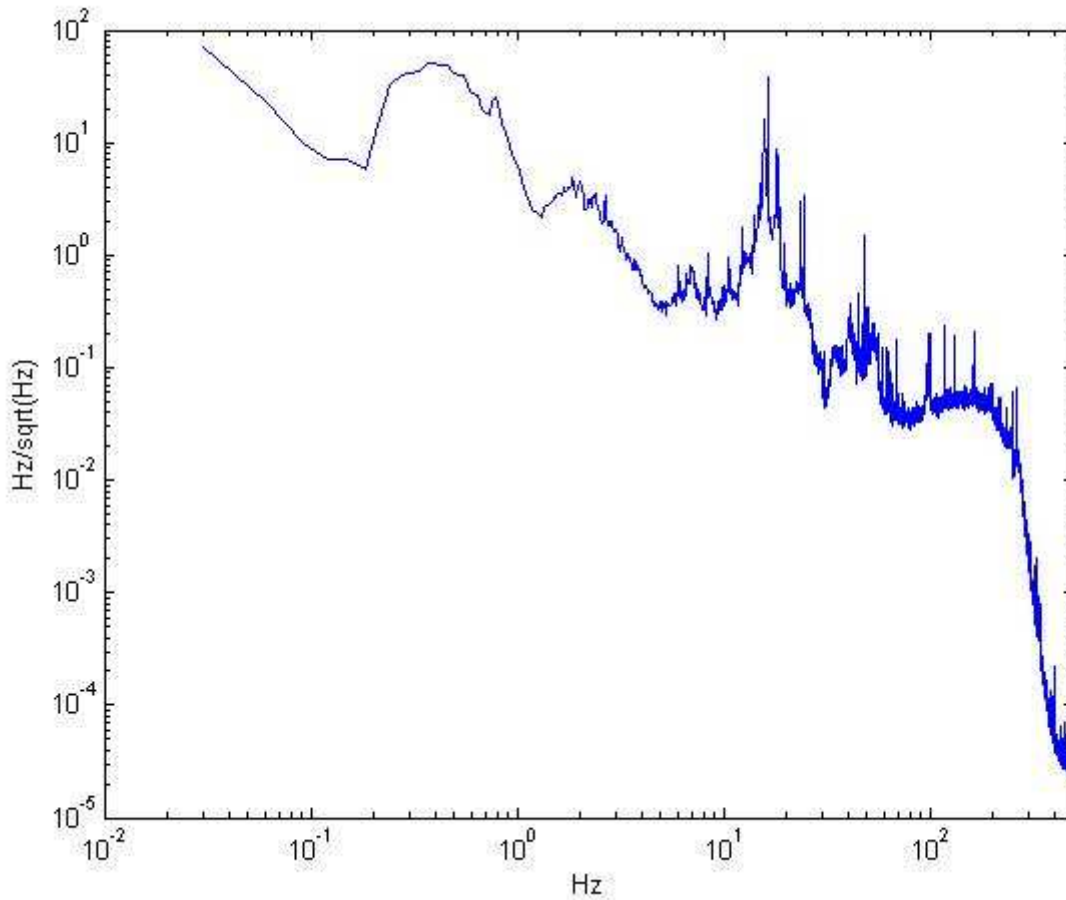
Figure 27: Estimated frequency noise putting the RFC on the EIB.

The "Doppler effect" could therefore be non negligible (TBC).

5.2.5. Suspended cavity

If the cavity is suspended to a simple pendulum stage (f_0=0.6 Hz, Q=1000, TF as in Figure 28 below), the resulting frequency noise on the RFC, in the same conditions as in Figure 24 is shown in Figure 29.
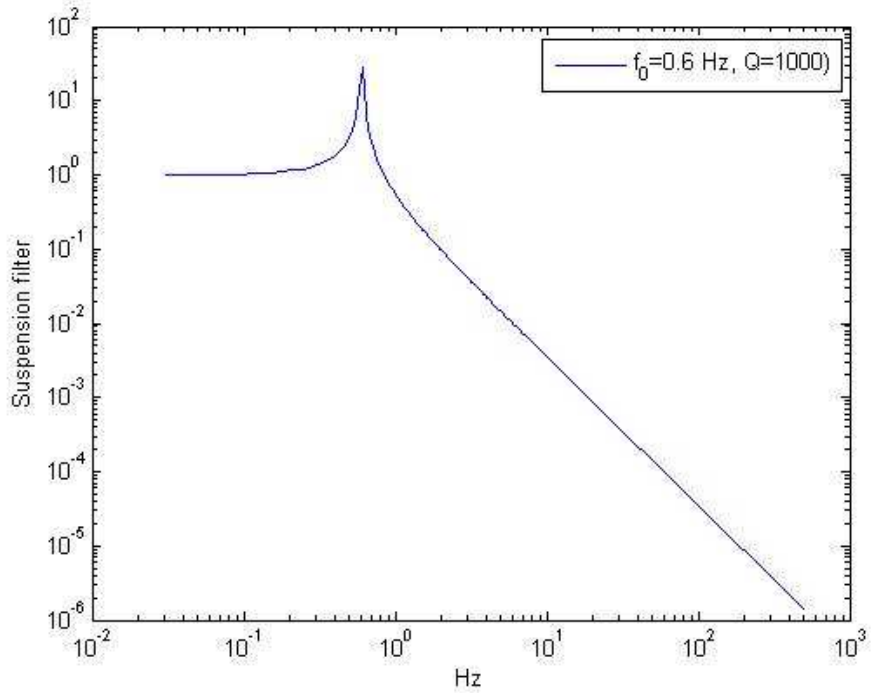
Figure 28: TF of a single stage suspension: f_0=0.6 Hz, Q=1000.
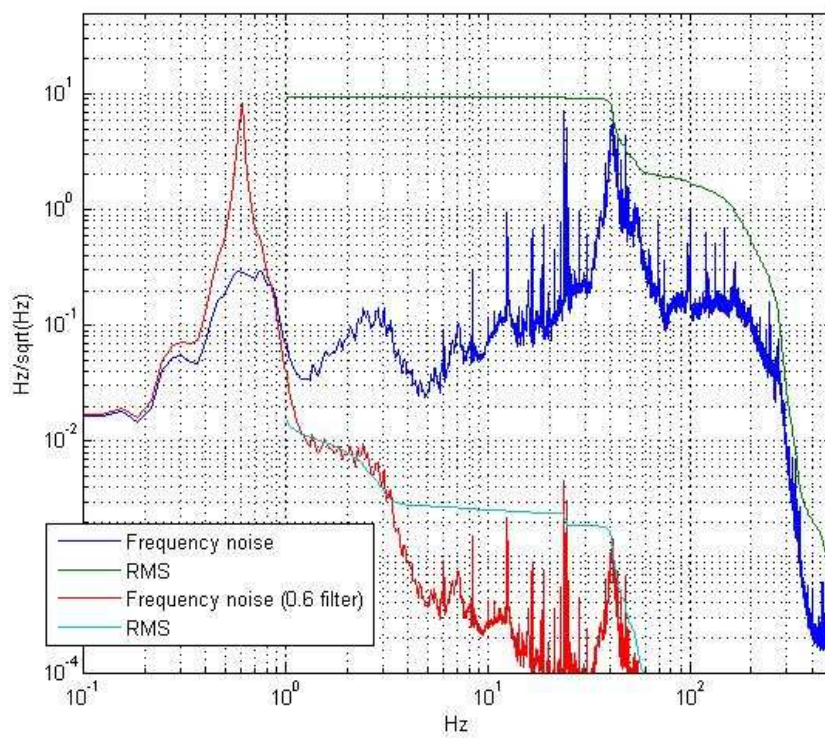
Figure 29: Blue: frequency noise as in fig.13, non suspended cavity; red: frequency noise with the same cavity suspended to a single stage suspension.

The strong peak at 0.6 Hz is the result of the simple application of the pendulum TF to the noise acting on the RFC. In real conditions this peak would be damped by the pendulum damping control. On the other side, the 40 Hz peak is much lower than the 0.01 Hz threshold. These results show two things: first, that a suspended cavity should fulfill the requirements for the pre-stabilization of Virgo, and so far for AdV. Second, that the expected noise, above 1 Hz, is much lower than the effectively measured noise of the suspended RFC in Virgo: if the red curve of Figure 29 is compared with the curve of Figure 23, the red one is in fact much below the measured one above 1 Hz. It's not clear, so far, which is the origin of this apparently excess noise.

5.3. Conclusion

The decision to suspend the RFC from the SIB suspension was taken more than 10 years ago, before any real experience in VIRGO beam stabilization, when the pre-stabilization topology was different from the one actually implemented. The assumptions on the seismic noise were also different from the ones actually measured, and the used mechanical model was very simplified, probably pessimistic. If the same computations as performed in 1993 are performed now in the VIRGO measured environmental conditions, the results could lead to the conclusion that it is not necessary to suspend the RFC. LIGO experience (having similar frequency pre-stabilization requirements) seems to confirm this, and also in Advanced LIGO it is not planned to put the RFC suspended into the interferometer vessel. The suspended RFC solution has been maintained in VIRGO because it was possible without any significant drawback.

On the other hand, in AdV the INJ tower and the SIB will likely accommodate many more large components with respect to the present. The SIB will be crowded and heavy. The possibility to remove some of the components (namely the RFC) from the INJ tower to outside the ITF vessel would largely simplify the optical and mechanical design of the injection system, as well as its alignment and control, thus improving the performance of the system.

Even if the solution to suspend the RFC from the SIB, after the IMC, would be still the preferred option, for this reason the possibility to move the RFC from the SIB to the EIB should be carefully evaluated. FEM simulation of the cavity placed on the EIB leaning on ground, in order to evaluate the real effect of the seismic vibrations, and computation of the other possible noise sources, such as beam jitter, should be performed. The possibility to design a small suspension for the RFC, to be installed on the EIB, should also be evaluated, taking as a reference the already implemented LIGO RFC mount. If the simulation showed that the level of vibration noise would be acceptable, the advantage of having more free space in INJ tower would be significant. Furthermore, the possibility to suspend the whole EIB, on which the RFC would be placed, should also be taken into account.

6. ITF and IMC reflection sensing setup

6.1. The issues

These 2 setups have to be compliant with high power. They need to be equipped with low scattering and high damage threshold optics. A safe setup should be designed in case the high power beam reflected by the IMC or by the interferometer is highly misaligned with respect to the setup. The backscattered light issue should be taken into account. Finally, the setup should provide large dynamic power tuning capability (lambda/2 + polarizers).

The diodes/camera/electronics specifications are not treated in this document.

6.2. Safety precautions

The light reflected by the interferometer and the Input Mode Cleaner can be up to 200 W. So the optics on these paths have to be qualified for high power and low thermal effects. Moreover, the beam reflected by the IMC or by the ITF will potentially reach the external optics in a different position than the one expected (for instance, if the Local Controls of the SIB are opened, the beam reflected by the IMC can reach the EIB with a position different by 10cm with respect to the nominal one). In order not to damage anything on the EIB, there is the need to install a large metallic plate at the input of the EIB with just the necessary holes for the beams reflected by the IMC and by the ITF when they are in the nominal positions.

6.3. Power tuning capability

The system has to be capable of running with low or high power at the input of the IMC/ITF. So the powers in reflection of the IMC and ITF have to be adjustable. We propose putting a half waveplate in these 2 setups followed by a polarizer. The waveplate has to be remotely adjustable to vary the polarization, and so, to change the power transmitted by the polarizer. This setup allows, as well, to set the polarization (S) before all the optics as it could be not in right polarization (as it is the case right now in reflection of the ITF after the Faraday Isolator periscope).

This setup should be followed by a beam-splitter reflecting typically 95% towards the longitudinal sensing diodes, and transmitting 5% towards the angular sensing diodes. The telescopes for adjusting beam sizes and possibly Gouy phases will be located after this beam-splitter.

This order of things is preferred for 2 reasons: it restricts the back-scattered problems to the waveplate and the polarizer (all other optics see less power). And it allows to have independent telescopes for every sensor.

6.4. Backscattered light current status

Currently, there are good models for assessing the scattered light issue but they often don't reflect the overall complexity of the system. But there exist some measurements and noise projections. The current one (done by I. Fiori) can be seen in Figure 30.
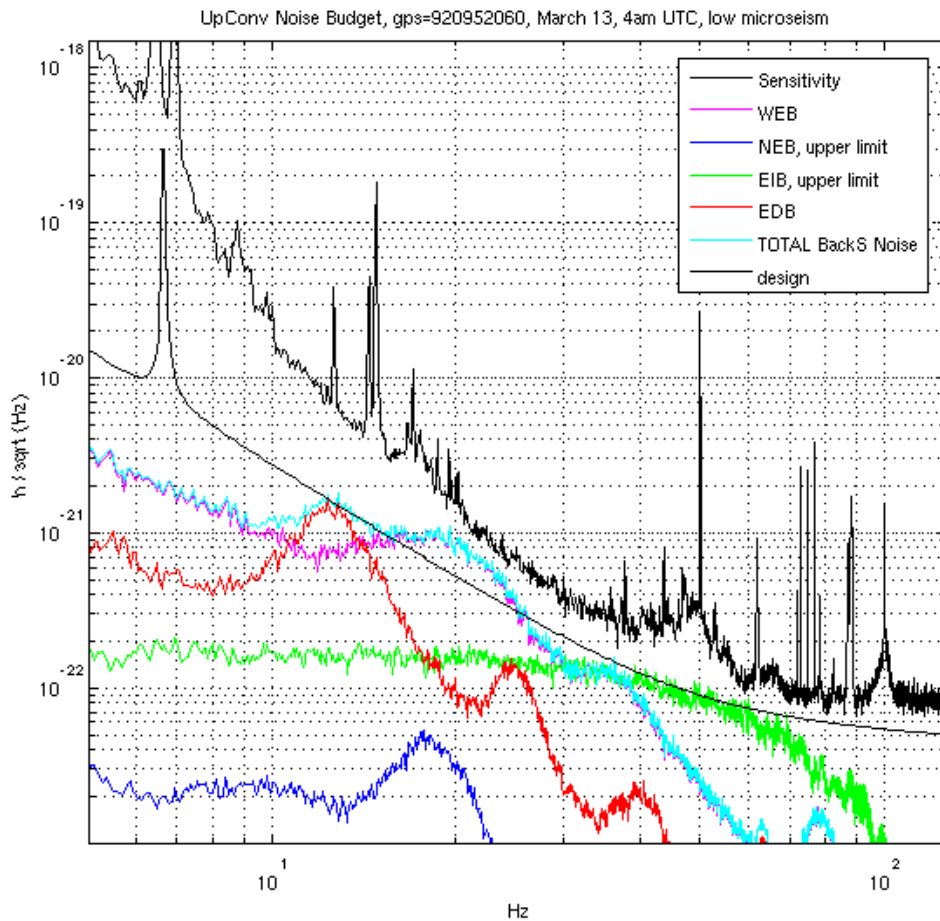
Figure 30: backscattered light noise projection in Virgo current sensitivity.

As it can be seen, the scattering from the EIB is not limiting the current sensitivity but could be critical for AdV. So, special care has to be taken for the critical optical components: wave-plate, polarizer and beam dump. In case, this is not enough, a Faraday isolator could be added.

Right now, it is difficult to derive specifications on the bench motion attenuation to cope with this issue. It is a bit the same for the specifications on the bench motions derived from the input beam jitter requirements. The best effort for the quality of the optics, in particular the beam dump, is recommended. Mechanical solutions to attenuate bench motions are under study in NIKHEF.

Some tests are under progress in the EGO optics lab for designing a beam dump with very low scattering properties and high damage threshold. Currently, we have succeeded in developing a beam dump with damage threshold of around 100W (for a 1mm beam size), and with a total integrated scattered light of around 10ppm (see section 2.2.2 for more details).

7. Faraday isolator

7.1. High power Faraday isolator

Light back reflected by the ITF towards the IMC has already been an issue in Virgo (see section 4.6**Error! Reference source not found.** for more details). This problem will be more significant with the higher power of AdV. The solution for this problem has been the use of an in-vacuum Faraday isolator placed between the IMC and the ITF.

With the higher AdV laser power (180-200 W input power), standard Faraday isolators will exhibit loss of optical isolation, due to thermally induced birefringence, and very high thermal lensing. In order to reach a good level of optical isolation (more than 40 dB) a custom designed Faraday isolator has to be used, including depolarization compensation and a passive correction of its thermal lensing. A design developed during many years of extensive experimentation has already been adopted by LIGO, and should fit also to AdV needs.

The in vacuum Faraday isolator properties necessary for AdV should be to:
- withstand high average power (300 W) over long periods,
- provide enough optical isolation,
- be compensated in terms of depolarization and thermal lensing (residual focal length> 100 m),
- provide good transmission and reflection,
- not to be too big and heavy.

Optical isolation performance, according to LIGO experience (which has been carried out in collaboration with Novgorod IAP group), strongly depends, at laser power level typically exceeding 50 W, on thermal depolarization effects in the TGG crystal. Depolarization has to be ascribed mainly to the temperature dependence of the Verdet constant and to the photoelastic effect [30]. Many years of extensive experience in the Novgorod group [31] have lead to an optical design of a Faraday isolator which compensates thermal depolarization effects. The optical isolation provided by the Faraday isolator prototype should be higher than 40 dB with laser power higher than 250 W (AdV requirement) [17].

The schematic of the candidate Faraday isolator for AdV is described in detail in [31]: it comprises an input polarizer, a half waveplate, two TGG crystals rotating the polarization by 22.5º, separated by a -67.5º polarization rotating Quartz Rotator, and an end polarizer. A difference, with respect to LIGO, could be the use of a larger free aperture TGG crystal: the LIGO isolator has a free aperture of 20 mm. In AdV, if the beam coming out from the IMC will have a diameter of 1 cm, a 25-30 mm aperture Faraday isolator should be more convenient, in order to avoid beam size reduction (in case we use a marginally stable recycling cavity). In the case of the Non-degenerate recycling cavity, a 20 mm clear aperture Faraday should be enough.

The candidate polarizers are Calcite Wedged polarizers (about 4.3º wedge) or Brewster Thin Film polarizers (tests have been done within High power input optics R&D program EOT polarizers are very promising for high power).

A motorized half waveplate is used to compensate for the drop in optical isolation that appears going from air to vacuum (about 10 dB in Initial Virgo). This solution is already used in Virgo+ and its efficiency has been confirmed [32].

Thermal lensing in the in-vacuum Faraday isolator has already been experienced in Virgo. The induced thermal lensing results in a mismatching of the beam with respect of the ITF. The thermally induced focal length in Virgo, with 10 W input power in the Faraday isolator (almost 20 W considering the reflection of

the unlocked ITF) was of the order of 100 m. In this case, the induced mismatching is of the order of 1 %, thus not affecting the ITF performance. Scaling Initial Virgo situation to the AdV higher power (200 W), the computed resulting induced focal length is of about 13 m, thus yielding an unacceptable mismatch of 37 %. Passive compensation will use most likely a DKDP (deuterated potassium dihydrogen phosphate, KD_2PO_4) calibrated rod mounted after the Faraday isolator. The thickness of the rod is critical for exact lensing compensation, the exact dimensions depending on DKPD and TGG parameters. These parameters are not exactly known a priori, this making it difficult to cut exactly the slice with the right length. The effect of the DKDP slice could be changed by changing the crystal temperature: a remote temperature modification should be implemented. The DKDP should be contacted to a heater/cooler (e.g. a Peltier placed below the thermally conductive mount of the DKDP), thus allowing to tune the lens compensation (see section 8.5.2.1 for further explanations).
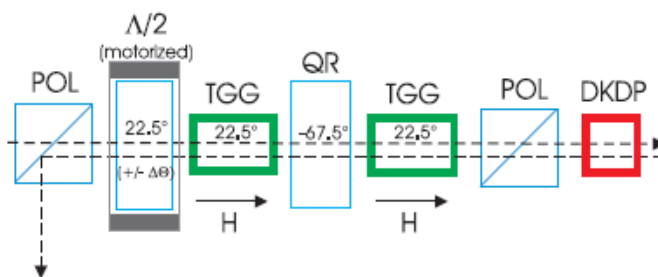

Figure 31: High power UHV compatible Faraday isolator compensated in term of thermal lensing, depolarization and with remotely adjustable isolation.

The dimensions of the Novgorod-IAP Faraday isolator are quite big compared to the initial Virgo Faraday isolator. The weight is about 12 kg. The clear aperture is 20 mm. The possibility to have a larger clear aperture has also been evaluated (25-30 mm). Dimensioning is given in the IAP report [17].

The accommodation of this large device in the input bench vacuum vessel of Virgo could be an issue. A solution will have to be found once the ITF optical configuration has been decided.

7.2. High power isolator tests

In order to perform these tests a high power laser facility was set-up in the EGO optics lab. It relies on a commercial 200W ytterbium laser from IPG photonics (see [33] for more details).

We have focused on the understanding of the thermal effects happening in faraday isolators. When heated up, the thermal effects created in a TGG crystal (magneto-optic material used in faraday isolators) are responsible for thermal lensing, depolarization of the light and modification of the polarization rotation angle. All these effects are spoiling the performance of the isolator and can be different if the isolator is placed in air or in vacuum, since it changes significantly the thermal conditions.

These three effects will be explained and characterized in the following sections.

7.2.1. Thermal lensing effect

7.2.1.1. Thermal lensing effect measurements

To study the thermal lensing effects, we have set up a test bench that can be seen in Figure 32. We use the 200W pump laser to heat up Faraday components located in a test area. The lensing effects are evaluated

looking at the modifications of a low power single mode laser (JDS Uniphase 100mW NPRO laser) used as a probe beam. This laser is sent to the element to be tested in the opposite direction and polarisation of that of the pump beam. The probe laser is then analysed with a Shack-Hartmann wave front analyser.
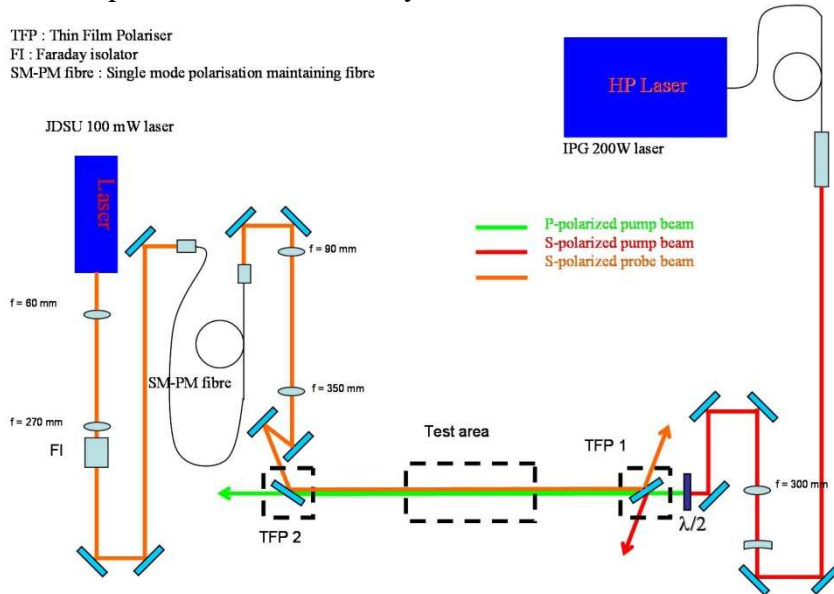
Figure 32: High power input optics test bench scheme.

Figure 33 gives the results of these measurements for a laser power going from 10 to 125 W for two different TGG crystal rods from the same manufacturer (Northrop Grumann). These samples are actually the same kind as those installed in initial Virgo SIB faraday. In order to understand the measured effects, we developed a finite element model analysis code to compute the thermal heating of the TGG samples. Figure 33 also shows the simulated focal length for different values of absorption of the crystal. The simulations are in good agreement with the measurements, with absorption values close to that of the manufacturer (about 1500 ppm).
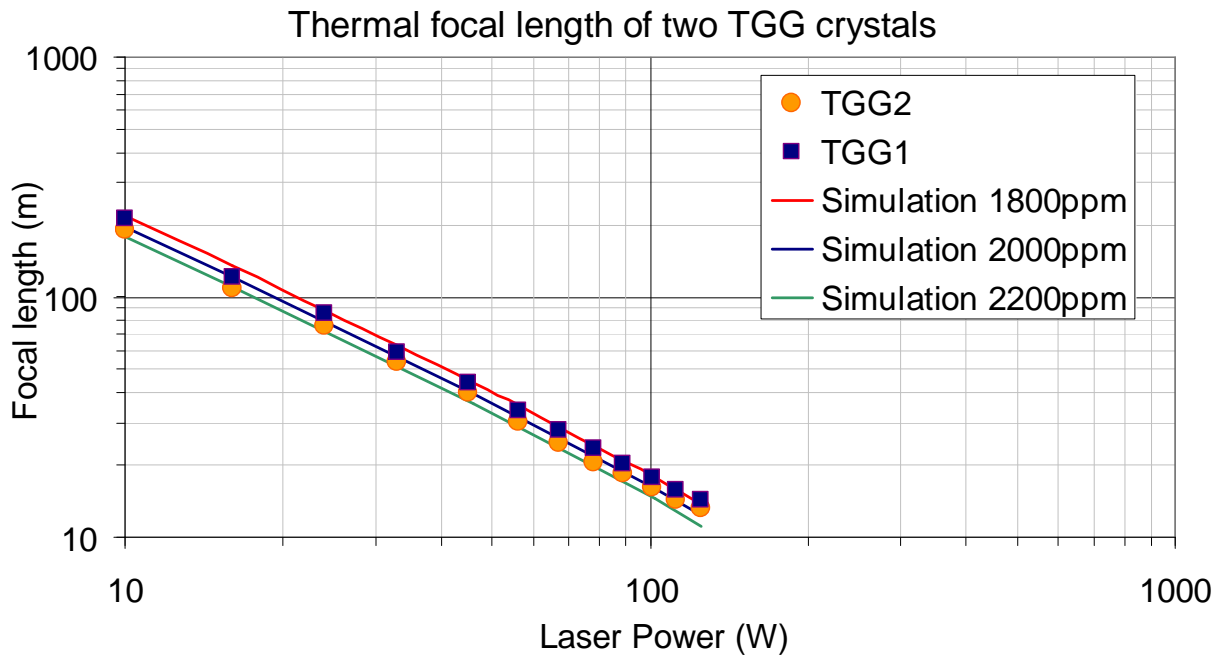
Figure 33: Thermally induced lensing in TGG. Triangles and circles are experimental results. Lines correspond to results obtained with the finite element model code.

All these measurements have been carried out in air. In a vacuum, as only the radiation is cooling down the samples, the heating of the crystal is very different. Nevertheless we could show with the simulation that the thermal lensing is quite similar, due to the fact that this is depending primarily on the radial temperature gradient inside the crystal and not on its average temperature.

7.2.1.2. *Thermal lensing effect compensation*

We can see in these measurements that already at average power, we are experiencing a significant lensing effect (13 m is reached at 125W for TGG crystal 2) in TGG crystals. It is clear that the current design of faraday isolators has to be modified in order to reduce this effect when going to high power. One possibility is to include in the rotator an element realizing a passive compensation of these geometrical distortions. For example it is possible to include a crystal of DKDP which exhibits a large negative thermo-optic coefficient (dn/dT_{DKDP}=-4.4.10^{-5} K^{-1} to compare with dn/dT_{TGG}=1.9.10^{-5} K^{-1}).

With the same setup used for TGG measurement, we tested a few plates of this material provided by different manufacturer. On Figure 34, we can see results of negative thermal lensing created in a 4mm thick plate bought from Leysop Ldt (UK). With our simulation tool, we could derive an absorption of this plate of about 800ppm.

Thermal focal length created by a 4mm DKDP plate
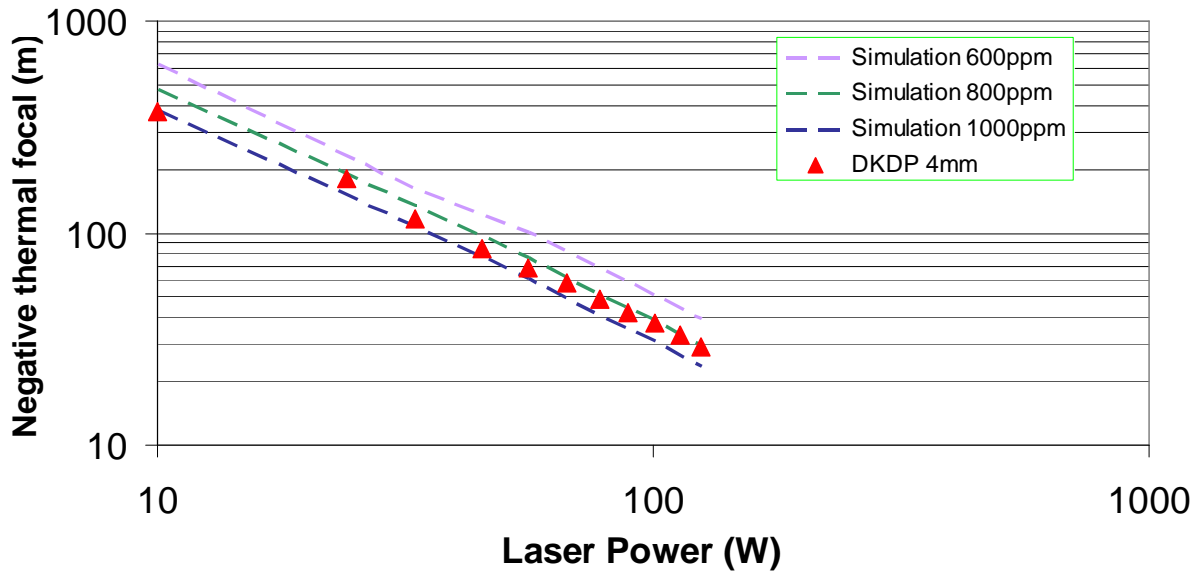
Figure 34: Thermal focal length created by a 4mm DKDP. Simulations agree for an absorption of 800ppm.

Then is is also possible to compute the length of DKDP necessary to correct for the TGG distortions.

As an example, the simulation of the thermal effect in a Faraday of 1800ppm has been performed with a power of 40 W, which corresponds to an induced thermal focal length of about 60 m. We used the finite element model simulation in order to estimate the length of DKDP necessary to compensate for this thermal lensing. In order to optimise the DKDP length we superimposed the absolute phase shift induced by TGG and DKDP and adjusted DKDP length to match the red curve as best as possible. The result is given in Figure 35, we got a good superposition for a 3.4 mm length DKDP rod in this case.
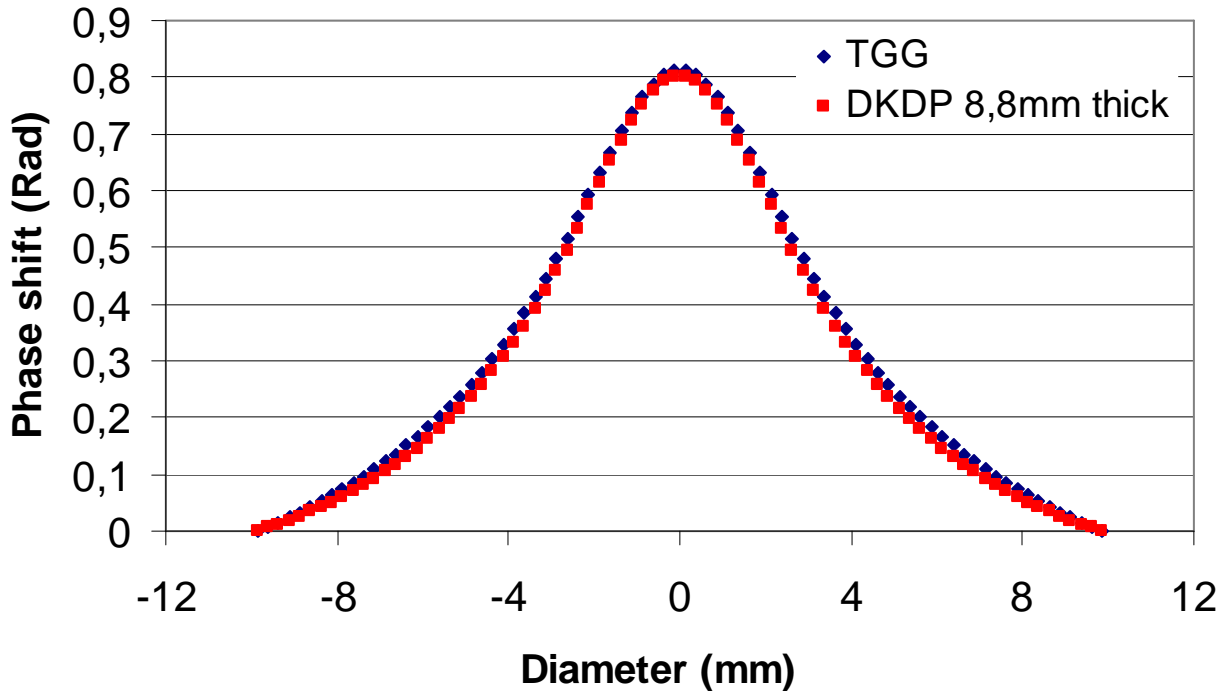
Figure 35: Passive compensation for a Faraday isolator crossed by 40 watt power laser beam (an example).

In order to validate our model, we used experimental data from the Virgo interferometer and experimental measurements [28] that have been performed on the Virgo suspended injection bench Faraday isolator. The investigation into the TGG physical parameters has been done and an absorption coefficient has been evaluated. We got 1600 ppm/cm for the Initial Virgo TGG crystal. Experimental tests are planned in the near future with the 200 W laser as part of the HPIO R&D.

7.2.2. Depolarization effect

The second spurious thermal effect impacting Faraday isolators is the depolarization inside the TGG crystal. This effect was characterized with the 200 W pump laser by placing a TGG crystal between two crossed polarizers. By measuring the small fraction of light transmitted (P_{tran}) by the second polarizer, it is possible to evaluate the depolarization defined by : $\gamma = P_{tran}/P_{Tot}$ for different laser power (P_{Tot}) (cf. Figure 36).
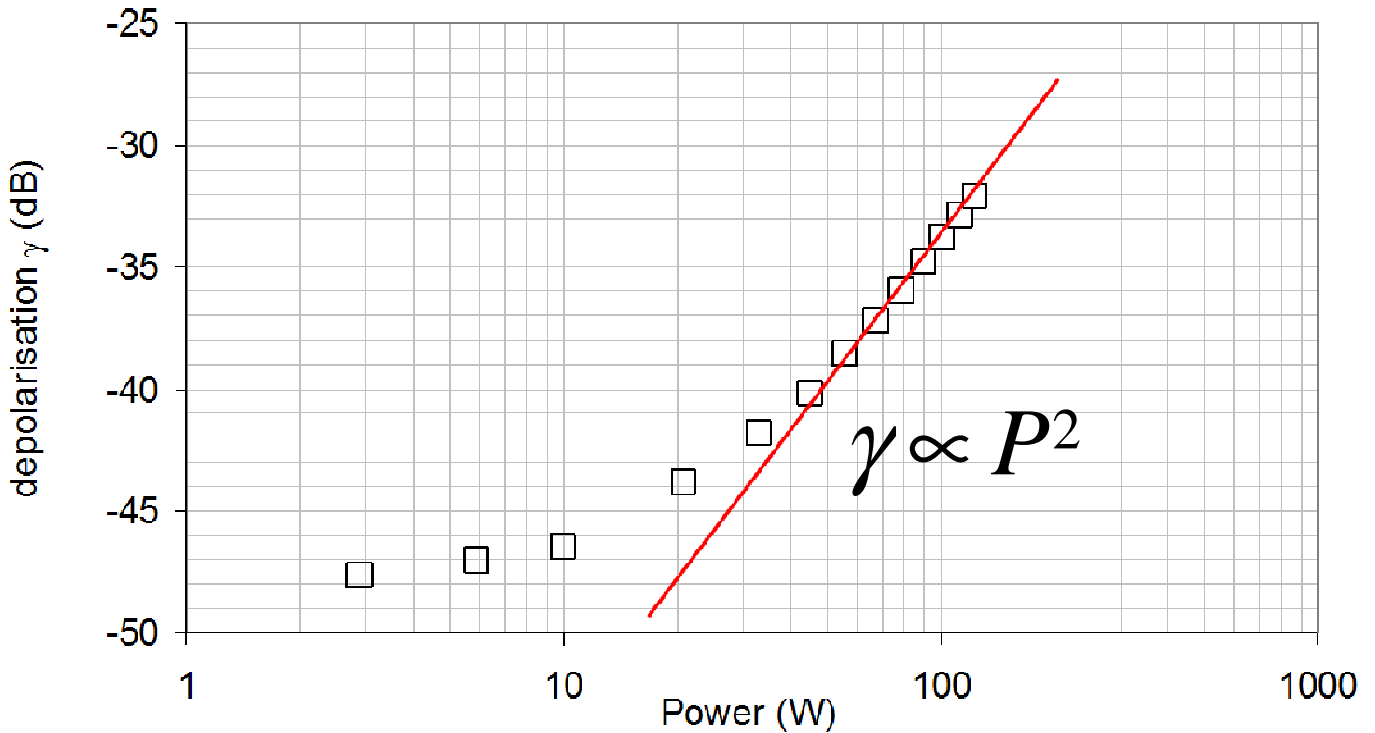
Figure 36: Depolarization (dB) in a TGG crystal as a function of the incident laser power (W).

We can see from these results that for a power higher than about 70 W, γ is proportional to P^2 (see also [31]).

This depolarization inside the TGG crystal cannot be compensated and directly affects the isolation factor of the Faraday. One strategy can be to tune the way the TGG is cut with respect to its crystallographic axes. According to Khazanov [30] this parameter has a large influence on the amount of depolarization. Taking into account this property, it seems more convenient to design faraday isolators with depolarization compensation[30] as described in section 7.1 which, by design, depolarize less and also are less sensitive to TGG crystallographic orientation.

In order to design such an isolator that fulfills AdV requirements, a collaboration has recently started with the Novgorod-IAP. Some results are given in [17].

7.2.3. Verdet constant temperature dependence

The third thermal effect spoiling isolator properties is the modification of the rotation angle of the faraday isolator when the TGG crystal is heated. This is due to the temperature dependence of the Verdet constant V and can be derived from:

$$d\theta = \frac{1}{V}\frac{dV}{dT}\theta \cdot dT \qquad (27)$$

where dT is the temperature change of the Faraday crystal due to laser heating and $\theta = nLVB$ (n is the TGG refractive index, L, the crystal length and B, the magnetic field).

This effect results in the loss of isolation observed when increasing the power inside a Faraday isolator. We could measure this loss of isolation using the 200 W pump laser heating a spare of Initial Virgo Faraday isolator. By retro reflecting a small amount of the power transmitted by the faraday (about 4%), we could measure the isolation, shown in Figure 37, for power going from 2 to 48 W. These tests were done by tuning the isolation at low power (2W) and by measuring the ratio between back transmitted light and total light sent back into the isolator when the power is increased.

As we can see, the isolation change is much different in air and in vacuum, due to the different thermal conditions.

In order to check these measurements, we measured for a power of 37W the temperature change of the crystal and used this value to compute the isolation change using equation 27. We found isolations of about 34 dB and 37 dB in vacuum and in air respectively, which is in good agreement with the measurements.
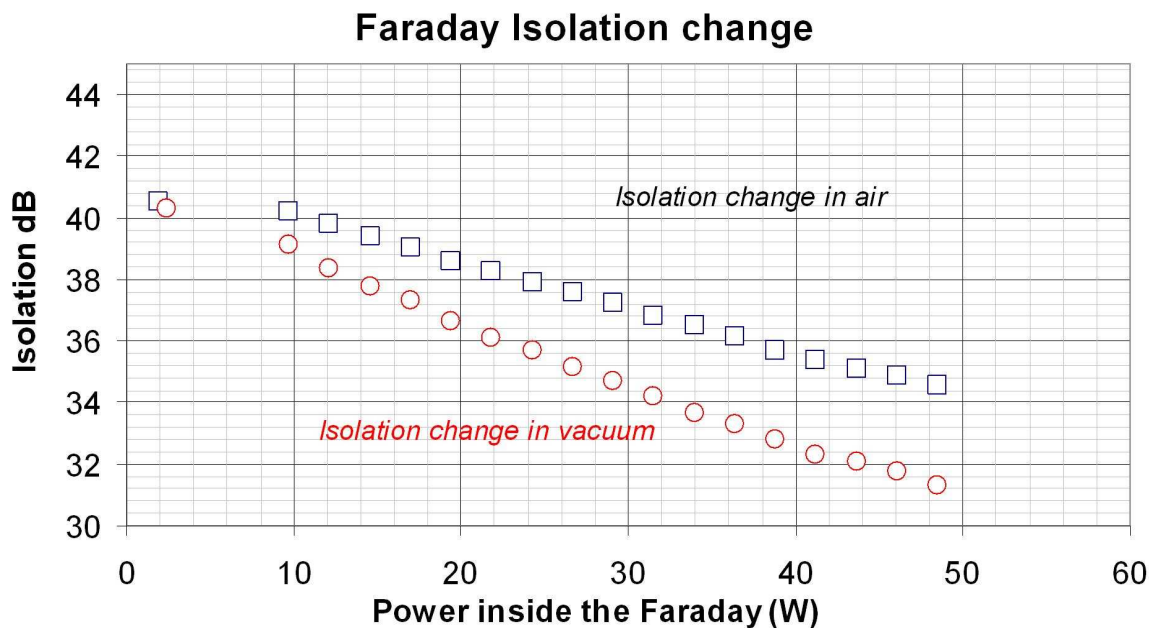
Figure 37: Experimental measurement: Faraday isolation change vs laser pumping power (W). in air (squares), in a vacuum (circles).

In order to compensate for this effect, it is possible to introduce a half wave plate inside the isolator (between the Faraday rotator and a polarizer) to compensate for the rotation change due to the temperature. This solution has been tested under vacuum for a laser power of 38 W. By turning the waveplate by about 0.7°, the isolation can be improved from 32.8 to 36.4 dB. The limit of isolation is then probably due to depolarization inside the TGG.

These measurements, together with the simulation tools that have been developed, permitted the understanding of thermal effects in the Faraday isolators.

The next step will consist of designing and building (during 2009) a prototype that fulfils AdV requirements in collaboration with Novgorod-IAP group.

7.2.4. Prototype design (Institute of Applied Physics, Novgorod, Russia)

The report on the design activity of IAP (which has extensive expertise in the field of high power compliant Faraday isolators) was delivered at the end of March 2009 [17].

The IAP group reports on the design activity that has been carried out in Russia on possible schemes that could be compliant with AdV requirements that have been listed in section 7.1.

Four different kinds of Faraday isolators (FI) have been considered in this study:
- Traditional FI (see Figure 38.a) with and without reinforced magnetic field
- FI with depolarization compensation (see Figure 38.b) with and without reinforced magnetic field.
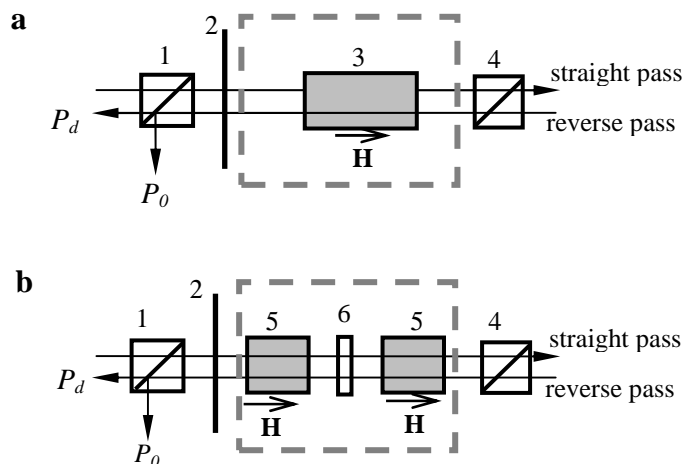
Figure 38: Traditional FI scheme (a) and a scheme of FI with compensation of depolarization (b). 1, 4 – polarizers; 2 – $\lambda/2$-plate, 3 – 45-degree magnetooptical element, 5 – 22.5-degree magnetooptical element, 6 – 67.5-degree reciprocal polarization rotator. Dotted line shows the magnetic system of FI.

Having a reinforced magnetic field enables the reduction in length of the TGG crystal to be used. In this way we can lower the total absorption of the TGG and reduce thermal effects that are appearing in the crystal (thermal lensing, depolarization and verdet constant change with temperature (see previous sections for more information and IAP report [17].

On Figure 39, depolarization in different kinds of Faraday isolators is reported. The best result were achieved with a Faraday isolator compensated for depolarization with a reinforced magnetic field (white circles). In this case the depolarization is lower than 40 dB for 200W meaning that we should be able to fulfil AdV requirements with this kind of isolator choosing the right TGG crystal (good quality).
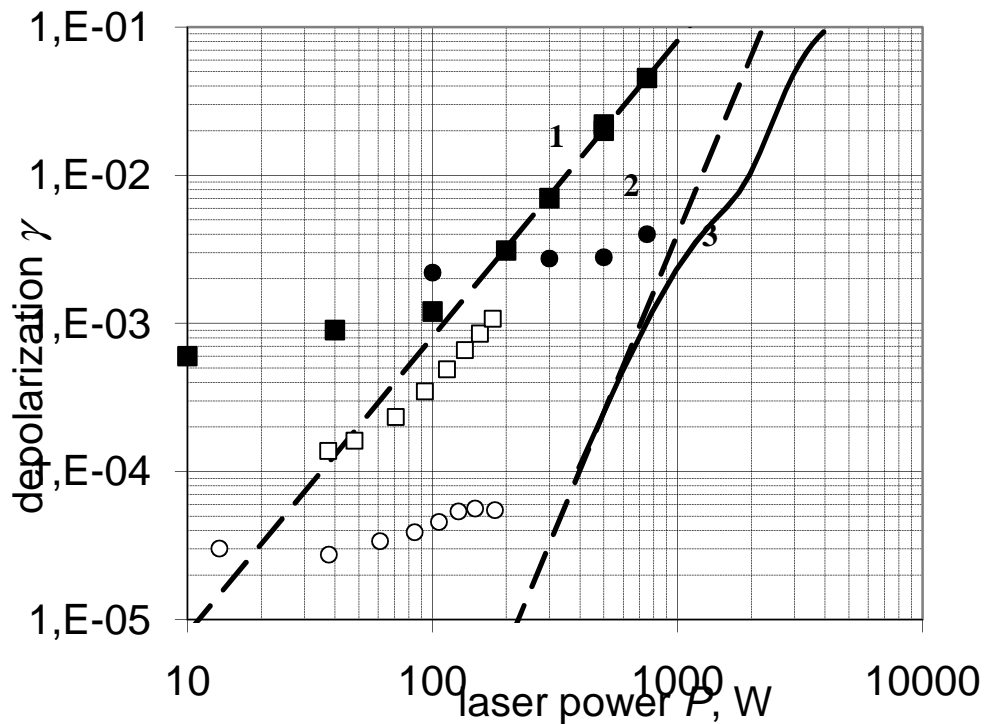
Figure 39: Depolarization versus heating radiation power in traditional FI without compensation (black squares, curve 1) and with compensation (black circles, curve 2, 3) of the depolarization; in FI with reinforced *H* with compensation (white circles) and without compensation (white squares) [4]. Curves 1, 2 were plotted by formulas, 3 – numerical computation result.

On Figure 40, there is a picture of the Faraday rotator that could be used in AdV. It is about 130 mm long and 130 mm diameter and weighs about 12 kg. Possible clear apertures are in the range of 20 mm to 27 mm without change of dimension and weight and for equivalent isolation ratio of the whole device.

Figure 40: Photo of the FI magnetic system in s case

The study showed that it is possible to build a FI that fulfils AdV requirements. The second step consists in building a prototype (HPIO R&D program). The production of the pieces should start once the specifications have been delivered to IAP and the strategy to choose the appropriate TGG crystals have been defined (we have the possibility to buy the crystals in Russia or from Northrop Grumman).

![Advanced Virgo logo]

8. Thermal effects monitoring and compensation

This part deals with the thermal effects that will be present in the AdV INJ and their possible fluctuations depending on the ITF use (commissioning, science mode). After listing the various sources of these thermal effects, we will see that it is necessary to control them. This can be achieved by using different beam monitoring associated with active or passive compensation systems. Various possibilities can be foreseen and will be discussed there.

8.1. Thermal effects in AdV INJ

The experience acquired during Virgo and Virgo+ commissioning showed that the main parts of the injection system subject to thermal effects are the IMC cavity, the suspended bench Faraday isolator and some various elements on the external injection bench. In this part we will give precise numbers concerning the Virgo case and will extend this to AdV.

8.1.1. Thermal effects in the IMC
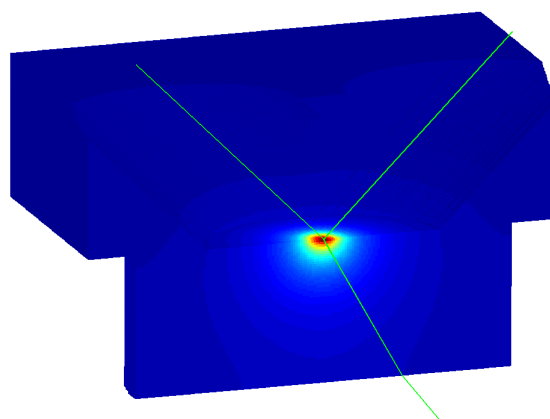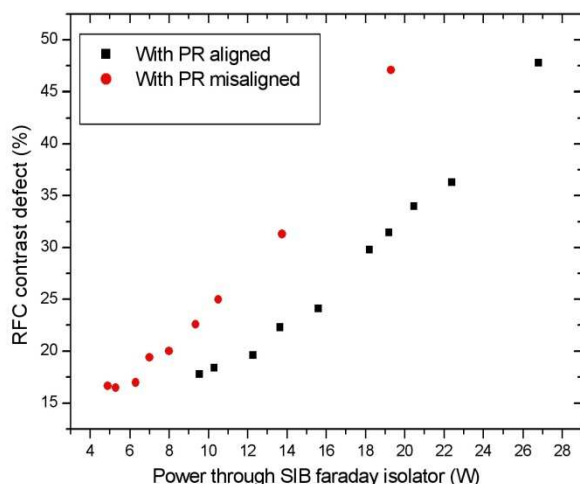
Figure 41: Left :Contrast defect of the RFC for various powers inside the Faraday, with and without PR aligned. The difference between the two curves is a proof of thermal effects inside the IMC. Right : FEM simulation of the heating of one of the flat mirrors of the IMC.

This effect was first noticed by observing the variation of contrast defect of the RFC cavity (located after the IMC) while power is increased. To discriminate between thermal effects inside the IMC and the suspended Faraday, the measure of RFC mismatching was done with and without PR aligned (Figure 41, left). We see here that for the same power inside the Faraday, the contrast is worse when the PR is misaligned. This means that the IMC is suffering from thermal effects.

A FEM model was done to simulate the thermal effects inside the input mirrors starting from their absorption. This simulation enabled to calculate the thermal focal length created and also the astigmatism of the beam which is resulting from the 45 degree incidence on the input mirror (see Figure 41, right). With this code we obtained:

$$F_{Horiz} = 1/0,07 \times P_{abs}$$
$$F_{Vert} = 1/0,046 \times P_{abs}$$

<div align="right">(28)</div>

which means that the output beam of the IMC shows quite an important thermal astigmatism [37].

Using this simulation in combination with contrast defect measurements on the IMC reflection, we could derive a mirror surface absorption of **40 ppm** (for the flat mirrors of the dihedron) [36].

As the beam arrives at 45° incidence with respect to the mirror, the tilt of the output beam of the IMC is also modified when power is increased. As an example, when passing from 11 to 25W of output power we measured 11 μrad of tilt modification.

It is difficult to adapt these measurements to derive the AdV case. Indeed, the absorption of the flat mirror of AdV IMC should be close to the actual Virgo ones before their installation (which was 2 ppm). As we see, some aging or pollution effect may have deteriorated these values and this seems difficult to predict in advance. In any case, we can estimate that with 180 W of incoming power on the IMC, the thermal focal length would go from 250m to 6m for absorptions from 1 ppm to 40 ppm.

8.1.2. Thermal effects in the suspended bench Faraday Isolator

When heated up, the thermal effects created in TGG crystal used in isolators are responsible for thermal lensing, modification of the polarisation rotation and depolarization. All these effects are degrading the performance of the isolator. In this part we will only treat the problem of thermal lensing.
The measurements done as part of the R&D program "High power input optics for AdV" showed TGG absorptions of about 1600ppm/cm [34]. These values were cross checked directly on the ITF by measuring the mismatching on the 3km FP cavities when the input power is increased [35].

As an example, for 40W of power inside the Faraday (which corresponds to the maximum input port power for Virgo+) the measurements done in laboratory showed a focal length of 70m due to thermal lensing created by the Faraday itself. As we said, this lensing creates mismatching on the FP cavities. On Figure 42, we can see simulations realized with Finesse and Zemax that computes this mismatching as a function of the lensing created inside the Faraday. We can then conclude that at 40W, the mismatching induced is of the order of 5%.

We see from this simulation that it is mandatory to keep thermal lensing in the Faraday quite small (even if it can be partially compensated by the ITF mode matching telescope). Up to 50m of focal length seems a reasonable value at full power for Virgo.

For AdV, this sensitivity will be different due to the different optical configuration . What we can say is that taking into account a power of up to 250W inside the Faraday, a compensation of this effect should be foreseen (see section 7.2.1.2).
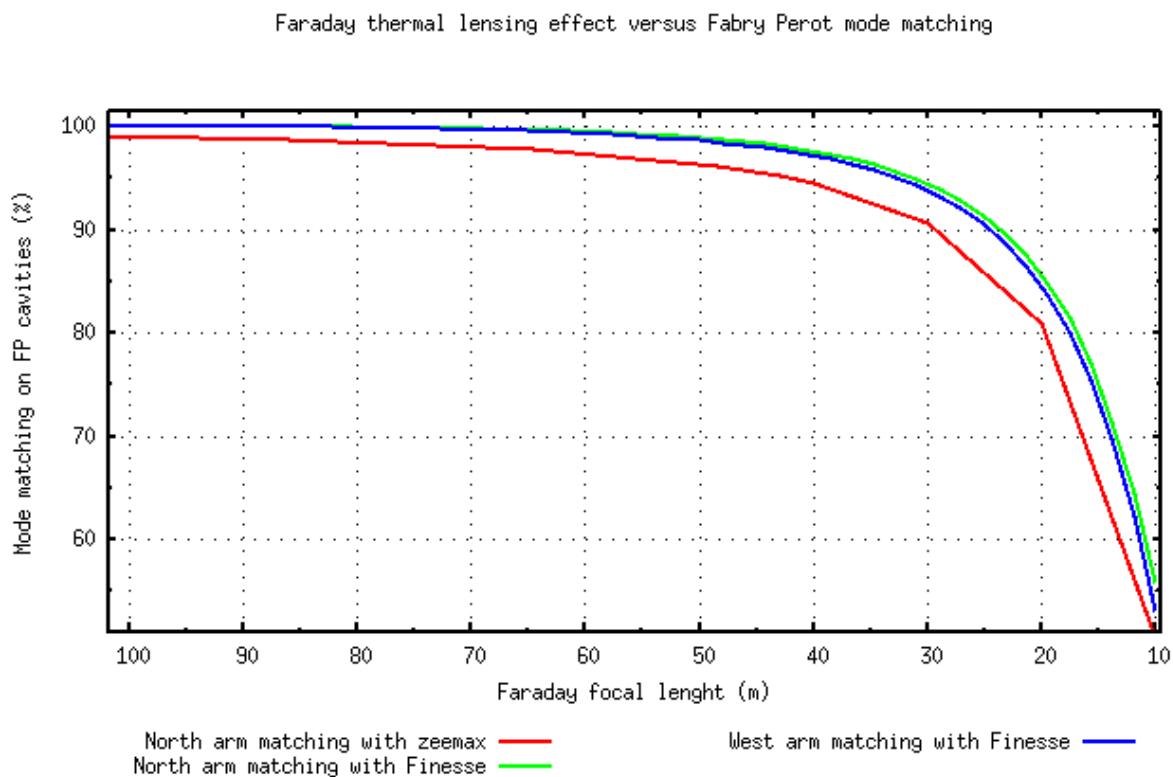
Figure 42: Mode matching on the 3km Virgo FP cavities as a function of the thermal focal length created inside the Virgo SIB Faraday Isolator.

The Faraday Isolator developed by the Novgorod Institute of Applied Physics for AdV should provide such a compensation (see section 7.2.1.2) and therefore, the residual focal length should be much smaller than that of Virgo+.

8.1.3. Thermal effects on the External Injection Bench

A few optical elements on the external bench could also suffer from thermal effects:

• Commercial Faraday isolator on the EIB: such an element should be used before the laser system to further improve the isolation of light coming back from the ITF. Measurements made during Virgo+ commissioning showed a thermally induced focal length of up to 2 meters [38] at full power .

• Commercial polarizers. It was shown in the frame of the R&D program "High power input optics for AdV" that much care should be given to their selection. The different polarizers of the actual Virgo injection system were tested and showed thermal focal lengths from 2m to negligible for a power of 100W and a beam waist of 1mm. It was possible to identify suitable polarizers for AdV taking into account both EIB and SIB constraints with negligible thermal effects.

• EOM (see section 1): The remaining lensing after selection should be negligible at full power.

As we see, we will be able to select suitable elements on the EIB to get small residual thermal effects. In the case of the Faraday, it should be placed before the IMC mode matching telescope where its lensing may be compensated. Moreover, it should be noted that all these elements will be placed before the EIB IPC which will keep the effects constant when changing the IMC input power.

In this part, we listed all the elements that could suffer from thermal effects in the AdV INJ. We could see that even if much care will be given to the selection and design of these different elements, the residual effects are not necessarily negligible. This justifies the development of a monitoring and control system.

8.2. Impact of the INJ thermal effects depending on ITF use

In this section, we study the impact of the previously listed effects on the functioning of the ITF in both science and commissioning modes to point out needs in terms of compensation and monitoring of these effects.

Science mode:

In this mode the power should remain constant on EIB-IMC-SIB. The power that should be sent to the ITF can be adjusted using the 2nd IPC system (see section 2.3). This enables to keep thermal effects constant in the injection. Nevertheless, it can be interesting to monitor the beam sent to the ITF.

A few transients can still modify the beam characteristics in case of:

- Lock-unlock of the IMC: this creates a transient on IMC matching, a transient on the beam coming out of the IMC and a transient at the output of the Faraday.
- Lock-unlock of the ITF: while the PR is aligned during the lock acquisition the power inside the faraday on the SIB changes (about 25% in the Virgo case).
- Lock-unlock PMC: transient on the IMC matching, IMC output, SIB Faraday output.

We see here, that even in the case of science mode, some time dependent thermal effects can impact the functioning of the interferometer. It would be therefore very convenient to get a way to monitor them. In addition, some passive (or active compensation) could help reduce transients and therefore help ITF locking.

Commissioning mode:

In this mode, we have all scenarios of science mode. In addition, it will be also needed to change power inside the first IPC on the EIB in order to study thermal effects in the IMC. This changes thermal effects in the IMC and the Faraday. Therefore, it seems very practical to get a second monitor of the beam after the IMC.

In commissioning mode, it would also be interesting to work in the following configuration: IMC locked at low power-ITF locked at low power. This means that we have to keep absolute thermal effects in the IMC, IMC output and Faraday limited (because in this case the amplitude of the effects would prevent a full compensation by simply adjusting the benche's telescopes).

As a whole, we think that taking into account the magnitude and the numerous thermal effects that could impact the INJ, we strongly recommend to develop a way to monitor these effects (exact place to be discussed further) and a way to compensate them. This compensation is not totally mandatory in science mode as the IPC can be used to keep the injection always in the same thermal conditions. It is nevertheless highly recommended for convenience in commissioning mode and would also help to reduce transients in both modes.

8.3. Beam Monitoring

A beam monitoring system is an essential part of INJ. It will allow to assess the quality of the beam at all stages of the injection and to monitor thermal transients providing the necessary error signals for any active compensation.

8.3.1. Beam Parameters to measure

The main aberrations that are caused by thermal effects in AdV INJ are tilt, focus and astigmatism. In addition to measuring aberrations due to thermal effects it will be important to measure also higher order modes, as it is the global quality of the beam that defines the efficiency with which it is coupled into the IMC and FP cavities. Therefore, in order to have a comprehensive understanding of the system and the necessary error signals to compensate, it is necessary to have a complete picture of the amplitude and phase of the beam.

An additional complication is the fact that the beam contains several different fields, namely the carrier, the upper sidebands and lower sidebands. These three fields could be modified differently. This could be the case at the level of the EOM where the modulation is made. Otherwise this may occur for each cavity; the IMC and of course the ITF itself. There is therefore a need to measure the amplitude and phase of these fields individually.

8.3.2. Location of beam monitoring devices

In order to decouple the various different effects previously described in chapter 8.1, it will be necessary to place beam monitors at various stages of INJ. There are four points in the injection system where monitoring would be useful:

- **Output of the EIB**. This will allow the monitoring of thermal effects present on the External injection bench. This will be of particular use during commissioning showing the quality of the beam entering the IMC and giving an error signal for adjustments on the EIB. The beam could be picked off after the first polarizer of the EIB IPC (see figure 8).
- **Transmission of the IMC**. This will allow the direct monitoring of thermal effects induced by the IMC. It will be necessary to pick off a beam and send it to the EIB.
- **Input of the ITF**. The quality of the carrier and sidebands defines how well they will be coupled into the FP cavities and recycling cavity respectively. Therefore it is important to measure their properties individually at the input of the ITF. Comparing the measurement here with that in transmission of the IMC will give information about the thermal effects in the Faraday. The beam

could be picked off after the first polarizer of the SIB IPC (see figure 8) and then sent to the EIB for measurement.

- **Reflection of the ITF**. Measurement of the carrier, upper and lower sideband beams in reflection of the ITF will give a wealth of information concerning the alignment and thermal effects in the ITF.

Individual monitoring for each of these places in INJ could prove to be expensive and cumbersome. A possible solution would be to have just one of each monitoring device and to switch between the different beams when the need arises. Figure 43 shows an example of this setup that would be placed on the EIB.
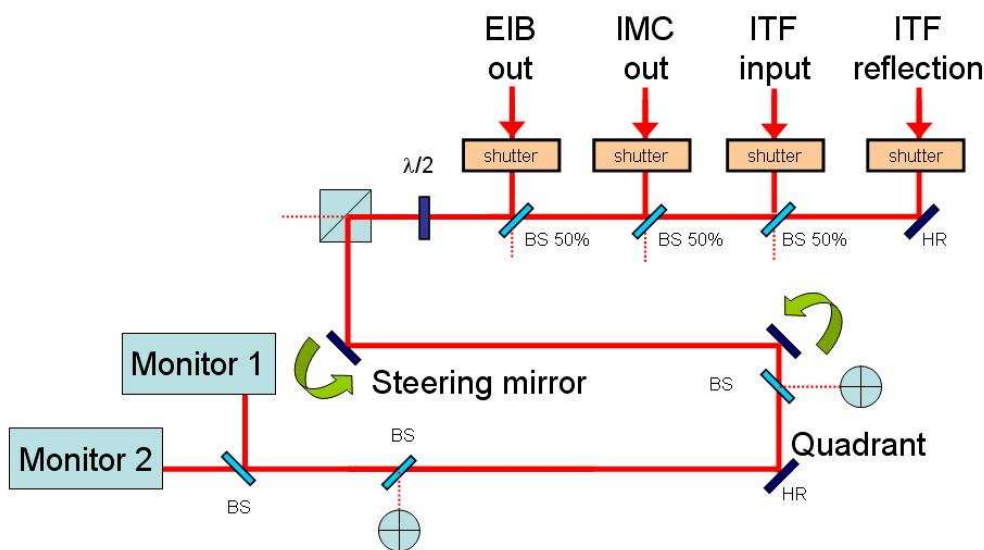

Figure 43: Setup of the proposed beam monitoring system. The four beams to analyze are combined using beam splitters. A combination of controllable mirrors and quadrants enables to preserve alignment on monitor systems.

The four beams are combined with beam splitters. Then a set of shutters is used to select a single one that is adjusted for tilt and translation using motorized mirrors and reference quadrants. This beam is sent to the beam monitoring system which could be one or more devices.

Of course this proposed setup is suitable for monitoring applications, however if the monitoring is used in a closed-loop compensation then a dedicated monitor may be required.

8.3.3. Existing beam monitoring systems in Initial Virgo

The available beam monitoring systems in the injection system of Virgo+ are relatively basic. Tilt and translation of the beam at the output of the external injection bench and suspended injection bench are efficiently characterized using near field and far field quadrant diodes as this is vital for aligning the beams with respect to the IMC cavity and ITF. However higher order aberrations are only indirectly estimated by looking at the camera images in transmission and reflection of the IMC and RFC cavities and by measuring mode matching efficiency. The only tool for measuring the carrier, upper and lower sideband independently is the Scanning Fabry-Perot which measures the relative integrated intensity of each. In order to better understand and control thermal effects in AdV there is clearly a need to find new beam monitoring solutions.

8.4. Beam monitoring solutions

There are a large number of techniques available for measuring the amplitude and phase properties of a beam. This section will briefly describe them.

8.4.1. Interferometers

8.4.1.1. Homodyne Interferometer

This technique interferes the beam to be measured with a reference beam of the same frequency on a photodetector. The measured intensity will be related to the phase shift between the two beams. As this is a DC detection then a CCD detector array may be used to measure the interference over the whole beam. Typically to reconstruct the phase and amplitude of the beam three images are required where the phase between reference and signal is changed by 90 degrees. A commercial device is sold by ESDI [39] giving the following specifications:

   Image Resolution 768 x 576
   Relative wavefront measurement accuracy: $\lambda/1000$
   Frame rate: 30 Hz

8.4.1.2. Heterodyne Interferometer – "Phase Camera"

This technique interferes the beam to be measured with a reference beam that has been shifted in optical frequency. The resulting beat frequency between the two beams is demodulated yielding directly the phase and amplitude information of the beam being measured. This technique is of particular interest for gravitational wave detectors as it allows the measurement of amplitude and phase of the carrier and each sideband independently. The phase camera was recently installed for Virgo+ on the external detection bench [40] with the goal of measuring the effect of input mirror heating on the sidebands. Figure 44 shows a schematic setup of the phase camera.
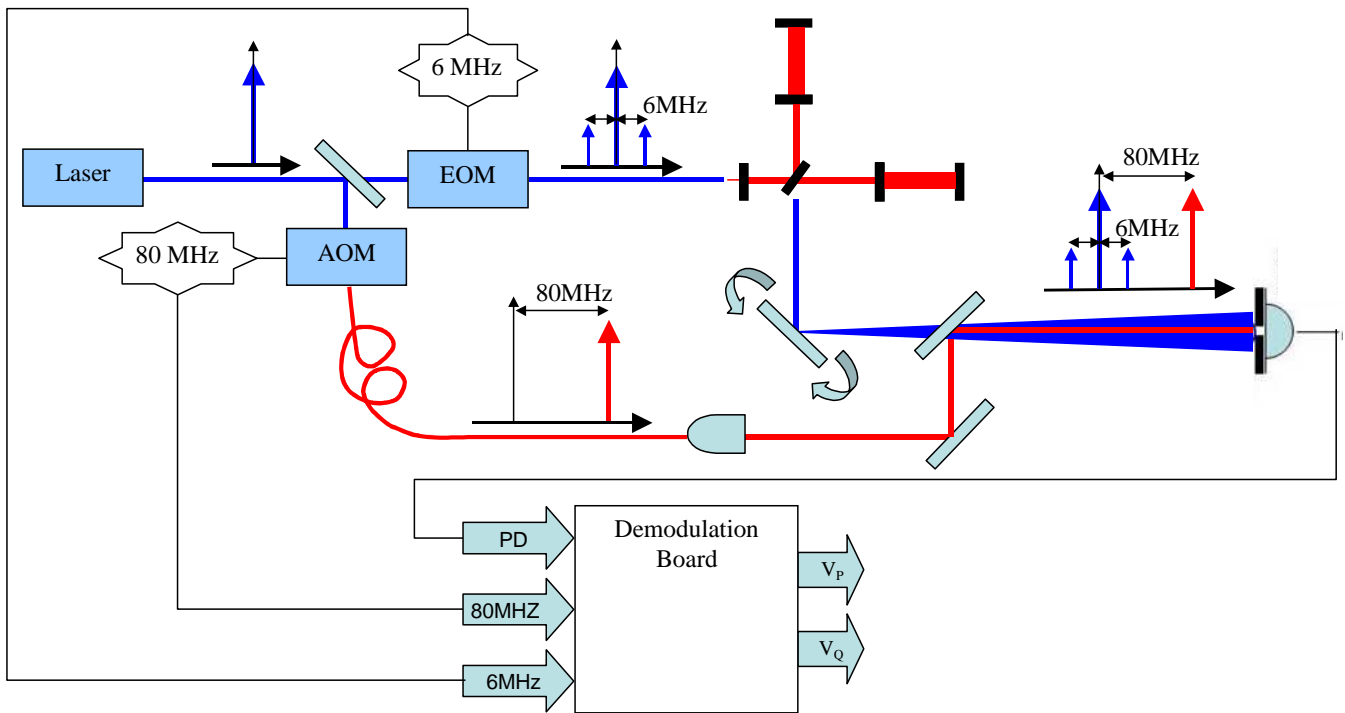
Figure 44 : Schematic setup of the phase camera installed on Virgo.

The beam to be measured, containing the carrier and two sidebands at ±6MHz is scanned over a pinhole detector using a mirror mounted on a 2-axis piezo-electric actuator. At the detector the beam is mixed with a reference beam which has been sampled from the injection bench before the 6MHz phase modulation and then shifted in optical frequency by 80MHz using an acousto-optic modulator. The mixing results in beat frequencies of 74, 80 and 86MHz corresponding respectively to the lower sideband, carrier and upper sideband. Each of these signals is demodulated yielding a signal in phase V_P and a signal in quadrature V_Q. From these signals the amplitude E and phase ϕ of the three fields may be directly calculated by

$$E=\sqrt{V_P{}^2+V_Q{}^2} \quad \text{and} \quad \phi=\arctan\left(\frac{V_Q}{V_P}\right) \tag{29}$$

The phase camera is a valuable tool for understanding thermal effects in the interferometer. Figure 45 shows the field amplitude distribution for the carrier and two sidebands when the interferometer is locked at step 12.

65
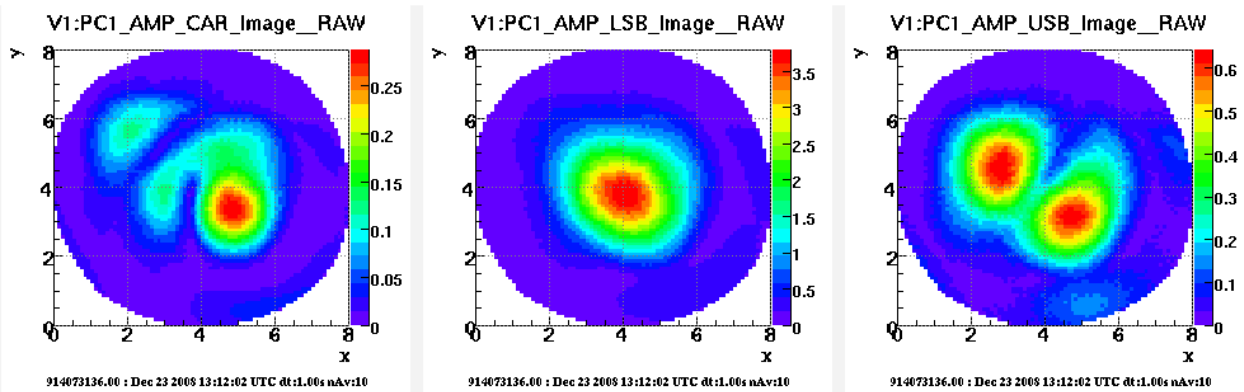
Figure 45: Amplitude images for carrier (left), lower sideband (middle) and upper sideband (right) at the output of the hot interferometer.

We see clearly how thermal effects in the interferometer can affect the overlapping of the three fields. In addition the phase camera may be used to measure distortions of the wavefront due to thermal effects by looking at the phase image. Figure 46 shows the amplitude and phase Image of the carrier field in reflection of the input mirror while it is being heated at the center with a CO2 beam of 144mW.
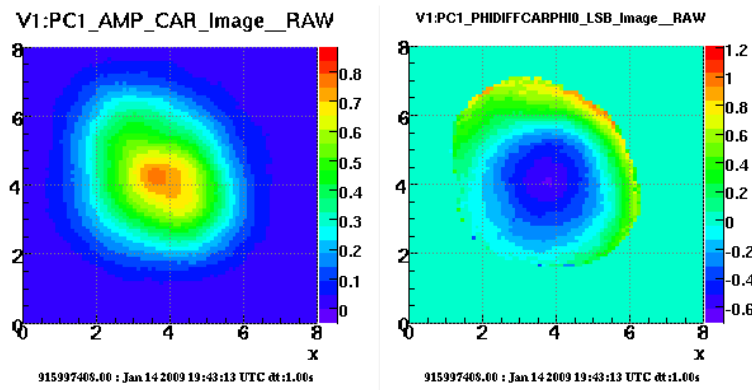

Figure 46: Amplitude (left) and phase (right) Image of carrier in reflection of input mirror being heated by the CO2 central spot. Color scale for phase in radians.

We see clearly the distortion at the center of the wavefront due to the thermal modification of the optical path length in the mirror substrate. The relative wavefront measurement accuracy was determined to be $\lambda/300$. This accuracy is mainly limited by the stability of the optical setup and with optimization could be improved to about $\lambda/1000$.

The main disadvantage of the phase camera is the need to scan the beam to be measured. Scanning can generate unwanted vibrations, introduce noise into the measurement and limits the frame acquisition rate to about 1Hz. The logical solution would be to use an array of detectors instead of just one. However each individual pixel will require frequency demodulation which could result in complicated and expensive electronics development. Fortunately much work has been done in the field of sensor arrays for the application of time-of-flight range finding [41]. These devices demodulate an RF optical signal reflected off a target. The phase measurement is proportional to the target distance. Application of this type of device could give wavefront measurement accuracies of up to $\lambda/1000$ with a frame rate of around 50Hz.

8.4.2. Wavefront sensors

The term wavefront sensor is normally applied to instruments used for measuring the aberrations of an optical wavefront that do not require an unaberrated reference beam to interfere with, such is the case for interferometry. Consequently they can also measure noncoherent sources and are commonly used in adaptive optics systems, lens testing and increasingly in ophthalmology. They are also becoming increasingly popular for measuring the characteristics of laser beams. One of the main advantages of wavefront sensors is that they measure locally the tilt or curvature of the wavefront rather than the absolute phase. This makes them much more insensitive to vibration. Here we will list the different available techniques.

8.4.2.1. Shack-Hartmann sensor

A schematic diagram for the Shack-Hartmann wavefront sensor is shown in Figure 47.
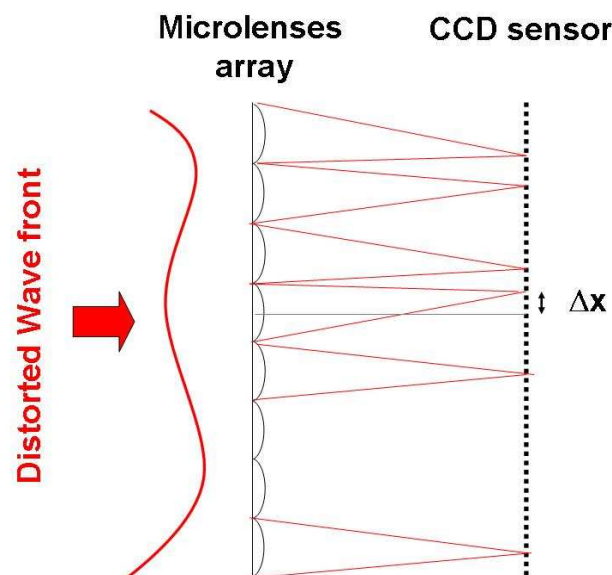
Figure 47: Principle of operation of a Shack Hartmann wave front sensor. The local wave-vector direction is measured by the displacement of the focal spot of each micro lens.

It consists of an array of lenses of the same focal length. Each is focused onto a sensor array such as a CCD. The local tilt of the wavefront across each lens can then be calculated from the position of the focal spot on the sensor. Any phase aberration can be approximated to a set of discrete tilts. By sampling an array of lenslets all of these tilts can be measured and the whole wavefront approximated. There is a large number of companies selling this type of device namely: Imagine Optic, Wavefront Science, OKO, Metrolux, Optocraft and Thorlabs. All of these companies give very similar specifications:

Detector size: ~ 6.1x4.9 mm
Number of lenslets: ~ 40x32
Relative wavefront measurement accuracy: ~ $\lambda/150$
Focus measurement accuracy ~ 10^{-3} m^{-1} (i.e. 10% accuracy on 100m of focal length measured)
Frame rate: ~ 20 Hz

The accuracy is a little lower than that of the interferometer techniques. However we note that the device is much simpler and is easily calibrated to give absolute measurements. Furthermore the accuracy is more than satisfactory to measure changes in focal length of less than 100m that have been predicted for the INJ. In addition software is available with such a device in order to break down the aberrated wavefront into its Zernike polynomials and use this information in a closed-loop compensation system.

A Shack-Hartmann from Imagine Optic is currently for the R&D "High Power Input Optics" in order to characterize the thermal effects due to absorption, in optics to be used for AdV (see Figure 48).
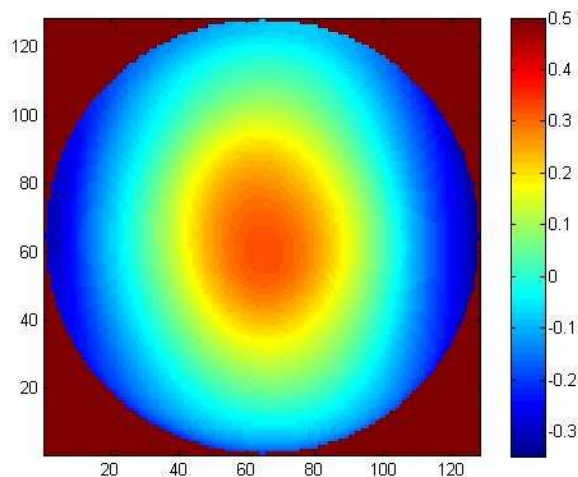

Figure 48: Image of the wavefront distortion through a polarizer when transmitting 100W beam at 1064nm with a waist of 1mm. Color scale in waves.

8.4.2.2. Hartmann sensor

The Hartmann sensor works on the same principle as the Shack-Hartmann. Instead of an array of lenslets a plate is used with an array of small holes. The position of the light spots on the CCD behind the plate is measured to determine the local wavefront tilt. The intrinsic design of the Hartmann sensor makes it less efficient at light gathering than the Shack-Hartmann. However this is not a problem for our application. Aidan Brooks developed a Hartmann sensor for measuring thermal distortions in the mirrors of gravitational wave interferometers to be used in a closed-loop compensation [42], claiming an accuracy of $\lambda/1050$. The combination of simplicity, high accuracy and potentially low cost makes the Hartmann sensor an appealing option.

8.4.2.3. Curvature sensor

This device is similar to the Shack-Hartmann but instead of measuring the position of the spots, the curvature sensor measures the intensity on either side of the focal plane. If a wavefront has a phase curvature, it will alter the position of the focal spot along the axis of the beam, thus by measuring the relative intensities in two places the curvature can be deduced. No commercial devices appear to exist using this technique.

8.4.2.4. Multiwave Lateral Shearing interferometer

In this technique, a 2D diffraction grating splits the incident beam into four identical waves, which propagate along slightly different directions. An interference pattern is generated a short distance behind the grating. Where aberrations are present in the beam the interference grid is distorted. The grid deformations directly relate to the gradient of the phase at each point of the optical beam. This technique allows a much higher lateral resolution compared to the Hartmann or Shack-Hartmann technique. The technique has been commercialized by Phasics who offer the following specifications

    Detector size: ~ 4.8 x 3.6mm
    Image Resolution 160x120
    Relative wavefront measurement accuracy: ~ $\lambda/350$
    Frame rate: ~ 10 Hz

8.4.3. Conclusion

The best monitoring system is one which gives the amplitude and phase distribution for the carrier and sidebands individually. The only device that is capable of offering all of this information is the phase camera. This type of solution has already been developed within the collaboration and is now up and running in Virgo+. **It therefore appears necessary to include the phase camera in INJ**.

Although commercial wavefront sensors cannot separate the three fields, in most situations of thermal effect characterization and monitoring this is not necessary. These wavefront sensors are simple, have adequate accuracy, they are silent, insensitive to vibration and give absolute measurements. The wavefront sensors that we have looked at all have similar specifications. However **the Shack-Hartmann sensor is by far the most mature and versatile device for which we have hands-on experience**.

The phase camera and Shack-Hartmann wavefront sensor is an ideal combination for measuring all aspects of beam quality and thermal effects in the AdV INJ.

8.5.   Thermal Compensation

In Chapter 8.1 we saw that thermal effects in the injection system for AdV are sufficiently large to cause problems with the normal functioning of the interferometer both during commissioning and science runs. The problem is partially alleviated by the use of a two stage input power control system that allows the changing of output power while keeping thermal effects in critical components constant.

Nevertheless a compensation system will be inevitable to allow for a versatile use of the instrument and to adapt to changing conditions over time. In this chapter we will highlight areas where compensation could be necessary and discuss the possible solutions.

8.5.1. Location of compensation system and corrections to apply

In this section we will discuss the compensation needs for different points in INJ.

1. **Output of the EIB**. We have seen that there will be important thermal effects modifying the characteristics at the output of the EIB. However the first stage IPC will insure that these effects remain constant. Therefore it would seem that manual intervention on the bench to compensate for these effects would be sufficient.

2. **Transmission of the IMC**. The magnitude of the thermal effects in the IMC is difficult to predict and could change over time. In addition during commissioning it will be necessary to work with different powers in the IMC. It is therefore essential to have an adaptive compensation of these effects which are principally focus and astigmatism. The tilt can be compensated using other actuators already present in the system.

3. **Output of the SIB Faraday**. The thermal effects are very strong in the Faraday of the SIB although they will be easier to predict and more stable over time than the IMC. A thermal compensation principally in focus will be essential for working at different powers in the IMC and particularly to compensate for the thermal transients when the PR cavity is locked.

8.5.2. Compensation solutions

The most obvious way to correct for thermal effects would be to tune an adjustable telescope as it is done currently for Vigo. But this method has numerous drawbacks as it modifies both the waist size and its position. It also has a limited correction range and does not enable to correct any aberrations other than focusing. It is also adapted only for DC correction and requires a separate tuning for each power. For AdV this solution has to be kept, as it can still permit some fine-tuning. Nevertheless it is mandatory to find other systems. Here we will list the most relevant making reference to how they may be applied to our particular problems.

8.5.2.1.   Compensation plate

The optical path length through a substrate depends on its temperature. This is of course the origin of the thermal lensing effect. A compensation plate is an optical element added to the system which will have a temperature distribution such as to cancel out the aberrations caused by the thermal effects of the IMC and Faraday.

The dependence of the optical path length on temperature, χ, is given by

$$\chi = \frac{dn}{dT} + \alpha(1+\sigma)(n-1)$$

(30)

where dn/dT is the refractive index temperature coefficient, α is the thermal expansion coefficient, σ is the Poisson ratio and n is the refractive index. Table 3 shows that these parameters will change dramatically according to the substrate used. Therefore selection of the right substrate for the job is paramount.

Parameter	Fused silica	TGG	DKDP	SF57	BK-7
n	1.45	1.94	1.49	1.81	1.5
dn/dT (10^{-6} K^{-1})	8.7	19	-48	6.8	1.5
Thermal conductivity (W m^{-1} K^{-1})	1.37	7.4	2.1	0.62	1.11
α (10^{-6} K^{-1})	0.55	9.4	44	9.2	8.3
Absorption Coefficient (ppm cm^{-1})	0.7	1500	~1200	200	1000
σ	0.17	?	0.119	0.248	0.206
χ (10^{-6} K^{-1})	8.99	27	-23.9	16.1	6.5

Table 3: typical values for commonly used substrates

8.5.2.1.1. *Passive compensation*

The absorption of transmitted light in most substrates generates a positive lens due to χ being positive. The insertion of a compensation plate made of a substrate such as DKDP having a negative χ creates a negative lens. The power of the lens will not only depend on χ but also on the absorption coefficient of the substrate. If the correct thickness of the DKDP compensation plate is chosen, then the positive thermal lens of the optical element to be compensated and the negative lens of the DKDP will cancel. As the lenses are generated by the transmitted laser then the compensation will be insensitive to alignment and will work at all laser powers.

Experimental tests have been carried out on 10mm thick z-cut samples of DKDP provided by MolTech GmbH. Figure 49 shows the thermally induced lens focal length as a function of transmitted laser power.
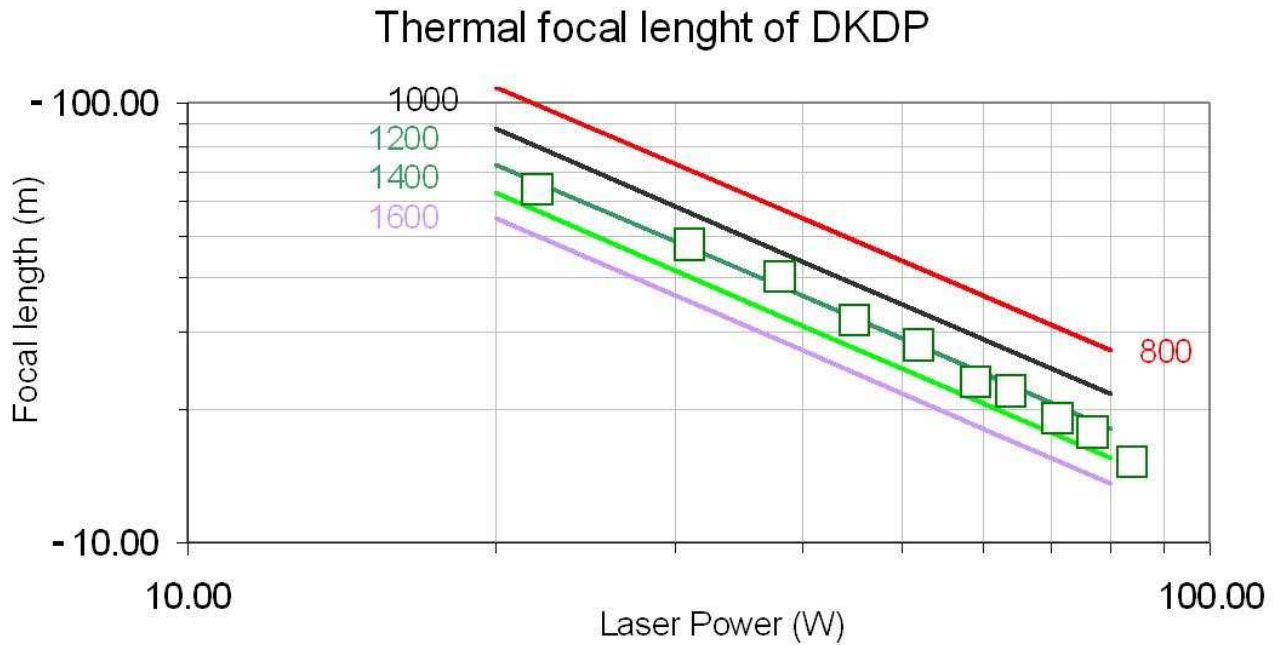
Figure 49: Experimental measurements of negative lensing in DKDP as a function of transmitted laser power. Comparison with simulation yields an estimated substrate absorption of 1200ppm

These results show good agreement with thermal simulations using an absorption coefficient of 1200 ppm. It is estimated that a DKDP thickness of 4.8mm would be required to compensate for the thermal lensing in the TGG crystal of the SIB Faraday isolator. Figure 50 shows a simulation for the DKDP compensation of the TGG crystal as a function of time after the transmitted power is switched on.
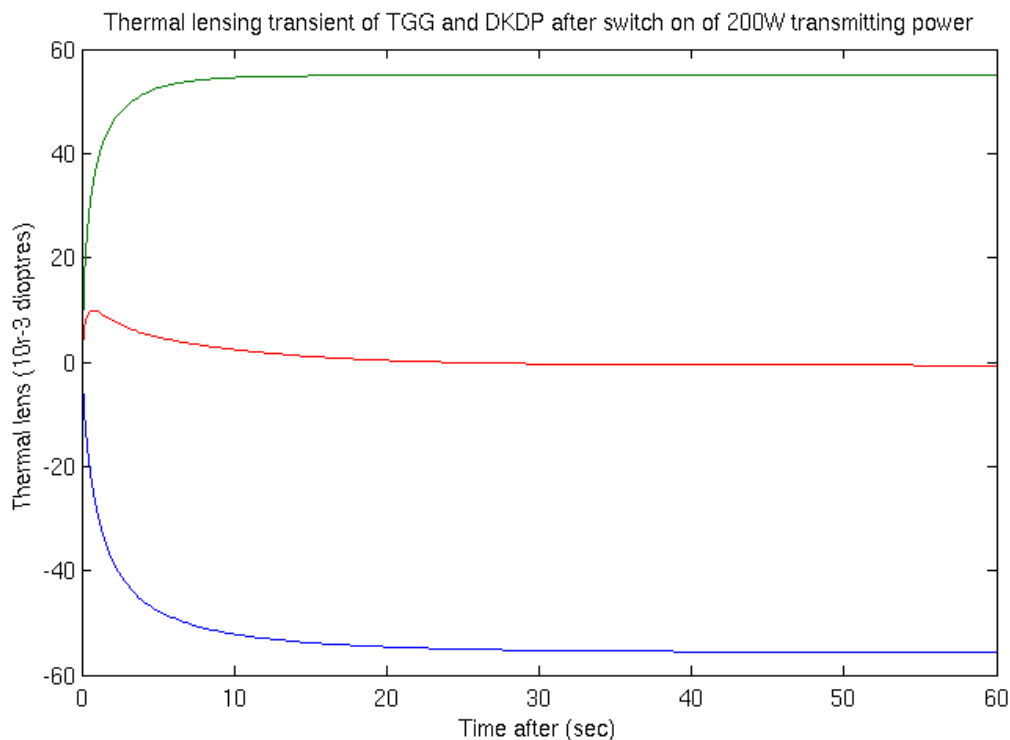
Figure 50: Simulation of thermal lensing as a function of time for TGG (green), DKDP (blue) and TGG+DKDP (red) when switching on 200W of transmitted power.

Both the TGG and DKDP have similar lensing time constants of the order of a few seconds. We see that even during these fast transients the residual lensing of the compensated system does not exceed 20% of the steady-state TGG lensing. A passive compensation system therefore seems ideal for compensating for thermal effects in the SIB Faraday isolator. This is part of the R&D work done by Novgorod Institute of Applied Physics as part of the High Power Input Optics (HPIO) R&D program [17].

Passive compensation has the advantage of being a very simple and efficient setup. However the exact combination of thickness and absorption must be chosen to have an ideal compensation. Afterwards there are no means to fine tune. In addition the system could not be used to correct for astigmatism. A passive compensation would therefore not be suitable for compensating effects in the IMC.

8.5.2.1.2. Active compensation

For the passive compensation it is the transmitted beam that is absorbed by the compensation plate creating the compensating lens. For the active compensation the compensation plate is actively heated or cooled by an external device in such a way as to create the desired compensation. An active compensation may be done on the DKDP of a passive compensation plate in order to fine tune the compensation. Otherwise any other type of suitable substrate may be used in order to create the desired lens. The advantage of this type of compensation is the possibility to compensate for astigmatism or other higher order aberrations by changing the distribution of heating on the plate. There are a number of possible solutions for heating or cooling the substrate:

- **Peltier:** The plate could be heated or cooled at its edges using a peltier or resistive heater. This system could be used principally to compensate for focus and astigmatism.
- **Scanning CO2**: A more exotic method of heating the plate would be to use a scanning CO2 laser beam. A CO2 laser would be scanned in two directions using two crossed acousto-optic modulators placed one after the other. This technique enables fast 2D scanning using a modulation frequency around the modulator's carrier. A few MHz scanning can be foreseen. By correct shaping of this modulation frequency, it is possible to generate any type of pattern that would allow the correction of higher order aberrations. By modifying the amplitude of the RF field sent to the modulator, it is also possible to easily modify the magnitude of the effect generated. In addition, this scanning would be vibration-free. This type of solution would be extremely effective and flexible but relatively expensive and complicated to develop.
- **Centrally heated double pass plate**: The laser beam would pass twice through the compensation plate by reflecting off an HR coating on the back surface. The plate would be heated at the centre using an array of heating resistors placed behind the HR coating. Depending on the number of heating resistors in the array this solution could allow the correction of higher order aberrations.

Table 4 shows the results of thermal simulations for thermal lensing due to YAG absorption itself, peripheral peltier heating and central CO2 laser heating.

Substrate	YAG absorption lens (10^{-3} dioptres)	1W Peltier lens (10^{-3} dioptres)	1W CO2 central heating lens (10^{-3} dioptres)
SF57	11.4	-15.1	677.4
DKDP	-46.9	11.8	-484.1
Fused Silica	0.0	-4.8	198.8
TGG	12.6	-2.7	106.1
BK7	11.8	-3.4	144.8

Table 4: Comparison of passive and active lensing effects in different substrates of diameter 26mm and thickness 4mm.

This result shows very clearly that creating a lens by heating the centre of the compensation plate rather than heating the edges is more efficient by more than a factor 40. In addition we see in Figure 51 that peripheral heating has a time constant which is about 10 times higher than that of central heating.
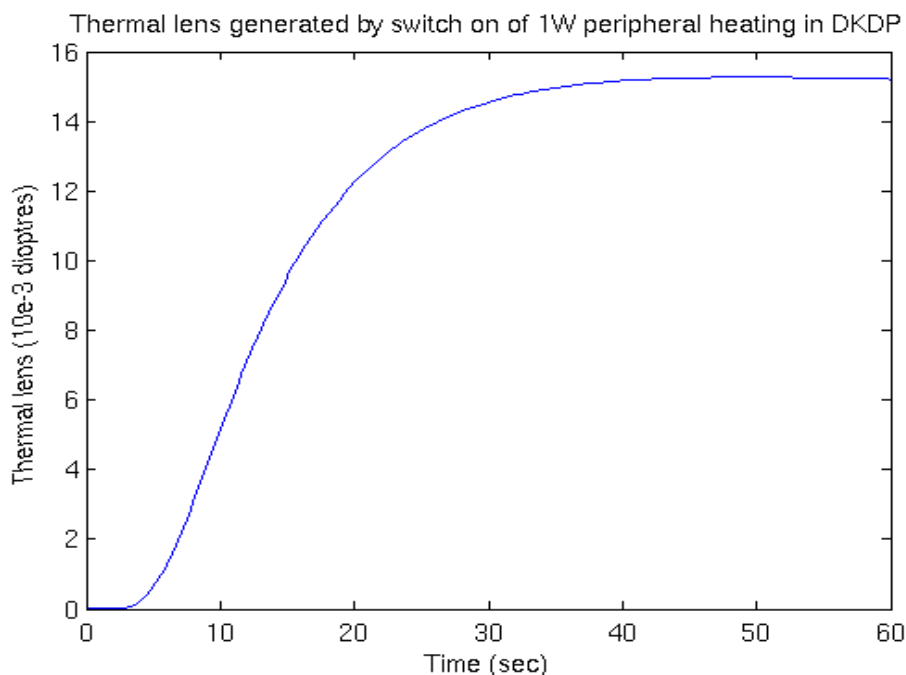
Figure 51: Simulation of thermal lensing as a function of time for 4.8mm thick, 26mm diameter DKDP when switching on 1W of peltier peripheral heating.

For the example of fine tuning the passive compensation of the Faraday isolator, 1W of Peltier heating would give a tuning range of just 20% but will increase the crystal temperature by more than 100°C. Realizing the same tuning using a central heating system (by heat resistors or CO2) would only require a few tens of mW.

In conclusion, an active compensation would be a well suited solution for the compensation of thermal effects in the IMC and fine tuning of the Faraday compensation. Peripheral Peltier heating is the simplest solution, however may only be used for relatively small and low order corrections. An adaptive central heating solution such as the scanning CO2 or heated double pass plate would be necessary to compensate larger and higher order aberrations.

8.5.2.1.3. *Deformable mirror*

Another possibility to compensate for thermal aberrations of the input beam is to use deformable mirrors. Useful mirrors for Virgo [43] could be piezoelectric or bimorph mirrors [44], widely used in high power laser control. This type of solution is extremely attractive giving the possibility of high speed (up to KHz) correction of large and high order aberrations. The cost would be around 20 Keuro. The main risk is the fact that the device would be mounted on the suspended injection bench after the IMC. It is not known if this technology could be made vacuum compatible. In addition any control noise on the mirror actuators would be directly injected into the interferometer. A great deal of research is necessary to validate the use of deformable mirrors in a gravitational wave detector. Since there is currently no R&D activity on this topic, it seems unlikely that a solution would be ready for AdV.

8.6. *Conclusions*

Taking into account the complexity and numerous thermal effects that could impact optical components of INJ, it is highly recommended to foresee a system of monitoring and a mean of compensation.

A convenient monitoring system would be the combination of two reliable devices: a phase camera system (already used and commissioned for Virgo+) and a commercial Shack Hartmann wavefront sensor. The phase camera would give access to precise information about sidebands and the Shack Hartmann would be used for its accuracy, ease of use and convenient available software that can give complete information about beam aberrations.

The compensation system would be a mix of passive components (such as the DKDP crystal that will be included inside the SIB Faraday) and active components made of centrally heated DKDP, or preferably Fused Silica substrates. The experimental investigation of these active systems still remains to be done, but simulations have given promising results.

Acknowledgement

Bibliography

[1] J.D. Mansell et al, **Appl.Opt., 40, 366-374 (2001).**

[2] G.Mueller, LSC, Internal note, **LIGO T020021-00-D (2002).**

[3] P.Fritschel, LSC, Internal note, **LIGO T010075-00-D (2001).**

[4] LSC, Input Optics Subsystem Preliminary Design Document, **LIGO-T060269-01-D (2007).**

[5] LSC, Complex modulation, **LIGO-T070197-00-R.**

[6] Ohmae et al., "Development of Electrooptic Modulator for Advanced Ground-Based Gravitational Wave Telescopes Using Stoichiometric MgO-Doped LiNbO$_3$ Crystals", **Applied Physics Express 1 (2008).**

[7] W. K. Koechner, "Thermal lensing in a Nd:YAG laser rod", **Appl. Opt. 9, 2548–2553 (1970).**

[LNFS100] LNFS 100 signal generator web page http://www.spectradynamics.com/LNFS-100.html.

[8] The Virgo Collaboration, Advanced Virgo Preliminary Design, **Virgo note VIR-089A-08, October 2008.**

[9] B. Canuel talk at the july 2008 Virgo Week.

[10] B. Canuel talk at the april 2008 Virgo Week.

[11] G. Mueller et al., "Pointing Requirements in Advanced LIGO, part 1".

[12] The VIRGO collaboration, "Results of the Virgo central interferometer commissioning", *Class. Quantum Grav., 21 S395-S402, 2004.*

[13] M. Barsuglia talk at AdV bi-weekly meeting, **July 2008.**

[14] Barriga et al., "Self-Compensation of Astigmatism in Mode-Cleaners for Advanced Interferometers", Journal of Physics: Conference Series **32** (2006) 457–463, Sixth Edoardo Amaldi Conference on Gravitational Waves

[15], P. La Penna, E. Genin and J. Marque, "Suspended Injection Bench Faraday in-vacuum isolation measurement", **Internal Virgo Note, VIR-026A-07, Sept. 2007.**

[16] Jean-Yves Vinet, "Backscattering off MC end mirror, VIR-NOT-OCA-1390-221, July 2002.

[17] Khazanov et al., "High aperture, high average power Faraday isolators", March 2009. https://workarea.ego-gw.it/ego2/virgo/advanced-virgo/inj/restricted/documents/advanced-virgo/high-power-faraday-isolator/Virgo_report_March.doc/

[18] A.Brillet, J-Y. Vinet, V. Loriette, J-M. Mackowski, L. Pinard and A. Remillieux "Virtual gravitational wave interferometers with actual mirrors", Phys. Rev. D67 102006 (2003).

[19] The VIRGO collaboration, "The Virgo physics book vol. II", **Chap. 6: Heating issues, last release April 2006.**

[20] S. Hebri, "Radiation pressure in the virgo input mode cleaner", **Internal Virgo Note, VIR-NOT-EGO-1390-331, Nov. 2006.**

[21] Francois Bondu, " L'interféromètre Virgo : propriétés optiques, stabilisation en fréquence du laser", Habilitation a diriger la recherche, June 2008.

[22] Michele Punturo, "Radiation pressure effects on Virgo mode cleaner", **VIR-NOT-PER-1390-284, 2004.**

[23] M. Mantovani, E. Genin, "Advanced Virgo INJ: Radiation pressure effects in the Advanced Virgo IMC - longitudinal and angular directions", **Virgo note VIR-009A-09, 2009.**

[24] Canuel, Day, Genin, Marque, LaPenna "AdV INJ design requirements", **VIR-XXX-XXX, 2009.**

[25] P. Fritschel, "Notes non laser frequency stabilization", **VIR-NOT-LAL-1380-051, 1993.**

[26] L. Chen et al., "Vibration-induced elastic deformation of Fabry-Perot cavities", **Physical Review A, 74, 053801 (2006).**

[27] Calloni E., Barone F., Di Fiore L., Grado L., La Penna P., Milano L., "Effects of misalignments and beam jitters in Fabry-Perot laser stabilization", **Opt. Comm., 142, 50-54 (1997).**

[28] The Virgo collaboration, "In-vacuum optical isolation changes in a Faraday isolator", **Applied Optics, Vol. 47, Issue 31, pp. 5853-5861, October 2008.**

 [29]P. LaPenna et al. "Suspended Injection Bench Faraday isolation remote adjustment", **Virgo change request, virchrq0012007 (2007).**

[30]E. Khazanov et al, "Investigation of self-induced depolarization of laser radiation in terbium gallium garnet", **IEEE Journ. Quant. Electr., 35 (8), (1999)**

[31]E. Khazanov et al, "Compensation of thermally induced modal distortions in Faraday isolators", **IEEE Journ. Quant. Electr., 40 (10), (2004**).

[32] E. Genin, "Virgo+ Laser and Injection system : Status", **Talk to Virgo Coll. Meeting Nov. 2008.**

[33**]** B. Canuel, E. Genin, **"**R&D project : High power input optical components for Advanced Virgo April 2008 status report", **Virgo note VIR-082A-08, October 2008.**

[34] B.Canuel, Jan 2009, seminar at LIGO Livingston.
https://workarea.ego-gw.it/ego2/virgo/advanced-virgo/inj/restricted/hpio-r-d/randd-presentation/canuel_13_01_09.ppt/

[35] E. Genin, oct 2008, weekly commissioning meeting:
http://wwwcascina.virgo.infn.it/commissioning/weekly/2008/Oct2008/Genin_weekly_14102008.ppt

[36] J. Marque, march 2009, mirror absorption meeting:
http://wwwcascina.virgo.infn.it/collmeetings/presentations/2009/2009-02/Detector/Marque_100309_Virgo&LigoAbsorptionMeasurements.ppt

[37] B.Swinkels "thermal simulation of the dihedron", Virgo logentry #21003.

[38] E. genin, J. marque, P. ruggi, Virgo logentry #20760.

[39] Product description of Intellium PDI from ESDI
http://www.engsynthesis.com/p/products/wavefront_sensing/point_diffraction_interferometer.php

[40] S. Bigotta, feb 2009, Virgo Week:
http://wwwcascina.virgo.infn.it/collmeetings/presentations/2009/2009-02/Commissioning/Bigotta_090202.pdf

[41] Product description of SwissRanger from Mesa Imaging
http://www.mesa-imaging.ch/prodview4k.php

[42] A. Brooks, "Hartmann Wavefront Sensors for Advanced Gravitational Wave Interferometers" Doctoral thesis (2007), University of Adelaide https://gwic.ligo.org/thesisprize/2007/Brooks_Thesis.pdf

[43] S Avino, E Calloni, A Tierno, B Agrawal, R De Rosa, L Di Fiore, L Milano and S R Restaino, "Low-noise adaptive optics for gravitational wave interferometers" **Class. Quantum Grav. 23 (2006) 5919–5925**
[44] Adaptive optics general informations,
http://www.imperial.ac.uk/research/photonics/research/topics/aotoolkit/adaptive_optics_for_all.htm
[45] M.Pichot, F.Bondu, M.Laval, A.Brillet, C.N.Man¸ "Clipping loss of Input Mode Cleaner: results of Dark F simulations - Update for Virgo+", Virgo internal note, VIR-020A-09

On the web

AdV INJ web site:
https://workarea.ego-gw.it/ego2/virgo/advanced-virgo/inj/

AdL Input Optics web site:
http://ilog.ligo-wa.caltech.edu:7285/advligo/Input_Optics_Optics